University of Alberta

DERIVATION AND INVESTIGATION OF MATHEMATICAL MODELS FOR SPOTTING IN WILDLAND FIRE

by

Jonathan Martin

A thesis submitted to the Faculty of Graduate Studies and Research
in partial fulfillment of the requirements for the degree of

Doctor of Philosophy

in

Applied Mathematics

Department of Mathematical and Statistical Sciences

Fall 2013
Edmonton, Alberta

Dedication. This thesis is dedicated to Diana, my Mother and Father, who have kept me driven to see this project through to completion.

Abstract

Spotting in the context of wildland fire refers to the creation of new fires, downwind from an existing fire front, where the new fires result due to the launch, and subsequent fuel bed ignition upon landing, of burning plant material released from the main front. We will present a new integro-partial differential equation (i-PDE) model which includes both local spread, combustion/extinguishment, and non-local spread due to spotting. We will also present a new model for firebrand transport in the atmosphere, which allows us to incorporate existing physical or empirically-based submodels existing in the literature to obtain the spotting distribution. We will use the spottting distribution to investigate the problem of fire fronts breaching obstacles to local fire spread, such as a highway or river, and the spotfire distribution appears as a kernel for the integral term in our i-PDE model. We then investigate travelling wave solutions to the i-PDE model, demonstrating that spotting can increase the rate of spread, or cause acceleration of a fire front's advance.

Acknowledgements

I would like to thank Cordy Tymstra, Canadian Forest Service, and the fire research division of Alberta's Sustainable Resource Development. It was during a MITACS internship with Cordy that I first learned about spotting, and I am grateful to MITACS for supporting me with two summer internships. Thanks to Prof. Anne Bourlioux, Universite de Montreal, for pointing out some errors in my earliest modelling attempts.

Thanks to the Centre for Mathematical Biology (CMB) at the University of Alberta, its members and guests over the years have broadened my perspective about modelling nature. In connection I would like to express my indebtedness to the PIMS IGTC in Mathematical Biology, who provided a two year fellowship supporting my studies. I would like to thank in particular Prof. Gerda de Vries at the CMB, for helping me become a better communicator as part of our weekly journal club, and especially for supporting my teaching efforts.

Finally, and most importantly, I would like to thank my advisor Prof. Thomas Hillen. Thomas has been a source of knowledge and inspiration, and has also been very supportive in dealing with the roadblocks I've run into while writing this thesis. His approach helped me early on to find my own research problems, so as to work independently, but Thomas has always been available whenever I have had questions. This thesis is largely indebted to Prof. Hillen's valuable suggestions.

Table of Contents

1 Introduction **1**

1.1 The central problem of this thesis: the role of spotting in wildland fire . . . 1

1.1.1 The scope and importance of modelling in wildland fire 1

1.1.2 The influence of spotting in wildland fire spread 2

1.1.3 Spotting and wildfire rate of spread, acceleration, and the probability of breaching . . . 4

1.2 Prior efforts in modelling the local spread of wildfires 5

1.2.1 Scale in wildfire modelling: micro and macroscales . . . 5

1.2.2 An empirical model for local spread: the Fire Behaviour Prediction System . . . 6

1.2.3 Macroscopic models: cellular automata and front-propagation models . . . 7

1.2.4 Model types: probabilistic versus deterministic 11

1.3 Travelling wave models from invasion ecology . . . 12

1.4 Thesis flowchart . . . 13

2 Derivation of a probabilistic model for the spread of wildfires including non-local spread by spotting **16**

2.1 Chapter Introduction . . . 16

2.2 Derivation of a discrete probabilistic model for linefire spread with spotting . . . 18

2.3 Determining the discrete spotting probability . . . 23

2.3.1 Separating the launching and transport processes . . . 23

2.3.2 The launching probability π . . . 23

2.3.3 Transport and ignition probability $\mathcal{T}$ . . . 24

2.4 Integrating local spread, continuous limit 27
2.5 Continuous limits of this chapter's discrete models: integro-partial differential equations (iPDE)'s for wildfire fronts 30
2.6 Limiting equations, and generalizations of our derived (iPDE)'s 33
2.6.1 A quasi-steady state assumption for the total fuel loading 33
2.6.2 Further simplification: removing the time-delay 35
2.6.3 The diffusion operator L 36
2.6.4 The spotting operator $\mathcal{S}$ 36
2.6.5 The spotting-dominated case 37
2.7 Chapter summary 38

3 Transport model for firebrands and the asymptotic landing distribution 40
3.1 Chapter Introduction 40
3.2 Transport model for impulse release in the plane 42
3.2.1 The vertical launch distribution, spotting distribution . 42
3.2.2 Transport model, initial and boundary conditions . . . 44
3.3 Impulse-release, transport-type model for combusting firebrands 46
3.3.1 The characteristic equations and their solution operators 46
3.3.2 Global existence and uniqueness of solutions in L^1 and L^∞ 49
3.4 The landed branches L and the asymptotic landing distribution $\mathbb{L}$ 52
3.4.1 The one-dimensional case 53
3.5 Chapter summary 55

4 Models for firebrand generation, combustion, transport and fuel bed ignition, new and old 56
4.1 Chapter Introduction 56
4.2 Firebrand distribution generated from burning vegetation . . . 57
4.2.1 Experimental results and challenges 57
4.2.2 Model G1: Regression analysis on Manzello's data . . . 58
4.2.3 Model G2: Models obtained from burning slash 60
4.3 Firebrand combustion 60
4.3.1 The combustion operator C and its inverse 60
4.3.2 Model C0: Constant burning rate 61

4.3.3 Model C1: Tarifa's original experiments and models . . 62
4.3.4 Models C2, C3: Caricatures of Tarifa's model 62
4.3.5 Model C4: Tse and Fernandez-Pello's improvements . 63
4.3.6 Model C5: Including more physical realism 64
4.3.7 Model C6: Albini's combustion model within line thermals 65
4.3.8 A model for firebrand temperature 65
4.4 Terminal velocity 67
4.4.1 Drag, gravity and terminal velocity 67
4.4.2 Model V1: Constant terminal velocity 68
4.4.3 Model V2: Experimentally determined model 68
4.5 Firebrand lifting in the fire's convection column 69
4.5.1 Definition and characteristics of wildfire plumes 69
4.5.2 The types of spotting considered in this thesis 70
4.5.3 The Baum and McCaffery plume 71
4.5.4 Mathematical models for the launching distribition $\phi(z, m)$ 74
4.6 Transport in the atmosphere 77
4.6.1 The atmospheric boundary layer 77
4.6.2 Model W1: Constant horizontal wind 78
4.6.3 Model W2: Logarithmic horizontal wind 78
4.6.4 Model W3: Power-law wind profile 79
4.7 Ignition of fuel beds by firebrands 81
4.7.1 Challenges in modelling fuel bed ignition 81
4.7.2 Experimental investigations of firebrand ignition 82
4.7.3 Ignition probabilities: Models I1, I2, I3 83
4.8 Summary of the models considered in this Chapter 86

5 Analytic examples of the spotting distribution 88
5.1 Chapter Introduction 88
5.2 Analytically-determined landing distributions and travel times 89
5.2.1 Constant wind, constant terminal velocity 89
5.2.2 Power law profile for w, constant vertical velocity . . . 92
5.2.3 Logarithmic profile for w, constant vertical velocity . . 95
5.2.4 Model (W1, V1, C0, L3): a simple illustration of $\mathbb{L}(x, m)$ 97
5.3 The spotting distribution $\mathbb{S}(x)$ determined from $\mathbb{L}(x, m)$ . . . 100

5.4 Some example spotting kernels 102
5.4.1 Case **(I1)**: Spotting kernel for (W1,V1,C4,L1) 102
5.4.2 Case **(I2)**: Spotting kernel for model (W1,V1,C4,L1) . 104
5.4.3 Case **(I3)**: The kernel for model (W1,V1,C4,L1); The kernel for (W1,V1,C0,L3) from 5.1.4. 106
5.4.4 A family of 'fat-tailed' kernels 110
5.5 Extending the delayed-(iPDE) model derived in Chapter 2 . . 112
5.6 The spotting distribution and spotfire breaching 113
5.7 Chapter summary 114

6 Analytic investigation of solutions to the i-PDE models: rates of spread and acceleration 116
6.1 Chapter Introduction 116
6.2 Existence and uniqueness of solutions in $L^2(\Omega)$, for bounded $\Omega \subset \mathbb{R}$ 117
6.3 Existence and uniqueness of solutions in $L^2(\mathbb{R})$ 119
6.4 The spotting-dominated case: Some background and notation 119
6.5 Spotting dominated case: existence of travelling wave solutions 122
6.5.1 Some recent results on travelling waves 122
6.5.2 Travelling wave solutions for our model (6.9) 123
6.6 Spotting dominated case: spreading speeds and acceleration . 126
6.6.1 Spreading speeds in the linearized case 126
6.6.2 Recent results on spreading speeds and accelerating solutions 128
6.6.3 Computing spreading speeds, or acceleration for our model (6.9) 130
6.7 Chapter summary 136

7 Numerical investigation of traveling waves and pulses for the iPDE models from Chapter 2. 137
7.1 Chapter Introduction 137
7.2 Numerical solutions of the equations in this Chapter 139
7.3 Traveling waves for the single equation model in the spotting-dominated case, with no time-delay 140
7.3.1 An uniform spotting kernel, travelling waves 140

7.3.2 A fat-failed kernel, accelerating solution 141
7.4 The temporal dynamics of combustion and heat loss 143
7.4.1 Case T1: Mass-action kinetics 143
7.4.2 Case T2: Second-order kinetics in u 144
7.4.3 Case T3: Arrhenius kinetics 145
7.4.4 Model T4: Logistic-type kinetics 147
7.4.5 Model T5: Ignition thresholds 147
7.5 Adding diffusion to the temporal dynamics 148
7.5.1 Traveling pulses for the mass-action model T1 149
7.5.2 Traveling pulses for the non-linear case T2 149
7.5.3 Travelling pulses for the Arrhenius model T3 151
7.5.4 Traveling pulses for the logistic model T4 153
7.6 The spotting-dominated case: traveling pulses 153
7.6.1 T4 kinetics, uniform probability distribution kernel . . 155
7.6.2 T4 kinetics, exponential spotting kernel 156
7.6.3 T4 kinetics, fat-tailed kernel, : acceleration 157
7.6.4 T1 kinetics, uniform kernel 158
7.6.5 T1 kinetics, exponential kernel 159
7.6.6 T1 kinetics, fat-tailed kernel: acceleration 160
7.6.7 T3 kinetics, uniform kernel 162
7.6.8 T3 kinetics, exponential kernel 163
7.6.9 T3 kinetics, fat-tailed kernel: acceleration 164
7.7 Chapter summary 165

8 Discussion 166

Appendix A Smooth solutions for first-order BVP's and the method of characteristics 172

A.1 The characteristic equations 172
A.2 Constructing smooth solutions using characteristics 174

Appendix B Essentials of semigroup theory 178

B.1 The Lebesgue spaces L^p 178
B.2 The Sobolev spaces $W^{k,p}$ 179
B.3 The dual space of important function spaces 181

B.4 Banach-space valued functions 181
B.5 Semigroups of bounded linear operators 182
B.6 Boundedness of integral operators 184
B.7 The Bounded Perturbation Theorem 185
B.8 The initial value problem for reaction-diffusion equations in an open bounded domain 186
B.9 Weak solutions to reaction-diffusion equations 187
B.10 The Fourier transform and the heat equation on $\mathbb{R}^n$ 189
B.11 The heat semigroup on $\mathbb{R}^n$ 191

Bibliography **192**

List of Tables

4.1 Physical and empirical models for spotting subprocesses 87

List of Figures

1.1 Caricature of the spotting process. A distribution of firebrands are launched to various heights y above a spreading ambient forest fire. 3

1.2 Elliptical growth, starting from a point ignition at the center of the ellipse, for homogeneous spread conditions 9

1.3 Huygens' principle for elliptical fire spread, starting from an ellipse 9

1.4 The organization of the thesis is indicated in this flowchart. . . 15

2.1 Shown is the basic fire scenario in the plane considered in this Chapter. 19

2.2 Here we discretize the plane uniformly, so that points are separated a finite distance Δx from each other, and we advance forward in timesteps of magnitude Δt. 21

2.3 Shown is our discretization of heights z, where $\Delta z = \nu \Delta t$. . . 26

3.1 At a given instant of time, the plane is divided by the fire front into disjoint subsets, according to whether a point has been burned or not. These subsets consists of the burned region Ω, shown in a darker shade of red as an ellipsoid in this figure, and the unburned region $U := (\Omega \bigcup \delta\Omega)^c$, the latter shown in green in this figure. 43

3.2 Determining the "flight and burning" distribution $\mathbb{L}$ from the vertical launch distribution ϕ. 54

4.1 The mass distribution for the 5.2m Douglas fir firebrands, reproduced from (47) in the histogram. 59

4.2 Sketch of a cross-section along the burning front. Presented are the three regions of the Baum and McCaffery plume. 72
4.3 Velocity versus height for three of the logarithmic profiles, described in Equation (4.44.) 79
4.4 A comparison of the wind profiles discussed in this Section. . . 80
4.5 A comparison of the ignition models discussed in this section. 86

5.1 Spatial characteristics with velocity field for the power-law wind profile, with constant vertical velocity, described in (5.12) . . . 93
5.2 We present an illustration of 500 realizations of the random variables for height z and mass m, uniformly distributed as in Equations (5.28) and (5.29). 98
5.3 Here we illustrate the asymptotic landing distribution as a surface above the (x, m)-plane, corresponding to the initial distribution illustrated in Figure 5.2. 99
5.4 Here we illustrate the asymptotic landing distribution as a surface above the (x, m)-plane, corresponding to a similar initial distribution illustrated in Figure 5.2, but this time with $H = 10$, $N = 1000$, $\overline{m} = 4$, $v = 1$, $|f|= 0.1$, and $\overline{z} = 100$. 100
5.5 Here we illustrate the asymptotic landing distribution as a surface above the (x, m)-plane, corresponding to a similar initial distribution illustrated in Figure 5.2, but this time with $H = 10$, $N = 1000$, $\overline{m} = 4$, $w = 4$, $|f|= 0.1$, $\overline{z} = 100$. 100
5.6 Here we show the spotting distribution $\mathbb{S}(x)$ corresponding to Equation (5.38) and the case (I1) of unique launching heights, for mass threshold values $\underline{\mathrm{m}}= 0.001$ kg, $\underline{\mathrm{m}}= 0.002$ kg, and $\underline{\mathrm{m}}= 0.004$ kg. 104
5.7 A plot of the ignition probability $E(m)$ described in (5.39), for the choices $A = 1,\ 2,\ 4$, which correspond to the transition of E to 1 at $m = 1, 2, 4$ grams respectively. 105
5.8 A plot of the spotting distribution (5.40) versus x (measured in metres), for the same choices of parameter described in the caption to Figure 5.6, but allowing A to vary between $A = 1, 2, 4.$ 106

5.9 A plot of the ignition probability densities given in (5.41), changing the threshold mass $\underline{m}$at which ignition is certain, from $\underline{m}$= 4, 2, and 1 grams respectively. 107
5.10 A plot of the spotting distribution (5.43), changing the threshold mass m at which ignition is certain, from $m = 4, 2$, and 1 grams respectively (see Figure 5.9 for an illustration of the corresponding ignition operators $E(m)$). 108
5.11 A comparison of the exponentially bounded kernel $2e^{-2x}$ versus the exponentially unbounded kernel $e^{-x^{1/2}}$. 111

7.1 We illustrate how a compactly supported initial condition for (7.4), with uniform spotting kernel given in (7.23) for $L = 5$, evolves into a right-traveling solution. We plot $u(t)$ versus x where x is measured in metres, for various snapshots in time, measured in seconds; the arrows point out the leading edge. . 141
7.2 We plot accelerating solutions $u(t)$ to (7.4) versus x, for the exponentially unbounded kernel $\mathbb{S}(y)$ from (7.5), showing the solution at various snapshots in time, and the spatial extent reached. 142
7.3 We plot a partial phase portrait for mass-action kinetics model (7.8), with a few arrows to indicate the direction of trajectories. 144
7.4 We plot a partial phase portrait for u-nonlinear kinetics model (7.9), with a few arrows to indicate the direction of trajectories. The parameters are $\alpha = 0.7$, and $d = 0.5$. 145
7.5 We plot a partial phase portrait for the Arrhenius kinetics model (7.10). 146
7.6 We plot a partial phase portrait for the logistic kinetics model (7.11). 148
7.7 Illustration of traveling pulses for the solution to the system (7.13), with dynamics determined by model T1. 150
7.8 Illustration of traveling pulses for the solution to the system (7.14), with dynamics determined by model T2. 151

7.9 Illustration of traveling pulses for the solution to the system (7.15), with dynamics determined by the Arrhenius model T3, in the case where $k = 0.5$. 152

7.10 Illustration of traveling pulses for the solution to the system (7.16), with dynamics determined by the logistic model T4. . . 154

7.11 Illustration of traveling pulses for the solution to the system (7.19), with dynamics determined by the logistic model (7.20), with uniform spotting kernel given in (7.23), and with $L = 5$. . 156

7.12 Illustration of traveling pulses for the solution to the system (7.19), with dynamics determined by the logistic model (7.20), with exponential spotting kernel given in (7.24), and with $\lambda = 0.5$. 157

7.13 Illustration of traveling pulses for the solution to the system (7.19), with dynamics determined by the logistic model (7.20), with exponential spotting kernel given in (7.24), and with $\lambda = 0.5$. 158

7.14 Illustration of traveling pulses for the solution to the system (7.19), with dynamics determined by the mass-action model (7.21), with uniform spotting kernel given in (7.23). 159

7.15 Illustration of traveling pulses for the solution to the system (7.19), with dynamics determined by the mass-action model (7.21), with exponential spotting kernel given in (7.24). 160

7.16 Illustration of traveling pulses for the solution to the system (7.19), with dynamics determined by the Arrhenius model (7.21), with exponentially unbounded spotting kernel given in (7.25), with parameter $\lambda = 0.5$. 161

7.17 Illustration of traveling pulses for the solution to the system (7.19), with dynamics determined by the Arrhenius model (7.22), with uniform spotting kernel given in (7.23). 162

7.18 Illustration of traveling pulses for the solution to the system (7.19), with dynamics determined by the Arrhenius model (7.22), with exponential spotting kernel given in (7.24). 163

7.19 Illustration of traveling pulses for the solution to the system (7.19), with dynamics determined by the Arrhenius model (7.22), with exponentially unbounded spotting kernel given in (7.25). 164

1.1 Illustration of Proposition A.1, in the planar case. 176

Chapter 1

Introduction

1.1 The central problem of this thesis: the role of spotting in wildland fire

1.1.1 The scope and importance of modelling in wildland fire

Forest fire spread in the boreal forest is a complex process, and is of major concern both to industry and to the public from a fire management perspective [67]. Over a billion dollars is spent each year between the United States and Canada on fire management operations [89]. Further, in the wildland-urban interface, forest fires pose a risk to assets and sometimes human lives [93]. An accurate predictive model describing the growth of large-scale forest fires is therefore important in a variety of contexts. Such models have been developed, though there is still much room for improvement.

Wildfires occur in many ecosystems on Earth. The types of fire, their intensity, and yearly time of occurrence can vary considerably depending on geographic location [67]. Indeed, in very wet climates, wildland fire may not be an issue. On the other hand, the Boreal forest, for example, which covers much of Northern America, regularly experiences forest fires, and as such fire as a disturbance process is vital in the preservation of the structure of the Boreal forest [67].

Forest fires are constantly in the news these days. Not only are wildfires an important ecological phenomenon, where wildfires meet the urban-wildland interface, they pose possible danger to human assets, and even in extreme cases to human life [67]. In particular around human housing, and industrial lands used to harvest trees, understanding the behaviour of wildfires is paramount, from both ecological and fire management perspectives.

1.1.2 The influence of spotting in wildland fire spread

Wildfires are capable of creating powerful updrafts, called convection columns, which launch burning plant materials, referred to as firebrands, into the atmosphere [2]. These firebrands are then transported by the ambient windflow, simultaneously combusting and decreasing in mass, until they reach the ground. Upon landing, depending on the local fuel and weather conditions at the landing site, a firebrand may ignite the local fuel and start a new fire. Such a fire is called a *spot fire*, and the process by which new fires are created by wind-driven firebrand ignition is called *spotting* (see Figure 1.1 for a sketch of the spotting process). Historically the first scientific description of the spotting process is credited to George Byram [20].

Spotting is not important in all fire contexts, but appears more frequently in extreme fire situations. In Boreal forests of North America, there are vast continuous stretches of coniferous forests, capable of creating incredibly intense fires, called *crown fires* ([26],[5]). These crown fires are capable of prolific spotting. Further, as reported in [5], current cannot account for the variability in the *rate of spread* of such fires. The rate of spread is typically measured in kilometres per hour, and is a measure of how fast the front is propagating.

In the chapparal brush of California, spotting from brushfires annually threatens property in the wildland-urban interface [93]. In Australia, spotting is a major issue for fires in Eucalyptus-grassland forests ([31], [56]). In the case of certain Eucalyptus fires, severe burning conditions have led to the observation that the fire's boundary "appears to be moving as a continual coalescence of spot fires" [31]. We will be interested in examining this *spotting-dominated case* in detail later in this thesis.

Spotting is often mentioned as being one of the most difficult problems for forest fire fighters, and has been incorporated in an ad-hoc way into existing

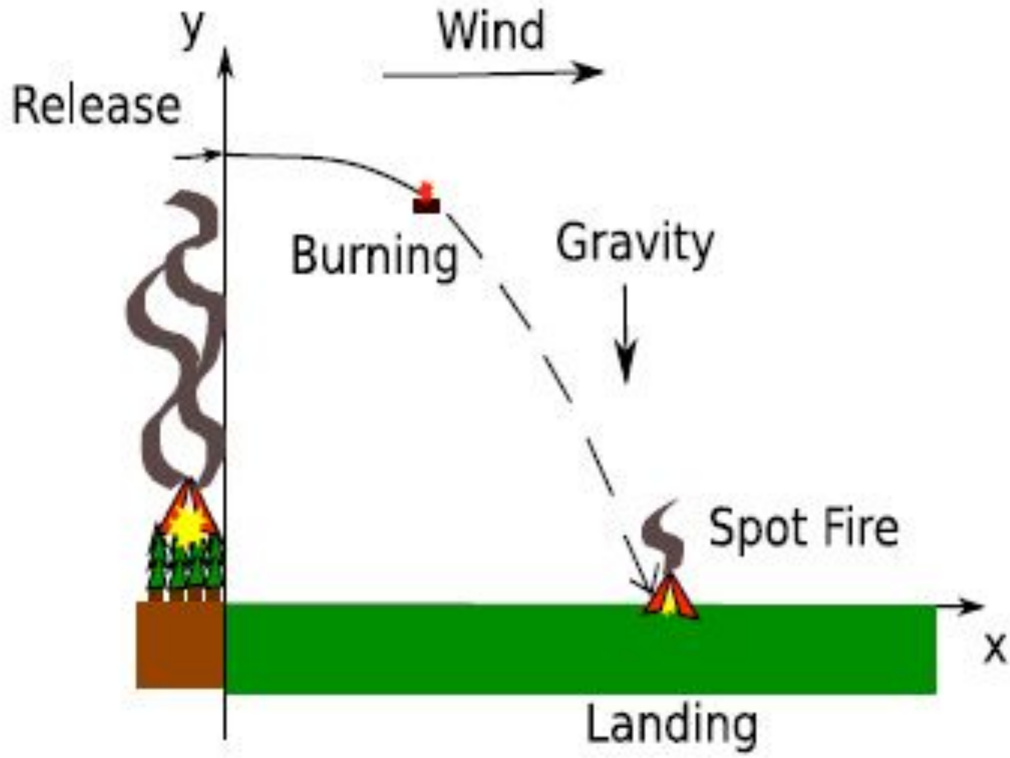

Figure 1.1: Caricature of the spotting process. A distribution of firebrands are launched to various heights y above a spreading ambient forest fire. The firebrands are then transported in the ambient windfield, combusting and falling downward due to gravity, until they finally come to rest downwind of the main fire. Depending on the local conditions for fuel and weather at the landing site, a spot fire may be ignited by the combusting firebrand.

fire simulators to help deal with this issue [4]. Indeed, spotting is often the cause of a fire breaching across an extended obstacle to local spread, such as roads, rivers, or man-made fuel breaks [3].

The stochastic nature of the spotting process, whose key features are outlined in the caricature Figure 1.1, makes it very difficult for forest fire fighters to predict where a spot fire is likely to occur. Indeed, the *spotting distribution* is an under-addressed issue, with most prior modelling focusing on the maximum spotting distance (e.g. [2]). A consequence is that spotting is often the cause of escape of prescribed fires [26]. Analagously, spotting may allow a fire to spread faster across a region along which the local spread is relatively slow [5]. The influence of spotting on the rate of spread is a major topic of this thesis.

When conditions aloft are favorable for strong convection column development, or large-scale fire-induced vortices (fire whirls) exist, spotting may contribute significantly to a fire's spread. A spot fire 29 km downwind of an existing fire in Victoria, Australia appears to be the longest recorded spot fire event [56]. As reported by Ellis [31], the Ash Wednesday fires in Australia, which occurred on the 16th of February 1983, produced spotting distances of between 5 and 12 kilometres, with the most extreme incident measured being 25 kilometres from the primary fire.

In addition, there are examples in the literature which indicate that spotting can at times lead to the *acceleration* of a fire's rate of advance. During the Beerburrum Fire No. 48, which occurred in Queensland Australia in 1994, the firefighters observed "Spotting..accelerated its rate of spread and its advance was halted only by Pumecestone Passage" [31].

1.1.3 Spotting and wildfire rate of spread, acceleration, and the probability of breaching

The central problems which we would like to address in this thesis are:

- What is the *spotting distribution*, or the probability of spot fire ignition, downwind of an existing fire front?
- What is the probability that a fire will breach an obstacle to local spread?
- What role does spotting play on the *rate of spread* of a fire front?
- Can spotting *accelerate* a fire's advance?

We will develop an integro-PDE model for the instantaneous fire probability, which incorporates combustion, local spread, and spotting. The kernel of the integral term contains the spotting distribution, and we will see that it can have a big influence on the fire's rate of spread. From first principles, we will derive the spotting distribution in Chapters 3 through 5, since it has been at present investigated only in the recent paper by Wang [90], in a very limited context. Further, there are no other existing models which incorporate local spread, and spotting via a spotting distribution. Understanding this distribution is also a first step towards addressing the problem of spot fire breaching. The remaining questions will be addressed later, in Chapters 6 and 7.

The type of spotting scenario is determined by the fire's convection column, and the prevailing winds aloft [25]. The most extreme spotting occurs either from a towering convection column, or if there are very strong winds which cause shearing of a strong convection column higher in the atmosphere [25].

1.2 Prior efforts in modelling the local spread of wildfires

Forest fire is a multi-scale phenomenon, and a variety of modeling paradigms and methods have been involved in its description. Broadly speaking, models can be described as empirical, semi-empirical, or physics-based. Empirical models are based solely on statistical relationships obtained through experiment, while physics-based models rely on the numerical solution of combustion and transport equations. Naturally, semi-empirical models are some hybrid of the other two types. A complete review of almost all such modeling prior to 2007 can be found in the series of papers by Sullivan [82].

1.2.1 Scale in wildfire modelling: micro and macroscales

The authors in [79] propose a classification of the various spatial scales on which forest fires operate. At each spatial scale, different modelling approaches are appropriate.

At the microscopic scale, herbaceous material is a porous medium, consisting of solid, liquid, and gaseous phases. Here, pyrolysis and vaporization are the dominant physical processes, and the use of transport equations for the constituents is the appropriate modelling framework. A good introduction to transport processes is presented in [29].

At a coarser spatial scale one may speak of a combustion model, which consists of the transport equations of an equivalent homogenized medium. Recall that the fire environment is highly heterogeneous in space and time. A mathematical introduction to homogenization is presented in the monograph [21].

Such combustion models can be scaled up to the macroscopic scale, for which the typical flame length is very small compared to length scale of the ambient windfield. Models appropriate at this scale include cellular automata models (e.g., [18]), wavefront-propagation models (e.g., [69]), and reaction-diffusion models (e.g., [91], [11]). At this scale, the ambient weather and wind, fuel type distribution, and topography are the primary forces which drive a wildfire's invasion.

1.2.2 An empirical model for local spread: the Fire Behaviour Prediction System

The Canadian Forest Service's Fire Behaviour Prediction System (FBP) is an empirically-based system for predicting fire behaviour [40]. The original models accounted for 16 different fuel types found in Canada, classified according to species-type, and whether the fuel type is coniferous, deciduous, mixedwood, slash, or grassland. The system constructs models using regression analysis on a data set consisting of over 500 monitored fires.

The FBP model accounts for fuel type and distribution, weather, topography, and fuel moisture content. Primary outputs are the head, flank and back rates of spread (discussed in the next subsection), fuel consumption, fire intensity, and whether crowning occurs and the crown fraction burned. The model accounts for diurnal variations in moisture content and wind/weather. The most important output determining the ignition probability is the so-called Fine Fuel Moisture Code (FFMC), which provides a measure of the moisture content in the most combustible surface fuels. The greater the FFMC, the lower the fine fuel moisture content.

Computation of the rate of spread depends naturally on the fuel type considered. The most extreme rates of spread are observed in dense coniferous plantations, as occur naturally or in industrial horticultural stands. Further, crown fires, where the spread occurs through the tree canopy, have much higher intensities and rates of spread relative to the other fuel types (with the notable exception of grass fuel types). The FBP model provides a probability for crowning to occur, as well as the time lapse between ignition of the surface fuels and crowning.

1.2.3 Macroscopic models: cellular automata and front-propagation models

Cellular automata models

The first computer simulator used to compute the spatial spread of a fire was a cellular automata model developed in 1971 by Kourtz and O'Regan [89]. These models are stochastic in nature. In such a model, the plane is divided up into cells, each of which may be burning or not. The fuel inside each cell is assumed to be of a particular type, and one defines a neighbourhood of adjacent cells. These neighbourhoods could consist, for example, of the nearest North, East, West and South neighbours. If a cell is burning, and a non-burning cell is in the burning cell's neighbourhood, then from one finite time step to the next fire will spread to the non-burning cell with some probability.

Modelling the probability of spread between adjacent cells is a complicated problem, and has been dealt with in a series of papers [89]. Many of them use the idea that the waiting time for spread to occur should be inversely related to the rate of spread R, which for example could be provided by the Fire Behaviour Prediction system [40].

A recent cellular automata model [18] was the first to incorporate spotting. The authors assumed a simple two-dimensional normal distribution for the spotting distribution, where the spotting distribution represents the probability of ignition occurring in a non-burning cell in a given time step. This model was considered separate from local spread, in which non-burning cells can be ignited by their burning neighbours with some probability. Burning cells become burnt-out in each time step with some probability. The simplicity of the spotting distribution employed in this paper provided some of the initial motivation for examining more realistic spotting kernels, as in this thesis.

In unpublished work, the author explored an extension of the model in [18] to allow for spotting distributions which are normally distributed perpendicular to the wind direction, but can take on a variety of functional forms in the wind direction. We noticed the development of fronts propagating in the wind direction, which are principally-driven by the spotting mechanism, as opposed to the local spread mechanism. We also noticed different rates of spread depending on the spotting distribution.

The dynamics of the discrete-space, discrete-time fire probability evolution model considered in Chapter 2, could be studied in such a cellular automata framework. In particular, since cellular automata models are computationally based, it would be relatively easier to incorporate the time-delays appearing in the discrete models outlined in Chapter 2.

The models discussed thus far deal with the expansion of individual forest fires. Cellular automata models, over large spatial and time scales, and where there is a possibility for regrowth of burnt-out cells, have been considered in the context of percolation theory [89]. One criticism of such models is that they do a poor job of modelling individual fires, which may have an impact on the long-time, multiple-fire landscape dynamics [89]. Again we see the need for in improvement in the modelling of fire behaviour.

Richards' model for curve expansion

A common observation amongst fire researchers, is that under homogeneous conditions for fire spread, a point-source fire ignition grows in a 'cigar-like' shape, with semi-major axis parallel to the wind direction. This shape is often approximated by an ellipse, though other shapes, such as teardrops have been observed [69]. The Fire Behaviour Prediction system [40] provides a description of these ellipses for various spread conditions, in terms of the parameters a, b, c as shown in Figure 1.2.

Let $\Gamma(t)$ denote our fire perimeter at time t, which we assume to be a smooth, simple, closed curve in the plane. We parameterize $\Gamma(t) = (x(t,s), y(t,s))$, $0 \leq s \leq 2\pi$.

Huygens' principle, first phrased in this context by Anderson [8], states that the fire perimeter $\Gamma(t + dt)$ is the envelope of all such ellipses, generated at each point locally along the fire perimeter at time t (refer to Figure 1.3). This allows for spread in a heterogeneous medium.

Richards' idea [69] was to employ a Huygens' principle for the growth of such a curve, as follows. We imagine that each point $(x(t,s), y(t,s))$ on the fire perimeter $\Gamma(t)$, in small time dt, an ellipse grows in the principle spread direction with parameters $a(t,s)$, $b(t,s)$, and $c(t,s)$ exactly as if it were

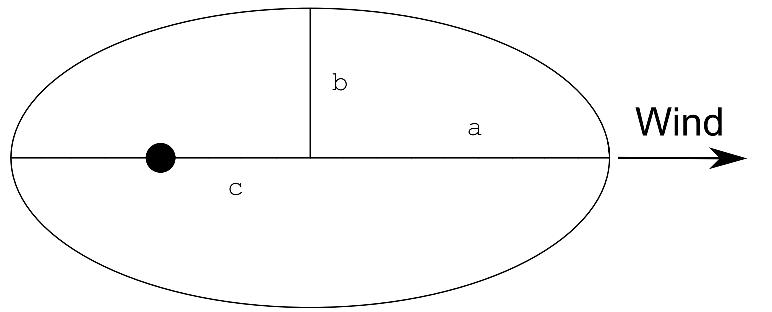

Figure 1.2: Elliptical growth, starting from a point ignition at the center of the ellipse, for homogeneous spread conditions. We assume that the principal rate of spread occurs to the right in the diagram, and we assume direction of spread is determined by the right-pointing wind (ignoring the effect of slope). The parameters a, b, and c are provided by the Fire Behaviour Prediction system, and correspond to the front, flank, and backing rates of spread respectively.

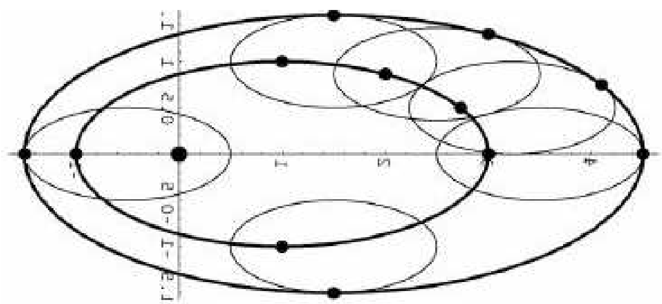

Figure 1.3: Huygens' principle for elliptical fire spread, starting from an ellipse. The curve $\Gamma(t+\Delta)t$, depicted by the larger ellipse, is the envelope of the family of smaller ellipses, which are assumed to grow at each point along the curve $\Gamma(t)$, during time Δt.

an isolated fire growing under the locally homogeneous conditions occurring instantaneously at location (x, y) at time t.

Richards derived a system of hyperbolic PDE's corresponding to such a growth, by means of a transformation which maps ellipses to circles [69]. We make the following definitions. Define the outward unit normal vector $\overrightarrow{n}$, displacement vector $\overrightarrow{c}$, and transformation matrix A by

$$A = \begin{pmatrix} a\cos\theta & -a\sin\theta \\ b\sin\theta & b\cos\theta \end{pmatrix},$$

$$\overrightarrow{n} = \begin{pmatrix} y_s \\ -x_s \end{pmatrix}, \overrightarrow{c} = \begin{pmatrix} c\sin\theta \\ c\cos\theta \end{pmatrix}.$$

In the above, θ denotes the angle between the wind direction and the principal spread direction (depending on the topography, these may not be the same).

Under the assumption that the ratio a/b is locally constant, Richards derived the following deterministic system for the local evolution of the fire perimeter,

$$\frac{\partial}{\partial t}\begin{pmatrix} x(s,t) \\ y(s,t) \end{pmatrix} = \frac{A^T A\overrightarrow{n}}{||A\overrightarrow{n}||}. \tag{1.1}$$

The model presented in Equation (1.1) was originally phrased in a different form [69], with the form (1.1) first appearing in [14] (published in 2010).

Equation (1.1) is employed in both the PROMETHEUS [89] and FARSITE [34] fire simulators. The numerical solution employs the marker method, in which one discretizes the curve into a finite number of points, then traces the evolution of these points according to a finite difference approximation to (1.1).

Such numerical methods are hindered by complications such as the crossing of trajectories, and the formation of internal loops as marker particles cross each other [14]. Specific algorithms have been developed to address these concerns [14], but a more promising approach is the level-set approach, which is described in the monograph by Sethian [80].

The level set method implicitly describes the fire evolution described in (1.1). Let us embed our curve $\Gamma(s,t)$ as the zero-level set of a smooth function ϕ,

$$\phi(\Gamma(s,t),t) = 0. \tag{1.2}$$

By differentiating the latter with respect to t, we obtain

$$\frac{d}{dt}\phi = \phi_t + \nabla\phi \cdot \Gamma_t. \tag{1.3}$$

We suppose again that our curve grows locally according to Huygens' principle for ellipses. Then equation (1.1) provides an expression for Γ_t, and using the fact that the outward normal is given by $n = \frac{\nabla\phi}{||\nabla\phi||}$, we see that Equation (1.3) can be written:

$$\phi_t + ||A\nabla\phi|| = 0. \tag{1.4}$$

The Equation (1.4) is of Hamilton-Jacobi type [33]. The level set method is a numerical method developed in [80] for solving (1.4), which resolves a number of the issues with the finite difference scheme for (1.1). In particular, the zero-level set of ϕ may contain two simple closed curves, corresponding to separate fires. The level set method allows for effortless merging of such separate interfaces, a major challenge facing finite difference schemes.

The implementation of an elliptical level-set formulation, in the context of forest fire modelling, was first suggested and explored by Anne Bourlioux as part of the MITACS project 'Forest Fire Spread in Heterogeneous Landscapes', and publications of this method are under preparation.

1.2.4 Model types: probabilistic versus deterministic

The Richards model (1.1) for fire front propagation at the macroscale introduced in the preceding subsection is deterministic, in the sense that given an initial curve $\Gamma(0)$, we will always obtain the same curve $\Gamma(t)$ at time $t > 0$. This is in part because the fire-atmosphere interaction is ignored, with a diurnally-varying but otherwise static windflow prescribed over the terrain in advance of simulation [89]. The rapid variation in local winds are not accounted for, and there is no accounting for in-stand variability in the fuel.

It is physically improbable that a given initial curve will always evolve into the same final curve, which suggests that a probabilistic approach to the spread of wildland fire may be more appropriate. Further, as we have seen, the spotting process is fundamentally stochastic in nature.

In the integro-PDE models we derive in Chapter 2, the stochastic aspect of the process is captured in the *spotting distribution*, while the i-PDE models themselves are deterministic in the sense that a given initial condition always leads to the same evolution. The solution describes the expected fire probability. A major advantage of our modelling approach is that rather than averaging the behaviour of Richards' model for multiple evolutions, with slightly varying winds so as to obtain a spatial expected-fire-probability map (a computationally very expensive endeavour), in our model a single simulation can reveal the spatial expected-fire-probability map.

1.3 Travelling wave models from invasion ecology

The first example of a travelling invasion front was presented in 1937 [35], as a model for the spread of an advantageous allele of a gene in a diploid population. The model takes the form of a reaction-diffusion equation for a density $u(x,t)$ for $x \in \mathbb{R}$ and $t \geq 0$,

$$\frac{\partial u(x,t)}{\partial t} = \frac{\partial^2 u(x,t)}{\partial x^2} + r\, u(x,t)(1 - u(x,t)), \tag{1.5}$$

where $r > 0$ is the intrinsic growth rate, and the population's carrying capacity is $u = 1$. At any point $\tilde{x} \in \mathbb{R}$ where $u(\tilde{x}, 0) > 0$, then asymptotically the population will approach its carrying capacity, i.e. $\lim_{t\to\infty} u(\tilde{x}, t) = 1$.

To find travelling wave solutions to (1.5), we look for a solution $u(x,t) = U(x - ct)$, where c is the travelling wave speed, and U describes the constant shape of the wave. We further require that $\lim_{t\to-\infty} u(x,t) = K$, and $\lim_{t\to\infty} u(x,t) = 0$.

Fisher found that there is a unique constant c_* such that the equation has a *travelling wave solution*, with speed $c \geq c_*$, and no traveling wave solutions with slower speeds [35]. Kolmogorov, Petrovsky and Pishkunov obtained the same types of solutions with a more general equation $u_t = u_{xx} + f(u)$ [45], with the so-called KPP condition $f(u) \leq f'(0)u$. Since these pioneering results, many people have investigated travelling waves for reaction-diffusion type equations. Many examples are presented in the monograph by Britton [19].

Integro-difference equation models are continuous space, discrete time models for a species which has two phases in its biological life, namely reproduction and dispersal. These two phases are assumed to be non-overlapping. Results from these models applied to biological dispersal provided much motivation for this thesis. In particular, the authors in [47] found accelerating solutions when the redistribution kernel in the integral term was 'fat'-tailed. In addition, the results in [51] suggested that different dispersal kernels could lead to different invasion speeds.

Integro-differential equations can be seen as the continuous space, continuous time analogues of integro-difference equations. Recently, integro-differential equations with 'fat'-tailed kernels have been shown to give rise to accelerating waves ([36], [41]). This is further reason to examine whether acceleration is possible in the models for fire spread which we derive in Chapter 2.

1.4 Thesis flowchart

In our thesis, we will examine integro-differential equation models, which are continuous in space and time. This section is intended as a guide to the flow of information in this thesis. In Figure 1.4, we show the connections between the various chapters.

In Chapter 2, we derive integro-PDE's (i-PDE'S) for wildland fire spread, including spotting. However, we must determine the spotting redistribution kernels appearing in the i-PDE models, which is the focus of Chapters 3 through 5.

In Chapter 3, we introduce a new model for firebrand transport and combustion, and investigate its qualitative properties. We also introduce the notion of the *asymptotic landing distribution* $\mathbb{L}(x, m)$, which is the density of firebrands with mass m which eventually land at location x.

In Chapter 4, we review a number of submodels for the various subprocesses which govern spotting. These are physical or empirical models from the literature which describe firebrand generation, launching, transport, combustion, and ignition.

In Chapter 5, we examine how the asymptotic landing distribution, given particular ignition models discussed in Chapter 4, gives rise to the *spotting distribution*. We examine specific examples of the spotting distribution. These spotting kernels can be used to discuss the probability of wildfire breaching.

In Chapters 6 and 7, we return to the models from Chapter 2, to discuss the effect of spotting on the rate of spread and possible acceleration of wildland fires. The spotting distribution becomes the *spotting kernel* in the integral term of our i-PDE models.

In Chapter 6 we take an analytic approach, examining travelling wave solutions to the one-component fire probability integro-differential equation. We derive solutions for the wave speed, and demonstrate analytically conditions under which accelerating solutions are exhibited.

In Chapter 7, we primarily examine numerical solutions to the i-PDE models derived in Chapter 2, for the full model, which incorporates the available fuel fraction. Travelling pulse solutions for the instantaneous fire probability are examined, in the spotting-dominated case. These pulses are shown to depend on the kinetics of combustion, as well as the spotting distribution chosen.

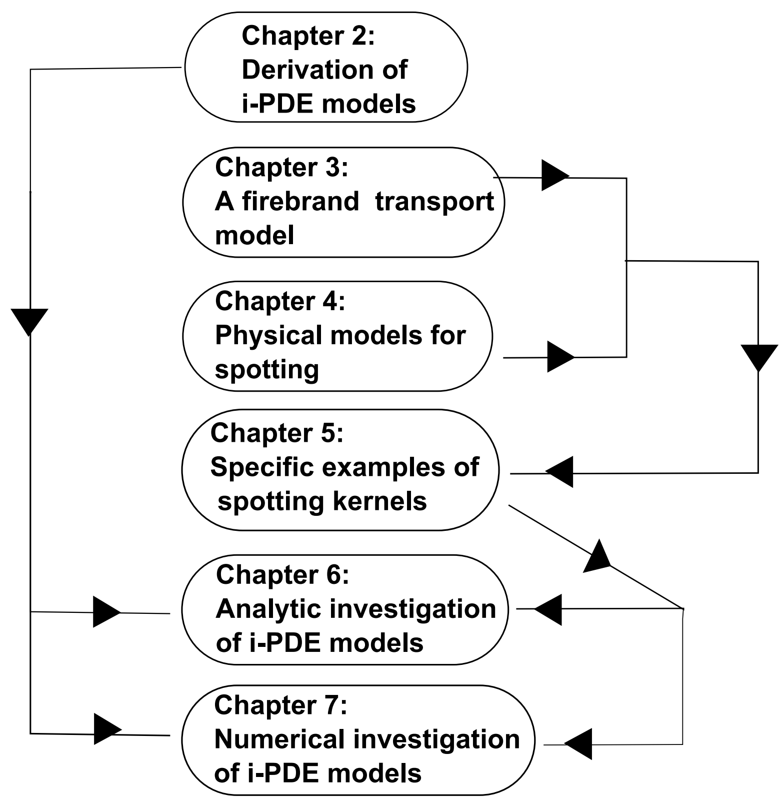

Figure 1.4: The organization of the thesis is indicated in this flowchart. The lines with arrows indicate the dependence of each chapter. For example, though we derive our central i-PDE model in Chapter 2, we do not return to it until Chapters 6 and 7 (which may be read independently).

Chapter 2

Derivation of a probabilistic model for the spread of wildfires including non-local spread by spotting

2.1 Chapter Introduction

In this chapter, our goal is to derive models for the spread of a wildfire, including both local dispersal, the interaction of the fire with fuel (i.e. combustion/heat loss), and non-local dispersal by spotting. Since the spotting, combustion and local spread processes occur continuously in space and time, we will derive continuous-time models for these processes in terms of discrete-time transition probabilities.

The first model we present is a discrete-space, discrete-time birth/death and jump process model for the expected fire probability density u and total available fuel load v, derived and explained in Sections 2.2-2.4. We then take macroscopic limits of these jump processes, first arriving at a delayed integro-partial differential equation system, (2.31) and (2.36) in Section 2.5.

In Section 2.2 we present a stochastic model for fire spread, in discrete space and time. For clarity in what follows, we also assume that firebrands move, in the horizontal direction, at the same velocity as the ambient local wind velocity. In this Chapter we assume both horizontal and vertical wind velocities are constant, though in the following three chapters we will develop a more accurate depiction of the transport and combustion of firebrands.

In Section 2.3 we discuss the launching probability. We make a simplifying assumption, namely that the probability of launching at a location is equal to the expected fire probability at that location. We eventually identify the expected fire probability with the expected fire spotting probability, in the case of extreme burning conditions.

For the purpose of analysis and applications, we discuss quasi-steady state assumptions in Section 2.6, leading to the non-time-delayed model (2.39). We also describe an approximation, which we refer to as the one-component model later, in which we assume $v = 1$ everywhere, so that our model reduces to a single equation for u. In Section 2.6.3 we generalize the latter equation for a more general local movement operator, described by Equation (2.44), following our discussion of anisotropic diffusion in Section 2.4. This anisotropic diffusion arises because of the greater local spread rate in the wind direction.

In Section 2.6.5 we discuss many simplifications of the model (2.39), one of which has recently been shown to permit accelerating wave-like solutions in the paper by Jin and Lewis [41], in the case of a 'fat-tailed' asymmetric dispersal kernel. It is one of our goals to show similar results for integral kernels derived from the wind-driven spotting process, which are inherently asymmetric. The derivation of such kernels is the subject of Chapters 3 through 5. We will also derive an expression for the effect of spotting on the rate of spread from the same paper.

The models derived in this chapter all depend on the so-called spotting kernel (distribution) $\mathbb{S}(y)$, which we will derive in Chapters 3 through 5, by introducing a separate framework for describing the transport and burning processes. There will be no further discussion of our i-PDE models until Chapters 6 or 7. Hence the reader may feel no loss of continuity proceeding directly to either Chapters 6 or 7 after reading this chapter.

It is important to state here that though we start from a very general jump process, in our later analysis we will restrict our attention to a homogeneous, but possibly anisotropic medium. The assumption of homogeneity implies that spread conditions are the same at each point in space. The assumption of anisotropy implies that the spreading speeds may depend on direction. We assume spotting occurs only from left-to-right, which will lead to an asymmetric spotting kernel,

We also must account for the increased local rate of spread in the wind direction, which we model with anisotropic diffusion, and the addition of an advection term. This explains how at a given point, the local spread in the wind direction is greater than the corresponding spread rate perpendicular to the wind, and consequently how our medium is anisotropic.

2.2 Derivation of a discrete probabilistic model for linefire spread with spotting

We would like to model line-fire spread, in which the fire propagates essentially as a front into the available fuel. Such fires occur in prescribed fires, e.g., in experimental burns [5], as well as in natural fires [40].

As an example of how a line fire may occur in natural fires, there are several reported cases where homogeneous spread conditions result in large fires which spread in a 'cigar'-like shape [40], with the interior of the ellipse burnt out. If the wind now changes so that it points perpendicular to the major axis of this burning front, an approximate line fire results as the direction of spread changes to point into the wind.

From a mathematical perspective, considering line fires allows us to reduce the number of independent variables in the problem. Consider that it is always possible to choose our Cartesian (x, y) coordinate system for the plane so that the line fire at a given time is parallel to the y-axis. The x-direction is thus normal to the line fire at each point, and it is only spread in the normal direction (often called the fire's rate of spread [40]) which is relevant. This is illustrated in Figure 2.1.

Hence we will develop spatially one-dimensional models, where the variable x is chosen as in the preceding paragraph as our spatial variable. We ignore for now variations in topography.

Let $X(x, t)$ denote a random variable for the occurrence of a fire at location x and time t. We assume that $X(x, \cdot)$ describes a Poisson process with rate

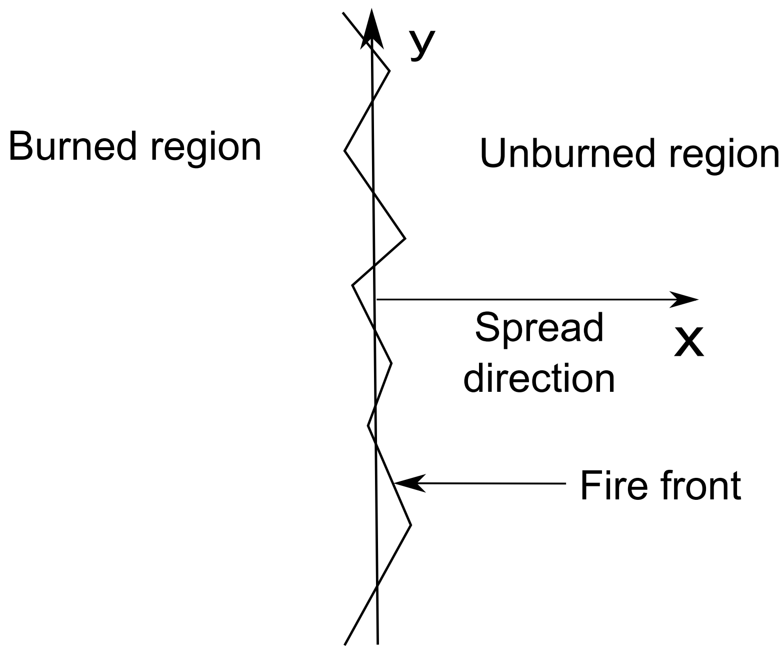

Figure 2.1: Shown is the basic fire scenario in the plane considered in this Chapter. The jagged fire front is represented by a line, and the wildfire front tracking problem is one-dimensional - we consider only spread in the positive x-direction. The left half plane represents the burned region, and the right half plane represents available fuel. The fire front forms the boundary separating these disjoint regions of the plane.

$\lambda = u(x, t)$. Then the expectation E of X depends on space and time,

$$E(X(x, t)) = u(x, t). \tag{2.1}$$

Let $A(x, t)$ be another process which contributes to or removes from the local fire probability. Then we have:

$$\begin{aligned} E(X(x, t) + A(x, t)) &= E(X(x, t)) + E(A(x, t)) \\ &= u(x, t) + E(A(x, t)), \end{aligned} \tag{2.2}$$

since the expectation is linear.

Hence when we model on the level of expectations of a Poisson process for fire occurrence, then different contributions from local spread, combustion, and spotting can be considered to be additive. In what follows, we model directly on the level of expectation of fire $u(x, t)$, i.e. we model directly at the mean field equations.

For convenience, we call $u(x,t)$ defined in (2.1) the "fire probability", while it is understood that $u(x,t)$ really denotes the expected fire probability. Note that this interpretation requires no upper limit on $u(x,t)$, and the probability distribution function for $X(x,t)$ is

$$F(t) = 1 - \exp\,(-\int_0^t u(x,s)\;ds). \tag{2.3}$$

We divide the real line into an even-spaced lattice, with the interpretation that this represents the region through which the fire line may progress. Let i, j be integers. We label points on the lattice $x_i := i\Delta x$, where Δx is the distance between lattice points. Similarly we discretize the non-negative time axis into points $t_j := j\Delta t$, where Δt is a fixed time-increment.

We will make the assumption that there is a fixed characteristic scale

$$\frac{\Delta x}{\Delta t} := w, \tag{2.4}$$

where $w > 0$ is the mean windspeed in the direction of fire spread. The direction of the mean windspeed is thus the positive x-direction.

We will also assume that spotting occurs only in the wind-direction, and that firebrands travel horizontally at the same speed as the wind (the latter is a good approximation, as described in Chapter 4), while local spread may occur in either direction following a spotting event ahead of the main front. So in considering the spotting process, we are only interested in firebrand launching events which occurred to the *left* of our current position, since no firebrands travel to the left.

In general, there is an increased local rate of spread in the wind direction, relative to the back rate of spread. These rates are known for a variety of spread conditions, including different fuel types, weather and wind, and topography, from data analysis of real world fire experiments [40].

We begin our modelling with the discrete mean field equations. The quantity $u_i(t_j) \in [0,1]$ is the discrete expectation that there is a fire burning at location x_i and at time t_j, and will refer to it as the fire probability.

Second, the total fuel loading fraction is denoted by $v_i(t_j) \in [0,1]$. This

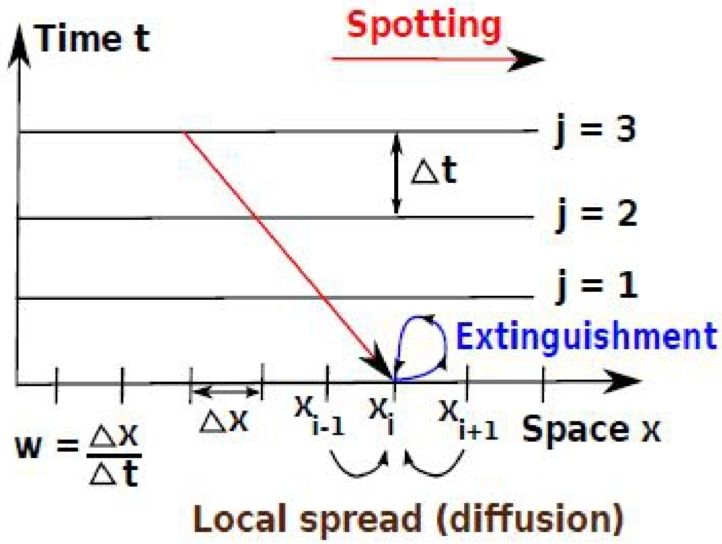

Figure 2.2: Here we discretize the plane uniformly, so that points are separated a finite distance Δx from each other, and we advance forward in timesteps of magnitude Δt. Also shown are the local spread, combustion, and extinguishment processes which act to change the fire probability $u_i(t)$. The diagonal arrow represents a spotting event indicates that occurs at time $t - \Delta t$, such that firebrands from x_{i-1} were launched which reach x_i at time t. Similarly, firebrands from location x_{i-2} and x_{i-3} reach location x_i at time t, launched at times $t - 2\Delta t$ and $t - 3\Delta t$ respectively.

variable describes the combustible material at location x_i and at time t_j. If $v_i(t) = 0$ (as in the case of no fuel being present) then no fire is possible at that location, while $v_i(t) = 1$ means no combustion has occurred at that location.

Our model takes the form of a space-jump and birth-death process for the fire probability, and a coupled death-process for the available fuel. The space-jump process for the fire probability accounts for both the local spread between neighbouring lattice points, as well as non-local spread due to spotting. The distinct processes are illustrated in Figure 1.1 from Chapter 1, and in Figure 2.2.

The coupling between the change in fire probability and available fuel is analagous to combustion, and we investigate phenomenological models for this interaction in a later subsection. More general space-jump processes are investigated in [7], while the models discussed here are based roughly on a model for cancer spread introduced in the thesis by Greese [39].

Given some initial distributions $\{u_i(0) \mid i \in \mathbb{Z}\}$ and $\{v_i(0) \mid i \in \mathbb{Z}\}$ when $t = 0$, where $\mathbb{Z}$ denotes the integers, we propose the following discrete-time, discrete space fire transport model, for any *non-negative integer* t:

$$\begin{aligned} u_i(t+1) = u_i(t) + \underbrace{k_{i,i-1}u_{i-1}(t) + k_{i,i+1}u_{i+1(t)}}_{\text{Local Spread}} \\ + \underbrace{\sum_{j=1}^{\infty} S_{i,i-j}(u_{i-j}(t-(i-j)\Delta t), v_i(t))}_{\text{Spotting}} + \underbrace{f\left(u_i(t), v_i(t)\right) u_i(t)}_{\text{Growth and decay}}, \end{aligned} \tag{2.5}$$

where $k_{i,j}$, $S_{i,j}$ and $f(u_i(t), v_i(t))$ are explained below.

First we examine the local spread terms on the right hand side of (2.5). The term $k_{i,j}$ denotes the probability that a fire at location x_j spreads to location x_i in a given time step. We notice that the contribution to $u_i(t+1)$ due to local spread involves only the points immediately to the right, and left, of the point x_i. Unlike many other space-jump models, here the fire probability $u_i(t)$ is not conserved, so no fire probability is lost due to local spread in a given time step. We will discuss these probabilities in detail in Section 2.3.

The final term $f(u_i(t), v_i(t))u_i(t)$ describes the discrete-time birth and death process, due to combustion or heat loss. We will describe several phenomenological models for combustion in Chapter 4, and we postpone specific functional forms until then, when we will present their continuous-time analogues. However, in order to introduce an evolution equation for $v_i(t)$, let's say we can decompose the birth-death term f into combustion and heat loss terms:

$$f(u_i(t), v_i(t)) = \underbrace{c(u_i(t), v_i(t))\ v_i(t)}_{\text{Combustion}} - \underbrace{\delta}_{\text{Linear heat loss to environment}} \tag{2.6}$$

The evolution equation for the available fuel thus has the general form:

$$v_i(t+1) = v_i(t) - \gamma c(u_i(t), v_i(t))\ v_i(t). \tag{2.7}$$

The constant γ will eventually be connected, in Chapter 7, to the efficiency with which the available fuel is able to increase the probability of having a fire, due to combustion.

In Section 2.2, we discuss the summation appearing in (2.5), and in particular the spotting probability $S_{i,i-j}(u_{i-j}(t-(i-j)\Delta t), v_i(t))$.

2.3 Determining the discrete spotting probability

2.3.1 Separating the launching and transport processes

In this section, we will focus in the spotting term $S_{i,i-j}$. In words, we say $S_{i,i-j}$ is the conditional probability that there was a fire at location x_{i-j} at time $t-(i-j)\Delta t$, and it then launched firebrands which are wind-transported and land at location x_i at time t, and ignite a new fire. Since we are assuming spotting occurs only from left to right, it follows that the spotting term is zero if $i-j \leq 0$.

Further suppose that the launching and transport processes are independent, so we can split up the probability

$$\begin{aligned} S_{i,i-j}(u_{i-j}(t-(i-j)\Delta t), v_i(t)) &:= \\ \underbrace{\pi_{i,i-j}(u_{i-j}(t-(i-j)\Delta t))}_{\text{Launch}} \cdot \underbrace{\mathcal{T}_{i,i-j}(u_{i-j}(t-(i-j)\Delta t), v_i(t))}_{\text{Transport and ignition}} \end{aligned} \tag{2.8}$$

In the latter equation, the term $\pi_{i,i-j}(u_{i-j}(t-(i-j)\Delta t))$ represents the probability that there was a fire launching firebrands at location x_{i-j} at time $t-(i-j)\Delta t$, while the term $\mathcal{T}_{i,i-j} = \mathcal{T}_{i,i-j}(u_{i-j}(t-(i-j)\Delta t), v_i(t))$ represents the probability that those firebrands land at x_i at time t and start a new fire. The dependence on $v_i(t)$ corresponds to the fact that the probability of ignition at x_i depends on the presence of available fuel.

2.3.2 The launching probability π

In general, there is a buildup time after ignition before the fire reaches the intensity required for spotting to occur [40]. In the context of our model, one might assume a threshold value $\underline{u}$ (analagous to a minimum intensity or temperature) required for spotting to occur. Using the Heaviside step function $H(u)$, one could write:

$$\pi_{i,i-j}(u_{i-j}(t-(i-j)\Delta t)) = H(u_{i-j}(t-(i-j)\Delta t)-\underline{u})\; u_{i-j}(t-(i-j)). \quad (2.9)$$

If we assume that the buildup time is negligible compared to the time scale associated with the dispersal process, as may occur in extreme fire scenarios where the fuel is very dry, we are lead to our main assumption about the launching probability:

$$\pi_{i,i-j}(u_{i-j}(t-(i-j)\Delta t) = u_{i-j}(t-(i-j)\Delta t). \quad (2.10)$$

Given the assumption on π described in (2.10), we are assuming that the probability that a fire is *spotting* at location x_i and at time t is equal to $u_i(t)$. This assumption will be crucial in much of the mathematical analysis to follow.

2.3.3 Transport and ignition probability $\mathcal{T}$

It is not so simple to separate the transport and ignition probabilities. The firebrands are combusting during transport, and the probability of ignition depends on the exchange of energy between burning landed mass and the surrounding terrain. For example, the *transport time* t^* which is explored in detail in Chapter 5, plays a role in determining ignition, since combustion ensures that firebrands which take too long to reach their targets will already be burned out, and thus be unable to generate a spot fire.

It will be the focus of Chapter 3 to develop a new model to study the launching of firebrands above a powerful wildland fire, and their subsequent transport and combustion through the atmosphere back towards the ground. This model will incorporate realistic models based on physics and experiments already existing in the literature on spotting. In this chapter we will focus on a simple situation, where there is a constant wind speed $w > 0$ and firebrands fall with constant terminal velocity v. In reality the velocity v will change with time due to combustion, and we discuss this in detail in Chapter 4, though we ignore this complication for now.

Assume a large fire launches a vertical distribution of N total firebrands, with corresponding probability density $\phi(z, m)$ for firebrand heights z, with mass $m = m(\rho, r, L)$, where ρ is the firebrand mass density, r is a characteristic radius for the firebrand type, and L is a characteristic length for the firebrand type. We will simply focus on $\phi(z, m)$.

To be precise, we define the *vertical launching distribution* $\phi(z, m)$, such that for an impulse release of firebrands we have:

$$1 = \int_0^\infty \int_0^{\overline{m}} \phi(z, m) dm dz, \tag{2.11}$$

where $\overline{m}$ is the maximum possible firebrand mass.

It then follows that the total mass distribution $M(z)$, which provides the mass of N firebrands, launched at height z is given by:

$$M(z) = N \int_0^{\overline{m}} m\phi(z, m) dm. \tag{2.12}$$

In order to determine $\mathcal{T}$, we will make the simplifying assumption that the mass distribution $M(z)$ is the same where the fire is launching firebrands (i.e. where $u(x, t) \neq 0$), corresponding to a homogeneous medium.

We discretize in the vertical direction, writing $z_i = i\Delta z$ for natural numbers i. We will choose the width between grid points so that $\Delta z = v\ \Delta t$, where v is the constant vertical firebrand falling velocity. This is a natural choice of the grid width, since the firebrands fall a distance $v\ \Delta t$ during a span of time Δt. This discretization is illustrated in Figure 2.3.

Consider that a fire at location $x_{i-j} = x_i - j\Delta x$ will have firebrands released from heights $z_{i-j} = (i - j)\Delta z$ at time $t - (i - j)\Delta t$, which reach the ground at x_i at exactly time t. We would like to determine the mass $M_{i,i-j}$ which will reach x_i at time t, since we will make the assumption that ignition depends only on landed mass, which has been justified in a variety of experimental contexts [90].

To determine $M_{i,i-j}$, first we consider that the mass $M(z_{i-j})$ is released at height $(i - j)\Delta z$, at time $t - (i - j)\Delta t$, at location x_{i-j} is determined from Equation (2.12),

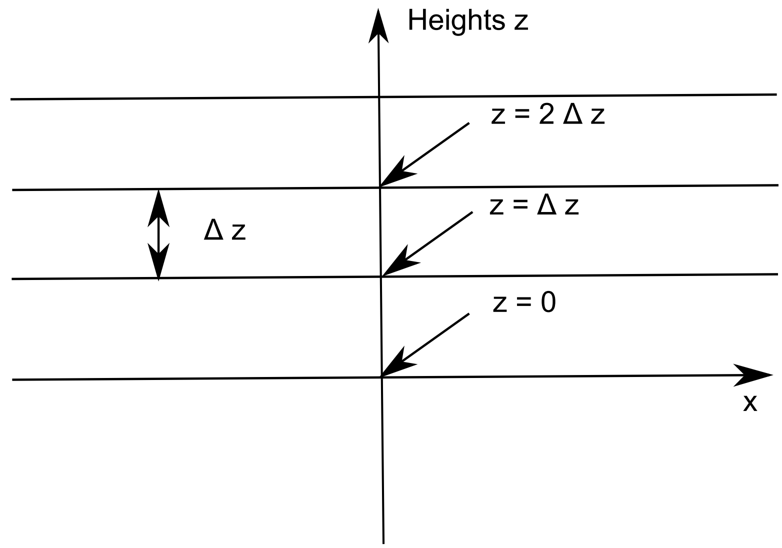

Figure 2.3: Shown is our discretization of heights z, where $\Delta z = \nu \Delta t$.

$$
\begin{aligned}
M(z_{i-j}) &= N \int_0^{\overline{m}} m\phi((i-j)\ v\ \Delta t, m)dm \\
&= N \int_0^{\overline{m}} m\phi((i-j)\frac{v}{w}\Delta x, m)dm,
\end{aligned} \tag{2.13}
$$

the latter equation following from the identity $w = \frac{\Delta x}{\Delta t}$.

Next, we must account for mass loss due to combustion during transport. Later, in Chapter 4, we will introduce several models from the literature which give realistic descriptions of combustion. Here we keep things abstract, and introduce the *discrete combustion operator* $C_{i-j}(m, \Delta t)$, which maps a mass m at time t into what the resulting mass will be $(i-j)\Delta t$ time units later. It follows that the landed mass $M_{i,i-j}$ is given by:

$$M_{i,i-j} = C_{i-j}(M(z_{i-j}), \Delta t) \tag{2.14}$$

Finally, our assumption that ignition is only a function of landed mass means we can define the *ignition operator* $E[m] \in [0, 1]$, which gives the probability that a firebrand with mass m generates a spot fire. In Chapter 5 we will provide a variety of functional forms for $E[m]$. In terms of the mass $M_{i,i-j}$ described in (2.14) and its corresponding integral formula (2.13), we can introduce a description of the transport and ignition operator $\mathcal{T}$ in terms of the ignition operator,

$$\mathcal{T}_{i,i-j} = E[M_{i,i-j}] = E[C_{i-j}(M(z_{i-j}), \Delta t)]. \tag{2.15}$$

Remark: The formula (2.15) provides a transport and ignition operator for the *total mass* which lands at x at time t. Experiments show that different masses have different rates of combustion [54], so this is only an approximate spotting distribution. Later, in Chapter 5, we will derive a model for the spotting distribution which takes into account the *mass distribution* which is launched at a given height, and which accounts for the burning of individual firebrands as opposed to just the total mass. Nevertheless, in the case of non-intersecting spatial trajectories, Equation (2.15) could provide a decent approximation to the true spotting kernel.

2.4 Integrating local spread, continuous limit

We are interested in discussing the local spread term in the model (2.5), namely the term

$$k_{i,i-1}u_{i-1}(t) + k_{i,i+1}u_{i+1}(t),$$

where we recall that t is a nonnegative integer.

As discussed previously, this is the augmentation in u_i due to spread from its immediate neighbours in a given time step. We will be interested in continuous limits of this discrete model, and to do so we will investigate the simplified equation

$$u_i(t+1) = u_i(t) + k_{i,i-1}u_{i-1}(t) + k_{i,i+1}u_{i+1}(t). \tag{2.16}$$

We will introduce densities corresponding to the terms in (2.16),

$$u_i(t) \approx u(x,t)\Delta x \Delta t. \tag{2.17}$$

with the interpretation that the expectation of having a fire in the $[x+\Delta x) \times [t, t+\Delta t)$.

For the local process we can assume that we have a redistribution kernel k

defined by:

$$
\begin{aligned}
k_{i,j} &\approx \lim_{\Delta t\to 0, \Delta x\to 0} k(x,y)\frac{\Delta t}{(\Delta x)^2}, && i\neq j,\\
k_{i,i} &:= \lim_{y\to x, \Delta x\to 0} k(x,y)\ \frac{\Delta t}{(\Delta x)^2} = 0, && \text{for all } \Delta t > 0.
\end{aligned} \tag{2.18}
$$

The Equation for $k_{i,i}$ in the previous system (2.18) implies that the probability of having a fire at location x_i is neither augmented nor reduced by the presence of a fire at location x_i.

Employing these densities in Equation (2.16), we obtain

$$
\begin{aligned}
&u(x,t+\Delta t)\Delta x\Delta t - u(x,t)\Delta x\Delta t \qquad (2.19)\\
&\approx (\Delta x)^{-2}\Delta t\Delta x\Delta t\left(k(x,x-\Delta x)u(x-\Delta x,t) + k(x,x+\Delta x)u(x+\Delta x,t)\right).
\end{aligned}
$$

The next step is to expand the kernel $k(x, x \pm \Delta x$ in a Taylor series in its second argument, about x,

$$
k(x,x\pm\Delta x) \approx k(x,x) \pm \Delta x\left(\frac{\partial k(x,\tilde{x})}{\partial \tilde{x}}\right)_{\tilde{x}=x} + \frac{\Delta x^2}{2}\left(\frac{\partial^2 k(x,\tilde{x})}{\partial \tilde{x}^2}\right)_{\tilde{x}=x} + O(\Delta x^3) \tag{2.20}
$$

Provided our solution is sufficiently smooth, we may similarly expand the fire density $u(x \pm \Delta x, t)$ in a Taylor series in its first argument, about (x, t):

$$
u(x\pm\Delta x,t) \approx u(x,t) \pm \Delta x\left(\frac{\partial u(x,t)}{\partial x}\right) + \frac{\Delta x^2}{2}\left(\frac{\partial^2 u(x,t)}{\partial x^2}\right) + O(\Delta x^3). \tag{2.21}
$$

Next we employ the formulae derived in Equations (2.20) and (2.21) into the model (2.19). Cancelling factors of Δx and Δt from both sides of Equation (2.19), we obtain:

$$
u(x,t+\Delta t) - u(x,t) \approx \Delta x^{-2}\Delta t\left(2k(x,x)u(x,t) + \Delta x^2 J\right), \tag{2.22}
$$

where the quantity J is defined by:

$$
\begin{aligned}
J &= u(x,t)\frac{\partial^2 k(x,\tilde{x})}{\partial \tilde{x}^2} + 2\frac{\partial u(x,t)}{\partial x}\frac{\partial k(x,\tilde{x})}{\partial \tilde{x}} + \frac{\partial^2 u(x,t)}{\partial x^2}k(x,\tilde{x}) \\
&= \frac{\partial^2}{\partial \tilde{x}^2}\left(u(\tilde{x},t)k(x,\tilde{x})\right)_{\tilde{x}=x}. \qquad (2.23)
\end{aligned}
$$

Dividing both sides of Equation (2.22) by Δt, and using the second equation in (2.18) to deal with the first term in (2.22), we find after taking the limit $\Delta t \to 0$ that Equation (2.22) becomes a partial differential equation,

$$
\frac{\partial u(x,t)}{\partial t} = \frac{\partial^2}{\partial \tilde{x}^2}\left(u(\tilde{x},t)k(x,\tilde{x})\right)_{\tilde{x}=x} \qquad (2.24)
$$

This type of anisotropic diffusion should be used, when the mean length of the wind field is of the same order of magnitude as the flame generated by the fire. It results in a faster spread to the right than to the left, when the wind points left to right, and thus more accurately represents the local spread of a fire than its isotropic approximation.

In the case of a homogeneous medium, where in addition the probability of local spread is equivalent from the left and right (the 1-D analogue of isotropy), the diffusion coefficient D is constant (and given in terms of the discrete transition probabilities $k_{i,j}$ by Equation (2.29)). Put otherwise, the spreading probabilities are the same at each spatial location x, and in each direction, and we obtain the simple diffusion model:

$$
\frac{\partial u(x,t)}{\partial t} = D\frac{\partial^2 u(x,t)}{\partial x^2}. \qquad (2.25)
$$

In the spotting-dominated case, which we consider in Sections 2.6 and 7.7, the assumption of local isotropy is justified, since spotting completely dominates the spread mechanism. However, in general the local spread is greater in the wind direction, since the wind points the flame closer to the ground, so that radiant energy is transferred more quickly to the right than to the left [68].

The reader will notice that in Equation (2.24), and in particular the expansion (2.23), the presence of birth/death , advection, and isotropic diffusion terms. These are, respectively, $u(x,t)\frac{\partial^2 k(x,\tilde{x})}{\partial \tilde{x}^2}$, $2\frac{\partial u(x,t)}{\partial x}\frac{\partial k(x,\tilde{x})}{\partial \tilde{x}}$, and $\frac{\partial^2 u(x,t)}{\partial x^2}k(x,\tilde{x})$. We will primarily focus on the approximation (2.25).

A proper explanation of the transition probabilities and their derivatives requires detailed knowledge of how fire spreads at the local scale, due to radiation, advection, and conduction of heat [68]. At this scale, the fuel may take on several phases (i.e. solid, liquid or gas), and is structured in terms of the ground, ladder, and crown fuel distributions, the availability of oxygen, in addition to topography. Certainly the medium is heterogeneous, and a one-dimensional model seems inappropriate. Scaling up to our length scale, by homogenization of some kind, may be possible in future work. In addition, it may be possible to use the spread rates prescribed by the Fire Behaviour Prediction system [40], which are already valid at the macroscopic scale.

Remark: By considering a simple change of the discrete transition probabilities used to construct D in Equation (2.25), we could define $k_{i,i+1} := k_{i,i-1} - \epsilon w := K - \epsilon w$, where w is the windspeed and $K = k_{i,i+1} > 0$ is a constant. This corresponds to a greater rate of spread in the wind direction, and constant isotropic diffusion characterized by the constant K. Upon performing similar expansions as in this section, we are left with an isotropic diffusion term, subtracted by an advection term. The advection term is characterized by the parameters ϵ and w, and in a PDE expansion leads to an advection term $f(\epsilon, w)\frac{\partial u}{\partial x}$ appearing in Equation (2.25), so that we have a different advection-diffusion model. While we remark on this possibility, we will not pursue it further in this thesis, and we disregard the wind pushing the fire. We include, however, the wind-driven spotting.

2.5 Continuous limits of this chapter's discrete models: integro-partial differential equations (iPDE)'s for wildfire fronts

In light of the preceding subsections, we would now like to return to our models for the expected fire probability $u_i(t)$ and the total fuel loading fraction $v_i(t)$, described in Equations (2.5) and (2.7). We would also like to emphasize that we are now interested in studying a homogeneous medium.

We would like to pass to a continuous limit for the discrete models presented thus far, obtaining a model which is continuous in space and time. To this end, let us first re-write the governing Equation (2.5), incorporating the functional forms for the various probabilities derived in the preceding subsections, as

$$
\begin{aligned}
u_i(t+1) = u_i(t) + (k_{i,i-1}u_{i-1}(t) + k_{i,i+1}u_{i+1}(t)) \\
+ \sum_{j=1}^{\infty} u_{i-j}(t-(i-j)\Delta t)\mathcal{T}_{i,i-j}v_i(t) \\
+ f(u_i(t), v_i(t))u_i(t).
\end{aligned} \tag{2.26}
$$

In the first line we have nearest-neighbour interactions only, as described in Section 2.3. In the second line we see the contribution from spotting, where we have employed the simplest launching assumptions. The transition and ignition operator $\mathcal{T}$ is described in the derivation leading to Equation (2.15). We recall that we have discretized time, so that t is a nonnegative integer.

We now introduce the densities:

$$
\begin{aligned}
u_i(t) &\approx u(x,t)\Delta x\Delta t, \\
v_i(t) &\approx v(x,t)\Delta x\Delta t, \\
\mathcal{T}_{i,i-j}v_i(t) &\approx \mathcal{T}(x, x-j\Delta x)\Delta x\Delta t\; v(x,t), \\
k_{i,j} &\approx \lim_{\Delta t\to 0, \Delta x\to 0} k(x,y)\frac{\Delta t}{(\Delta x)^2}, \qquad i \neq j, \\
k_{i,i} &:\approx= \lim_{y\to x, \Delta x\to 0} k(x,y)\;\frac{\Delta t}{(\Delta x)^2} = 0 \qquad \text{for all } \Delta t > 0, \\
f(u_i(t), v_i(t)) &\approx f(u(x,t), v(x,t))\Delta t.
\end{aligned} \tag{2.27}
$$

In terms of these densities, the spotting term appearing in the second line of Equation (2.26) becomes:

$$
\begin{aligned}
&\sum_{j=1}^{\infty} u_{i-j}(t-(i-j)\Delta t)\mathcal{T}_{i,i-j}v_i(t) \\
&\approx \Delta t^2\Delta x \sum_{j=1}^{\infty} u(x-j\Delta x, t-(i-j)\Delta t)\mathcal{T}(x, x-j\Delta x)\; v(x,t)\Delta x.
\end{aligned} \tag{2.28}
$$

If we assume we have an isotropic medium, $k_{i,j} = k_{j,i}$ everywhere. This will lead to the simple diffusion term $D\frac{\partial^2 u(x,t)}{\partial x^2}$ on the right hand side, as described in Section 2.3. For the purpose of analyzing the spotting dominated case as in Section 7.6, this assumption is valid, since spread by diffusion is negligible. We should note that the diffusion coefficient is calculated by taking the limit [74]:

$$D := \lim_{\Delta t \to 0, \Delta x \to 0} k_{i,i+1} \frac{(\Delta x)^2}{\Delta t}. \tag{2.29}$$

Let us drop the local spread terms from Equation (2.26) for the moment, then divide both sides by Δt, to obtain:

$$\begin{aligned} \frac{u(x, t + \Delta t) - u(x, t)}{\Delta t} &= \\ \sum_{j=1}^{\infty} u(x - j\Delta x, t - (i - j)\frac{\Delta x}{w})\mathcal{T}(x, x - j\Delta x)\ v(x, t)\Delta x & \\ + f(u(x, t), v(x, t))u(x, t). & \end{aligned} \tag{2.30}$$

Now we want to take the continuous limit, sending $\Delta x \to 0$ and $\Delta t \to 0$. The reader will notice that the sum appearing in (2.30) is actually a Riemann sum, which will converge to an integral in the limit as $\Delta x \to 0$ (see Equation (2.31) below).

Combining the results from Equation (2.30) together with the results concerning local spread from Section 2.3, we are prepared to take the continuous limit of (2.30), obtaining the model

$$\begin{aligned} \frac{\partial u(x, t)}{\partial t} = D\frac{\partial^2 u(x, t)}{\partial x^2} + v(x, t) \int_0^{\infty} u(x - y, t - \frac{x - y}{w})\mathcal{T}(x, x - y)dy & \\ + f(u(x, t), v(x, t))u(x, t). & \end{aligned} \tag{2.31}$$

Notice that the linear time-delay appearing in the integral term in Equation (2.31), is the *landing time* required for firebrands launched from location $x - y$ at time $t - \frac{x-y}{w}$, to reach location x at time t.

Of equal importance is to note that since our medium is homogeneous, and we assume spotting occurs only from left to right, we expect the spotting transition probability $\mathcal{T}(x, y)$ to depend only on the difference $x - y$. That is,

$$\mathcal{T}(x, y) = \mathbb{S}(x - y), \tag{2.32}$$

for a new function $\mathbb{S}$, where the argument $(x - y) \geq 0$. Since spotting occurs only from left to right, it follows that $\mathbb{S}(x-y)=0$ for $x-y<0$.

When one considers the term $T(x, x-y)$ appearing in (2.31), in terms of $\mathbb{S}$ we see:

$$\mathcal{T}(x, x-y) = \mathbb{S}(x-(x-y)) = \mathbb{S}(y). \tag{2.33}$$

Substituting the righthand side in (2.33) with the corresponding term appearing in (2.31), our model for the fire probability density reads:

$$\begin{aligned} \frac{\partial u(x,t)}{\partial t} = D\frac{\partial^2 u(x,t)}{\partial x^2} + v(x,t)\int_0^\infty u(x-y, t-\frac{x-y}{w})\mathbb{S}(y)\,dy \\ +f(u(x,t), v(x,t))u(x,t). \end{aligned} \tag{2.34}$$

Finally, the continuous analogue of Equation (2.7) is derived from the following:

$$(v(x, t+\Delta t) - v(x,t))\Delta x \Delta t = -\gamma\; c(u(x,t), v(x,t)\;\Delta t\; v(x,t)\;\Delta x \Delta t, \tag{2.35}$$

and cancelling the common factor of Δx and Δt from both sides, dividing by Δt, then sending $\Delta t \to 0$, we obtain the equation governing v, namely

$$\frac{\partial v(x,t)}{\partial t} = -\gamma c(u(x,t), v(x,t)). \tag{2.36}$$

2.6 Limiting equations, and generalizations of our derived (iPDE)'s

2.6.1 A quasi-steady state assumption for the total fuel loading

For the purposes of mathematical analysis, we would like to simplify the coupled system of differential equations ((2.34), (2.36)). To this end, let us make the assumption that the combustion process is very slow compared to the dispersal process. In particular, we would like to assume:

$$\frac{\partial v(x,t)}{\partial t} \approx 0, \tag{2.37}$$

so that the total fuel loading fraction is approximately constant.

For simplicity of notation, since we consider a homogeneous medium we normalize $v(x,t) = 1$ everywhere. Physically this could correspond to a thick coniferous forest, which forms a type of continuum medium where all points may be burned. Then our problem is reduced to the solution of a single integro-partial differential equation for $u(x,t)$. This assumption will be relevant when we discuss traveling wave solutions for (2.34). Allowing solutions $v = v(x)$ would be relevant should consider spotting across obstacles, since in this case we will have $v = 0$ in the region blocking local spread.

We are thus led to consider a delayed integro-partial differential equation for $u(x,t)$, governed by

$$\begin{aligned} \frac{\partial u(x,t)}{\partial t} = D\frac{\partial^2 u(x,t)}{\partial x^2} + \int_0^\infty u\left(x-y, t-\frac{x-y}{w}\right)\mathbb{S}(y)\,dy \\ + f(u(x,t),1)u(x,t). \end{aligned} \tag{2.38}$$

This is a delayed integro-partial differential equation, with a potential non-linear birth-death term $f(u(x,t),1)$. The delay term $\frac{x-y}{w}$ is scaled by the windspeed w, which could range up to 30 metres per second. Alternatively, and in future work, we will replace the simple isotropic diffusion term by the anisotropic term (2.24), which is especially important in the case where local spread and spotting occur at approximately the same rate. Traveling wave solutions for similar models have been investigated, for example, in Thieme [87]. Such models are, however, the subject of current research and as such are quite complicated.

One thing that seems common across the modeling of invasions with non-local dispersal, is that the behavior of the model is determined largely by the redistribution kernel $\mathbb{S}(y)$ [51]. We will devote a great deal of effort, in Chapters 3 and 4, to providing a mechanistic determination of a variety of redistribution kernels.

2.6.2 Further simplification: removing the time-delay

As an important remark, we notice that the delay appearing in (2.38), namely $\frac{(x-y)}{w} := t^*$ is the *landing time*. This means t^* is the time it takes a launch of firebrands to travel from above location $(x-y)$ to location x, just in time so that this mass of firebrands reaches x at time t. Since spotting occurs from left to right only, it follows that the landing times are always positive, since we consider only values $x-y>0$.

Since there is a finite combustion lifetime for any firebrand, those whose landing time exceeds the combustion lifetime will be burnt out and unable to ignite a spot fire. Since the landing time increases with increasing launch heights, the upper bound on the possible values for heights z contained in the integral in (2.38) will be a finite number in many instances. In turn, there is an upper bound the possible time delays from launch to landing.

If we imagine the wind-driven transport process, the launching process, and the ignition process is very rapid relative to the local spread of fire (valid in the most extreme fire scenarios), we may make the extreme assumption that the time-delay t^* is neglibile in (2.38). With this assumption, we arrive at yet another simplification, namely to consider an initial value problem for $u(x,t)$ satisfying

$$\begin{aligned}\frac{\partial u(x,t)}{\partial t} = D\frac{\partial^2 u(x,t)}{\partial x^2} + \int_0^\infty & u(x-y,t)\mathbb{S}(y)\, dy \\ & + f(u(x,t),1)u(x,t).\end{aligned} \tag{2.39}$$

We will consider initial value problems on $\mathbb{R}$ for (2.39), with compactly supported initial conditions, and our only boundary conditions are that:

$$\lim_{|x|\to\infty} u(x,t) = 0. \tag{2.40}$$

We now have a single equation, which we will employ for a variety of purposes. One can think of Equation (2.39) as a model for a quasi-steady state for the dispersal process, where the non-local dispersal occurs much more rapidly than the launching of firebrands. Since this will usually be the case in extreme spotting situations, we expect that the model (2.39) should provide a reasonable approximation of the delayed equation (2.38) in a variety of fire scenarios.

Further, numerical investigations in Section 7.6, of solutions to initial value problems on $\mathbb{R}$ for (2.39), with compactly supported initial data, showed that such a quasi-steady spreading state emerges after an initial transient, at least for spotting kernels $\mathbb{S}$ which exponentially bounded. Further, even in the presence of fuel loading v, travelling pulses are shown to spread with constant shape and speed. The shape and speed may not be influenced by time delays in all cases, for these types of evolutions.

2.6.3 The diffusion operator L

Referring to the discussion in Section 2.4, the local movement can in general be accounted for by a term $L[u(x,t)]$ in the differential equation (2.39), so that we must consider:

$$\begin{aligned} \frac{\partial u(x,t)}{\partial t} = L[u(x,t)] + \int_0^\infty u(x-y,t)\mathbb{S}(y)\,dy \\ +f(u(x,t),1)u(x,t), \end{aligned} \tag{2.41}$$

Here $L[u(x,t)]$ is an elliptic differential operator, given by the right hand side of either (2.24) or (2.25), as derived in Section 2.3. We are here restricting ourselves to the case of a homogeneous, isotropic medium, so we simply have

$$L[u(x,t)] = D\frac{\partial^2 u(x,t)}{\partial x^2}.$$

2.6.4 The spotting operator $\mathcal{S}$

Given a kernel $\mathbb{S}(y)$, which in our case will be the spotting distribution $\mathcal{S}$ on $[0,\infty)$, we can extend the kernel $\mathbb{S}$ to all of $\mathbb{R}$, by defining a new kernel $\tilde{\mathcal{S}}$:

$$\tilde{\mathbb{S}}(y) = \begin{cases} \mathbb{S}(y), \, y \geq 0; \\ 0, \quad\;\; y < 0. \end{cases} \tag{2.42}$$

We associate with a density $u(x,t)$ defined on $\mathbb{R}$ the *spotting operator*

$$\mathcal{S}[u(x,t)] := \int_{-\infty}^{\infty} u(x-y,t)\tilde{\mathbb{S}}(y)\, dy. \tag{2.43}$$

With the above notations, we can rewrite our model (2.41) in the abstract form:

$$\frac{\partial u(x,t)}{\partial t} = L[u(x,t)] + \mathcal{S}[u(x,t)] + f(u(x,t),1)\; u(x,t) \tag{2.44}$$

In Chapter 5 we will determine a variety of operators $\mathcal{S}$, and in Chapters 6 and 7 we will investigate how our choice of kernel $\mathcal{S}$ affects the properties of solutions. In particular we will determine a subclass of our derived kernels for which we can guarantee existence and uniqueness of solutions in appropriate spaces of mappings, and investigate wave-like solutions.

2.6.5 The spotting-dominated case

Let us suppose that the influence of local spread is negligible, so that we can drop the local term. The result is another integro-differential equation,

$$\frac{\partial u(x,t)}{\partial t} = \mathcal{S}[u(x,t)] + f(u(x,t,1)\; u(x,t) \tag{2.45}$$

This form of the equation will be useful in our analytic investigation of accelerating traveling wavefronts, later in Chapter 6. We are motivated by analytical results for the spread of solutions, with 'fat'-tailed kernels defining $\mathbb{S}$, for an equation of very similar form to the recent paper by Yu and Jin [41]. In order to apply their results here we will require assumptions on f, $\mathcal{S}$, and the initial conditions to be specified, all of which is discussed in Chapter 6.

Physically, there are two distinct important situations we wish to consider. The first corresponds to prolific, short-to medium-range spotting, as occurs in Eucalyptus-grassland fires in Australia [31], or in urban-wildland interface fires [93]. The other is the situation where prolific long-range spotting is occurring, as occurs in intense crown fires in dense coniferous coverings in North America [26].

2.7 Chapter summary

In this Chapter we considered first a discrete-space, discrete-time model for the spread of an instantaneous expected fire probability $u_i(t)$, for t a non-negative integer, as well as the total fuel loading fraction $v_i(t)$. The model explicitly includes local spread, non-local spread by spotting, and growth/decay analagous to fire combustion. Our spread environment is one-dimensional, homogeneous, but anisotropic, since in particular the wind is assumed to point from left to right.

In subsections 2.2-2.4 we describe several assumptions we make, and the resulting simplified models. In particular, we assume that launching and the transport/ignition processes are independent. We discuss possible assumptions for the launching probability, and we merely assume that the launching probability equals the instantaneous fire probability. Implicit in this assumption is that wherever a fire exists, it is in the process of releasing firebrands, and our assumption of spatial homogeneity implies this release distribution must be the same everywhere.

We spend some time discussing the transport/ignition probabilities. We assume constant horizontal wind, and vertical falling velocity, and postpone a discussion of the validity of these assumptions until Chapter 4. We then discuss the so-called combustion operator $\mathcal{C}$, which is discussed at length in Chapter 4, and which describes how the mass of a firebrand evolves with time. An additional assumption is that the ignition of fuel beds depends only on the landed mass, and is described by the ignition operator $E[m] \in [0, 1]$ which gives the probability of ignition. We then present an approximation to the spotting distribution, which accounts only for how the total mass of firebrands evolves with time.

Next we described how to convert from our discrete-space, discrete-time transition probabilities, to continuous-space, continuous time densities. The model for u derived takes the form of a time-delayed i-PDE, where the delay is the travel time from the launching to ignition point. A simple ODE describes the evolution of v. Since such time-delayed models are difficult to analyze, we discuss how we can reduce our system to a single equation for u which does not contain a time delay. Of particular relevance is the spotting-dominated case, which we consider last, where we can ignore the effects of local spread; in this case non-local spread by spotting will be seen to really drive the invasion.

Chapter 3

Transport model for firebrands and the asymptotic landing distribution

3.1 Chapter Introduction

In this chapter, we will consider a new mathematical model which describes the transport of combusting firebrands in the atmospheric boundary layer. In Chapter 2, we used a discrete random walk model (2.26) for the fire probability, where we assumed that the mean horizontal wind and vertical terminal velocity were constant.

The new transport-type model considered in this chapter is based on conservation laws, and it will allow us to incorporate the various physical or empirically-derived models already existing in the literature. The physical models will be discussed in Chapter 4, including models for atmospheric mean windspeed, as well as firebrand generation and launching, terminal velocity and combustion, and ignition probabilities. Hence we will be able to determine spotting redistribution kernels, for the continuous models from Chapter 2, which are based on physically realistic models for the spotting subprocesses.

In this chapter, we keep things abstract, preferring to define our transport-type model and describe some qualitative features for its solutions. In Chapter 5, we will combine the model derived in this chapter with the physical processes described in Chapter 4 to derive a variety of new spotting kernels.

In this Chapter we consider only an impulse release of firebrands, with firebrands released above the fire, with distribution $\phi(z, m)$ for heights z and masses m, but only at time $t = 0$ and at location $x = 0$.

Of course, a real fire will continue to move forward, and there will be firebrands launched from locations to the right of the fire's initial location at $x = 0$, unless there is a blockage to local spread. One can regard the release of firebrands from this moving fire as a superposition of impulse releases, and this is exactly what our i-PDE models from Chapter 2 are meant to emulate. We must suppose this 'continuum' of impulse releases do not interfere with each other in the transport phase, but can augment each other's influence upon landing, and the results can be seen directly in simulations of the i-PDE models in Chapter 7.

Finally, the issue of release only at time $t = 0$ can be viewed as a mathematical approximation. If, for example, the fire reaches a barrier to local spread, but there is a town downwind, the fire will burn near the edge of burnable material for a finite amount of time. A distribution for spotfires in a such a situation, confined to a single spatial dimension, was described in [90]. In more than two dimensions, in general this problem is more challenging since one must keep track of the local fire perimeter so that knows where spotting is occurring.

In what follows, we will primarily focus on the one-dimensional model outlined later in this chapter. Let's consider again the case where the fire reaches a barrier to local spread. An alternative to the impulse release is to replace the delta-function $\delta(t)$ with the difference of two Heaviside functions $\mathbb{H}$, i.e. $p(t, x = 0, z, m) = (\mathbb{H}(t) - \mathbb{H}(t - n))$, so that the fire spots up to time $t = n$ (see Equation 3.4 below for the launch model we employ). We will not explore this type of release in this chapter, but we could in future work. In this way the delta function serves as a mathematical approximation: we assume the launching process is complete at $t = 0$, and now our task is to track where the firebrands end up.

3.2 Transport model for impulse release in the plane

3.2.1 The vertical launch distribution, spotting distribution

Suppose we have a large fire, burning so that its progress can be idealized as the progression of a fire front, the latter separating the burned and unburned regions of the plane.

The *burned region* Ω is assumed to form a simple closed domain, which means its boundary is a simple closed curve denoted by $\delta\Omega$. For points inside Ω, the fire is burned out.

The *unburned region* is the complement of Ω in the plane, and it represents fuel into which the fire front is expanding with time. We will be interested in how a given fire front progresses into an unburned region. This separation of the plane according to the fire front is illustrated in Figure 3.1.

In such models, valid at the macroscopic scale, we imagine that burning takes place only in a narrow region, at the interface between the burned and unburned regions. One then allows this region to collapse onto the curve which we denote $\partial\Omega$, by scaling the coordinates appropriately. For simplicity, we will neglect the effect of topography, so that each point along the interface is assumed to be at the same height. This assumption is generally valid for example in dense tree plantings, where we expect the most significant spotting to occur.

As described in the Chapter 1, the problem of outward curve expansion in forest fire models has been treated extensively, and used in applications such as PROMETHEUS [89] or FARSITE [34]. These models are based on Richards' curve expansion equations [69], which are a system of first-order PDE's for the fire perimeter (1.1), and in which the spread in the normal direction is given by the empirically-based fire behaviour prediction (FBP) system [40]. It should be noted that short-range spotting, up to about 30m, is already implicitly accounted for in the FBP computations [40].

Spotting models such as that developed by Albini [2] have been incorporated into curve-propagation models in an ad-hoc way [4], but these spotting

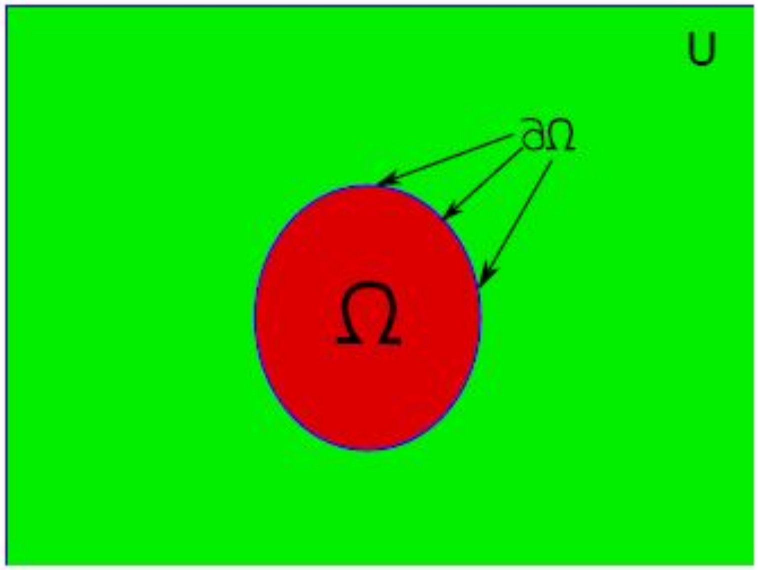

Figure 3.1: At a given instant of time, the plane is divided by the fire front into disjoint subsets, according to whether a point has been burned or not. These subsets consists of the burned region Ω, shown in a darker shade of red as an ellipsoid in this figure, and the unburned region $U := (\Omega \bigcup \delta\Omega)^c$, the latter shown in green in this figure. The boundary of the burned and unburned regions is the fire front $\partial\Omega$, and this boundary expands outwards in time as the fire burns into the unburned region.

models focus on the maximum spotting distance, rather than the downwind spotting *distribution*. The advantage of our modeling is that we will be able to obtain a downwind spotting *distribution*, which can then be incorporated into the types of continuous models considered in Chapter 2, for a variety of fire scenarios, including those where prolific long-range spotting is common.

The final goal of our efforts is to determine a continuous *spotting distribution* $\mathbb{S}(x) \in [0, 1]$, defined for points x in the unburned region U, which will characterize whether a spot fire will ignite at some future time, at location x, due to the impulse release of firebrands above $\partial\Omega$ at time $t = 0$. We also assume that there are no subsequent launching of firebrands. We will consider, as we do in Chapter 4, detailed models for spotfire generation, launching, transport, combustion, and ignition. First in this chapter we will derive a model for the impulse release of firebrands, and their subsequent transport and combustion through the atmosphere.

3.2.2 Transport model, initial and boundary conditions

We suppose that at each point along the fire boundary, and not at any point in the interior, the updraft created by the fire carries a *vertical launch distribution* $\phi(x, z, m)$ of firebrands, at each location $x \in \partial\Omega$, with height $z \geq 0$, and with mass $m \in [0, \overline{m}]$. Here the upper limit $\overline{m}$ in the domain of definition denotes the maximum possible loftable firebrand mass.

The vertical launch distribution is normalized, so that given a release of N firebrands, the total mass $M(x)$ launched above the point $x \in \partial\Omega$ is given by

$$M(x) = N \int_0^\infty \int_0^{\overline{m}} \phi(x, z, m)\, m\, dmdz \tag{3.1}$$

We interpret the total mass as the product of the total number N of firebrands, multiplied by the integral whose integrand is the probability to find a firebrand at x and height z with mass m by the mass m.

To determine the subsequent transport and combustion of the firebrands launched along the fire perimetre, we introduce the *density of firebrands* $p : (t, x, z, m) \to \mathbb{R}$, defined for $(x, z, m) \in D$ and $t \geq 0$, where

$$D = U \times [0, \infty) \times [0, \overline{m}], \tag{3.2}$$

We interpret the variables in (3.2) as time t, location x, height z and mass m.

The density p is defined so that the mass $M(t, x)$ of firebrands above location $x \in U$ at time $t \geq 0$ is given by:

$$M(t, x) = \int_0^\infty \int_0^{\overline{m}} m\, p(t, x, z, m) dmdz \tag{3.3}$$

The boundary conditions for the density p are given by:

$$p(t, x, z, m) = \delta(t)\phi(x, z, m), \qquad x \in \partial\Omega, \tag{3.4}$$

where $\delta(t)$ is the Dirac delta functional.

This boundary condition implies that no further firebrands are released from the main fire for any time $t > 0$.

It is natural to assume that the firebrand density dies off at spatial infinity,

$$p(t,x,z,m) \to 0, \qquad |x| \to \infty. \tag{3.5}$$

It is also natural to assume that the firebrand density decreases to zero with height, which leads to our final boundary condition,

$$p(t,x,z,m) \to 0, \qquad z \to \infty. \tag{3.6}$$

We finally must provide initial conditions. We suppose that initially there are no firebrands inside, or outside the burning domain when $t = 0$. Hence we have:

$$p(t=0,x,y,m) = 0, \qquad x \notin \partial\Omega. \tag{3.7}$$

Since we are assuming that no firebrands are created or destroyed after the initial launch, we are naturally led to a conservation law for the firebrand density p. We think of the independent variables (x, y, m) as coordinates in a phase space $\mathbb{D}$, defined by

$$\mathbb{D} = U \times [0,\infty) \times [0,\overline{m}]. \tag{3.8}$$

To interpret our conservation law for firebrand density evolution in phase space, we need to specify the density flux across a unit volume. We define the evolution flux vector field J for constant t by:

$$J(x,y,m) := (w^1p, w^2p, vp, fp)\,|_{(t,x,z,m)}\,. \tag{3.9}$$

We interpret $w(t,x,z,m) = (w^1(t,x,z,m), w^2(t,x,z,m)))$ as the horizontal wind velocity vector, so that w^1 is the windspeed in the x^1-direction, and w^2 is the windspeed in the x^2-direction. We will only consider the case where $w = w(z)$, so that mean windspeeds depend only on height z.

The function v denotes the vertical velocity of the firebrand density, and hence describes the change of height z. We will assume only functional forms $v(t,z,m)$, so that terminal velocity is independent of position.

The function f is the rate of combustion, and consequently determines the rate of change of mass during transport. We will consider functional forms $f(t,z,m)$.

All considered, none of the rates depend on the density p, which will be important in what follows.

We are assuming our phase space is a subset of $\mathbb{R}^4$, equipped with a Cartesian coordinate system (t, x, z, m), for which we define the divergence operator $\nabla\cdot$ in the usual way:

$$\nabla \cdot J = \frac{\partial(w^1 p)}{\partial x^1} + \frac{\partial(w^2 p)}{\partial x^2} + \frac{\partial(vp)}{\partial z} + \frac{\partial(fp)}{\partial m}, \tag{3.10}$$

where $x = (x^1, x^2)$ are coordinates in the plane.

The continuity equation for our system, which describes the conservation of firebrand density, can thus be expressed:

$$\frac{\partial p}{\partial t} + \frac{\partial(w^1 p)}{\partial x^1} + \frac{\partial(w^2 p)}{\partial x^2} + \frac{\partial(vp)}{\partial z} + \frac{\partial(fp)}{\partial m} = 0. \tag{3.11}$$

Our full model then consists of the PDE (3.11), together with boundary conditions ((3.4), (3.5), (3.6)), as well as the initial condition (3.7).

3.3 Impulse-release, transport-type model for combusting firebrands

3.3.1 The characteristic equations and their solution operators

Let us recall our transport model derived in the first section of this chapter, for an impulse release of firebrands. We would like to determine the so-called *asymptotic landing distribution* $\mathbb{L}(x, m)$, which is the density of landed masses m at location $x = (x^1, x^2)$, which land due to the impulse release at time $t = 0$. The method of characteristics is typically used to produce solutions for conservation laws such as (3.11). We review this method and the kind of solutions it produces in Appendix A.

We recall that the transport-type model is given by Equation (3.11), which for the functional forms for w^1, w^2, v and f described in the preceding section, is *linear* with respect to the dependent variable p:

$$\frac{\partial p}{\partial t} + \frac{\partial(w^1 p)}{\partial x^1} + \frac{\partial(w^2 p)}{\partial x^2} + \frac{\partial(vp)}{\partial z} + \frac{\partial(fp)}{\partial m} = 0$$

where $x = (t, x, z, m) \subset [0, T] \times \mathbb{D}$, and $\mathbb{D}$ is the phase space for our model, determined in Equation (3.8).

Assuming that the functions w^1, w^2, v and f are smooth, we can rewrite Equation (**??**) in the form:

$$\frac{\partial p}{\partial t} + w^1 \frac{\partial p}{\partial x^1} + w^2 \frac{\partial p}{\partial x^2} + v \frac{\partial p}{\partial z} + f \frac{\partial p}{\partial m} + p \frac{\partial w^1}{\partial x^1} + p \frac{\partial w^2}{\partial x^2} + p \frac{\partial v}{\partial z} + p \frac{\partial f}{\partial m} = 0.$$

The first set of characteristic equations (see [33] or Appendix A), for a curve $(t(s), x^1(s), x^2(s), z(s), m(s))$ with parameter s, in vector form are given by:

$$\begin{aligned} (\frac{dt}{ds}, \frac{d(x^1)}{ds}, \frac{d(x^2)}{ds}, \frac{dz}{ds}, m') &= \left(\frac{\partial F}{\partial \frac{\partial p}{\partial t}}, \frac{\partial F}{\partial \frac{\partial p}{\partial x^1}}, \frac{\partial F}{\partial \frac{\partial p}{\partial x^2}}, \frac{\partial F}{\partial \frac{\partial p}{\partial z}}, \frac{\partial F}{\partial \frac{\partial p}{\partial m}} \right) \\ &= (1, w^1, w^2, v, f). \end{aligned} \tag{3.12}$$

By choosing $s = t$, solving the first equation, then we can parameterize our so-called spatial characteristic curves in terms of the time parameter. These curves solve the equations:

$$\begin{aligned} \frac{dx^1}{dt} &= w^1(z), \\ \frac{dx^2}{dt} &= w^2(z), \\ \frac{dz}{dt} &= v(t, m), \\ \frac{dm}{dt} &= f(t, z, m), \end{aligned} \tag{3.13}$$

where the arguments appearing on the right hand sides of the preceding equations incorporate all the functional forms which we will consider in this later in Chapter 4.

The above system of ordinary differential equations must be equipped with initial conditions

$$y(0) := (x^1(0), x^2(0), z(0), m(0)). \tag{3.14}$$

Although the equations (3.13) were derived under assumptions of smoothness, we can consider a generalized type of solution for which we will assume that the functions w^1, w^2, v, and f appearing in (3.13) are each *locally Lipschitz continuous*. With this assumption there exists a unique continuously differentiable solution of the equations (3.13).

It will be useful to introduce the notion of a *solution operator* $\Phi(t, y(0))$ corresponding to the Equations (3.13) with initial conditions given by $y(0)$ as in (3.14). The solution operator is defined in terms of the unique solution to the IVP for by:

$$(x^1(t), x^2(t), z(t), m(t)) =: \Phi(t, y(0)), \quad t \geq 0. \tag{3.15}$$

Corresponding to a given solution operator, there is a unique inverse operator which we denote by $\Phi(-t, y) = y(0)$.

Next consider the total derivative:

$$\frac{dp}{dt}(t, \Phi(t, y(0))) = \frac{\partial p}{\partial t}(t, \Phi(t, y(0))) + \frac{\partial \Phi}{\partial t}(t, y(0))) \cdot \nabla p(t, \Phi(t, y(0))). \tag{3.16}$$

Employing the property of the solution operator:

$$\frac{\partial \Phi}{\partial t}(t, y_0) = (w^1, w^2, v, f), \tag{3.17}$$

we can rewrite Equation (3.16) as:

$$\begin{aligned} \frac{dp}{dt}(t, \Phi(t, y(0))) = & \frac{\partial p}{\partial t}(t, \Phi(t, y(0))) \\ & + (w^1, w^2, v, f) \cdot \nabla p(t, \Phi(t, y(0))). \end{aligned} \tag{3.18}$$

Now, when one examines the differential equation in (3.12), and considering the expressions given in (3.17) and (3.18), we see that we can rewrite the transport equation (3.11) in the form:

$$\frac{dp}{dt}(t, \Phi(t, y(0))) = -p(t, \Phi(t, y(0)))\ \nabla \cdot (w^1, w^2, v, f). \tag{3.19}$$

In the next subsection we will investigate problems of existence and uniqueness for Equation (3.19).

3.3.2 Global existence and uniqueness of solutions in L^1 and L^∞

This subsection requires some notation and ideas, in particular the Banach spaces $L^1(\mathbb{D})$ and $L^\infty(\mathbb{D})$, both of which are discussed in Appendix B. In what follows $\mathbb{D}$ given in (3.8) defines the phase space for our problem. We will show that the regularity of the solutions to our impulse IBVP for the transport process (3.19) depends on the initial conditions.

One reason for looking at less smooth solutions will be evident after Chapter 5, where we will first discuss the spotting distribution $\mathbb{S}(x)$. We will there derive kernels $\mathbb{S}$ which are both exponentially bounded, and exponentially unbounded. In particular, while exponentially bounded kernels are both integrable and essentially bounded, exponentially *unbounded* kernels will not be integrable, but will be essentially bounded. Hence we are interested in solutions in $L^\infty(\mathbb{D})$ as well as integrable functions.

Let us assume $\nabla \cdot (w^1, w^2, v, f)$ is uniformly bounded in L^∞. Let us define A so as to denote the negative of the divergence map for fixed (w^1, w^2, v, f):

$$A(t) := -\nabla \cdot (w^1, w^2, v, f). \tag{3.20}$$

Then using this notation, we can rewrite Equation (3.19) as:

$$\frac{dp}{dt}(t, \Phi(t, y(0))) = A(t)\; p(t, \Phi(t, y(0))), \tag{3.21}$$

which is linear in p. Solving the latter, we obtain the solution along characteristics:

$$p(t, \Phi(t, y(0))) = \exp\big(\int_0^t A(s)ds\big)\; p(0, y(0)). \tag{3.22}$$

So we see that the initial conditions $p(0, y(0))$ play an important role in our formula for the solution (3.22). Having an explicit formula for the solution allows us to say much about the structure of solutions.

Theorem 3.1: *For the impulse IBVP consisting of the PDE (3.11), together with boundary conditions ((3.4), (3.5), (3.6)), as well as the initial condition (3.7), we have:*

1. *If the initial condition $p_0 \in L^\infty(\mathbb{D})$, then so is the solution p.*

2. *If the initial condition $p_0 \in L^1(\mathbb{D})$, then so is the solution p.*

Proof. 1. To deal with the first statement, we suppose initial condition $p_0 \in L^\infty(\mathbb{D})$. Then computing the norm of the solution, we find:

$$\begin{aligned} ||p(t)||_\infty &= ||\exp\,(\int_0^t A(s)ds)\; p(0, y(0))||_\infty \\ &\leq ||p_0||_\infty \exp\,(||A||_\infty \int_0^t ds) < \infty. \end{aligned} \tag{3.23}$$

This shows that the solution is bounded on any interval of the form $[0, T)$ for any $T > 0$, and hence we have global existence and uniqueness.

2. To prove the second statement, suppose the initial condition $p_0 \in L^1(\mathbb{D})$. Again computing the norm of the solution, we find:

$$\begin{aligned} ||p(t)||_{L^1} &= ||\exp\,(\int_0^t A(s)ds) p(0, y(0))||_{L^1} \\ &\leq \int_{\mathbb{D}} \exp\,(||A||_\infty \int_0^t ds) p(0, y)) dy \\ &\leq \exp\,(||A||_\infty t) \int_{\mathbb{D}} p(0, y)\; dy \\ &= \exp\,(||A||_\infty t);\; ||p_0||_{L^1} < \infty. \end{aligned} \tag{3.24}$$

Again we see our solution is bounded in $L^1(\mathbb{D})$ for all $t \in [0, T]$ for some $T > 0$.

□

Our family of solution operators are solutions to a possibly non-autonomous Cauchy problem, since the operator $A(t)$ may depend on t. We would like to characterize the solution family as an *evolution semigroup* [72].

Definition: A family $\{U(t, s)\}_{t \geq s}$ of bounded linear operators on a Banach space X is a strongly continuous evolution family if:

1. $U(t,s) = U(t,r)\, U(r,s), \qquad t \geq r \geq s.$

2. $U(s,s) = I$, where I is the identity on X.

3. The map $(t,s) \to U(t,s)$ is strongly continuous.

We can then define a strongly continuous *evolution semigroup* on $L^\infty(\mathbb{R})$, namely $\{T(t)\}$, according to the definition [72]:

$$(T(t)f)(s) := U(s, s-t)f(s-t), \tag{3.25}$$

for $f \in L^\infty(\mathbb{R})$.

Theorem 3.2: *Consider the IBVP outlined in Theorem 3.1. In the context of our problem, the strongly continuous evolution family is given by*

$$U(t,s) := \exp\,(\int_s^t A(v)dv), \tag{3.26}$$

where $U(t,s)$ acts as a multiplication operator. The semigroup $T(t)$ defined in (3.25) forms a strongly continuous evolution semigroup in $L^\infty(\mathbb{R})$,

Proof. We will establish that $U(t,s)$ defined in (3.26) forms a strongly continuous evolution family. Notice that:

$$\begin{aligned} U(t,s) &= \exp\,(\int_s^t A(v)dv) \\ &= \exp\,(\int_s^r A(v)dv + \int_r^t A(v)dv) \\ &= \exp\,(\int_s^r A(v)dv)\ \exp\,(\int_r^t A(v)dv) \\ &= U(t,r)\, U(r,s), \end{aligned} \tag{3.27}$$

which establishes the first property.

From the definition (3.26), it is clear that $U(s,s) = 1$, the identity on $L^\infty(\mathbb{R})$. Further, since $U(t,s)$ is an exponential function, and $A(t)$ is continuous (since it is a linear mapping which is assumed bounded), the map $(t,s) \to U(t,s)$ is strongly continuous. This completes the proof. $\square$

3.4 The landed branches L and the asymptotic landing distribution $\mathbb{L}$

In this section we will use an argument described in the thesis by Robbins [70], where he determined a similar asymptotic distribution in the context of seed dispersal. The transport process used in [70] is described either by an advection-reaction diffusion equation, or by stochastic differential equations.

Let us suppose that up to some time $T > 0$ we have a unique solution p, as would be guaranteed for example by the results in the preceding subsection. Since we are only interested in firebrands which land on the canopy (we do not consider within-canopy winds or resettling), we introduce the *landed branches* distribution $L(t, x^1, x^2, m)$ by

$$L(t, x^1, x^2, m) := \int_0^t p(s, x^1, x^2, H, m)ds. \tag{3.28}$$

The landed branches distribution can be integrated, against m, to determine the total mass which lands at location (x^1, x^2) by time t.

Remark: In the limit where the launching heights are very large, and we are interested mostly in the 'tail' of the landed branches distribution, then at least for our constant-velocity models, we can approximate $H \approx 0$. We are interested in this case in firebrands which travel a long distance, and relatively uninterested in local dispersal, so relative to the scale of such dispersal a typical canopy height H is very small.

Thus L is the density of firebrands of mass m which have landed at (x^1, x^2) on the canopy by time t. Also of interest is the *asymptotic landing distribution* $\mathbb{L}(x, m)$, defined by

$$\mathbb{L}(x, m) := \lim_{t\to\infty} L(t, x, m). \tag{3.29}$$

The asymptotic landing distribution describes the density of firebrands with mass m which will eventually land at location $x = (x^1, x^2)$. We will revisit this concept later, when we discuss continuous models for the spotting distribution $\mathbb{S}(x)$ in Chapter 5.

3.4.1 The one-dimensional case

To make our models more analytically approachable, in this section we return to the case of a line fire, which propagates as a line in the direction of increase in the single spatial variable x, as outlined in the introduction to the first chapter. That is, in the horizontal direction we are only concerned with movement in the $x^1 := x$ direction, where the x^2-direction is assumed parallel to the fire front.

The transport model in this case reads:

$$\frac{\partial p}{\partial t} + \frac{\partial (wp)}{\partial x} + \frac{\partial (vp)}{\partial z} + \frac{\partial (fp)}{\partial m} = 0. \tag{3.30}$$

The characteristic equations for this first-order PDE are the same as those described in (3.13), except that the first spatial equations degenerate to a single equation for the coordinate x:

$$\begin{aligned} \frac{dx}{dt} &= w(z), \\ \frac{dz}{dt} &= v(t, m), \\ \frac{dm}{dt} &= f(t, z, m). \end{aligned} \tag{3.31}$$

The initial conditions for the characteristic equations are chosen in terms of the *launching distribution* $\phi(z, m)$, at location $x = 0$.

If we assume a homogeneous medium, then we have a single launching distribution $\phi(z, m)$, assumed to be launched at time $t = 0$ at location $x = 0$. The boundary conditions then reduce to:

$$p(t, 0, z, m) = \delta(t)\phi(z, m), \tag{3.32}$$

where again $\delta(t)$ denotes the Dirac delta functional.

Hence we are supposing that no further firebrands are released from the main fire for any time $t > 0$. We will also assume again that initially there are

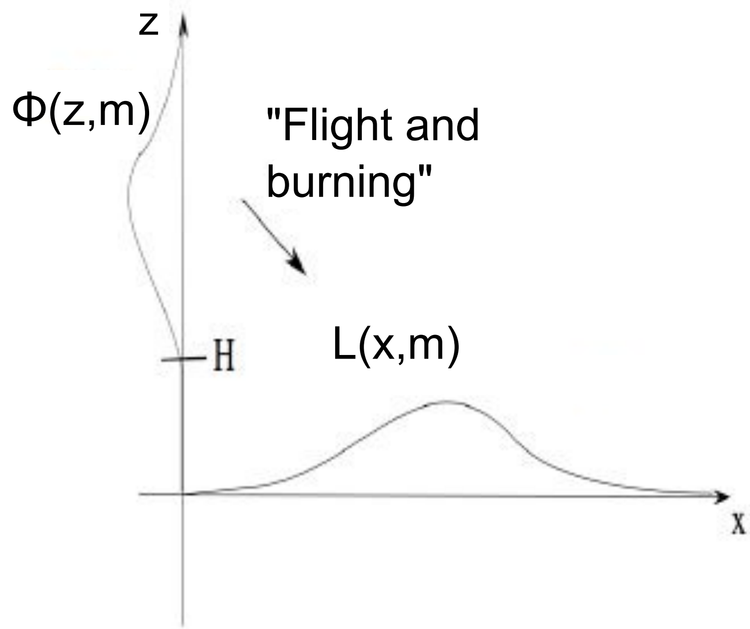

Figure 3.2: Determining the "flight and burning" distribution $\mathbb{L}$ from the vertical launch distribution ϕ. The "flight and burning" refers to the physical details of firebrand flight and combustion, which we will discuss in the next chapter. Shown in the vertical is a cross-section of the launching distribution $\phi(z, m)$, which is then tracked via the density $p(t, x, z, m)$. By examining the landed branches $L(t, x, m)$, which is the density of branches on the ground, we determine in the limit as $t \to \infty$ the asymptotic landing distribution $\mathbb{L}(x, m)$ as in (3.29). A possible asymptotic landing distribution is plotted here in the horizontal.

no firebrands in flight ahead of the front, so that

$$p(0, x, z, m) = 0, \qquad x > 0. \tag{3.33}$$

It will be our goal to determine what forms are possible for the asymptotic landing distribution $\mathbb{L}(x, m) = \int_0^t p(s, x, H, m)\ ds$, where H is the canopy height. This was defined at the end of the previous section, and the formulas (3.28) and (3.29) apply in this context, except now we have $x \in [0, \infty)$. The distribution $\mathbb{L}(x, m)$ is dependent on the launching distribution $\phi(z, m)$, as illustrated in Figure 3.2.

3.5 Chapter summary

In this Chapter, we introduced a model for firebrand transport and combustion, and described qualitative properties of its solutions. We showed how it can be used to obtain the asymptotic landing distribution $\mathbb{L}(x, m)$, which describes how an impulse release of firebrands leads to a landing distribution at point $x \in [0, \infty)$ and $m \in [0, \bar{m}]$.

In the following chapters, we will largely focus on the one-dimensional case, in the interest of mathematical analysis. In Chapter 4 we will examine a variety of physical models for firebrand generation, launching, transport, and combustion. The latter in turn will provide functional forms for the right hand sides (w, v, f) appearing in the characteristic equations, the launching distribution $\phi(z, m)$.

In addition, we will describe the *ignition operator* $E(m)$, which gives the probability that a mass m will ignite a fuel bed in a homogeneous medium.

After explaining our physical models for firebrand ignition and transport, we will revisit the asymptotic landing distribution in Chapter 5, and obtain from it the *spotting distribution kernel* $\mathbb{S}(x) \in [0, 1]$, which gives the probability of a spotfire occurring at location x, due to an impulse release as described in this section. The spotting distribution discussed in Chapter 5, and will provide a candidate for the spotting kernel appearing in our models in Chapter 2.

From this we generalize the i-PDE models considered in the second chapter. The reader will recall that there we assumed a constant windspeed w and falling speed v, and this resulted in a constant *landing time* $t^*(x) = x/w$, the latter being the travel time from launch to landing. We will obtain, in Chapter 5, a host of possible spotting kernels, by generalizing the falling time to include more physical wind profiles. These will include exponentially bounded, and exponentially unbounded kernels, and we will see very different behavior for the i-PDE models depending on whether the kernel is bounded or not.

Chapter 4

Models for firebrand generation, combustion, transport and fuel bed ignition, new and old

4.1 Chapter Introduction

In this chapter we will discuss the modelling of physical subprocesses that are involved in the spotting problem. We will review the extensive literature in this area, and derive mathematical models for the firebrand mass distribution, plume models and the vertical launch distribution, firebrand combustion and temperature, vertical and horizontal transport speeds, and ignition probabilities.

By considering all the possible permutations of the models considered here, when we derive the spotting distribution in Chapter 5, we obtain an enormous number of possible spotting distributions. Our goal is not consider to determine the corresponding spotting distributions for all such permutations, but rather to synthesize the existing physical and empirical submodels into the spotting distribution in the next chapter.

This chapter need not be read straight through; the Table 4.8 in the final section of this chapter summarizes the models, and a given model can be referred back to as needed. The reader interested in determining the spotting distribution, as in Chapter 5, should read, at least, the subsection concerning the combustion operator $\mathcal{C}$, and Section 4.7 in which we introduce the ignition operator $E[m]$. Also of great importance is Subsection 4.5.2, where we describe the *type* of spotting considered in this thesis.

4.2 Firebrand distribution generated from burning vegetation

4.2.1 Experimental results and challenges

Firebrand generation refers to the release of burning plant material, i.e. firebrands, from a wildfire. Unfortunately, there are only a few quantitative experimental studies which measure the important characteristics of such firebrands in relation to their ignition efficiency, in terms of type, mass, length, and effective diameter.

Prior to the beginning of this thesis, there were no studies on this subject. A series of studies by Manzello and colleagues ([53], [54], [55]) were a first step in the right direction. These experimental studies investigated firebrands emitted from the controlled burning of either pine or fir trees. The experimenters responsible for the Manzello studies are continuing their research at the Building Research Institute in Japan [55], and with time hopefully a more complete description of the firebrand distribution will emerge.

A prior investigation of Babrauskas [13] determined that Douglas fir trees with moisture content greater than seventy percent will not sustain burning after ignition; between thirty and seventy percent moisture results in partial combustion, and below thirty percent moisture content complete combustion occurs. The authors in [54] confirmed that Douglas fir do not emit firebrands if the moisture content exceeds thirty percent and no external moisture is applied. Complete combustion typically occurs within twenty seconds after ignition in extreme burning conditions.

In the Manzello experiments, trees both 2.6 metre and 5.2 metres tall were investigated. For each tree, more than 70 firebrands were collected. These were all cylindrical in shape. The average firebrand length and diameter for the 2.6 metre class was 40 mm in length and 3 mm in diameter, while for the 5.2 metre class the average was 53 mm in length and 4 mm in diameter. The most recent of the experiments, on Korean pine [54], confirmed that the distribution was approximately the same. The total number of firebrands collected numbered almost 1000.

With respect to mass, all three studies indicate that between 60 and 80 percent of the firebrands have masses less than 0.1 grams. Further, for both pine and fir taller trees produce larger firebrands, with the largest found at about 5 grams. In addition, between 58 and 65 percent of the firebrand mass is needles, which are insignificant in long-range spotting, but may be effective at igniting local fuel in short-range spotting [38]. When one removes the needles from the mass distribution, one ends up with a very different-looking distribution, which we call the 'effective mass' distribution.

Of course, we must be open to considering a variety of possible firebrand mass distributions, since the data only covers a small subset of the possible distributions. For example, with stronger winds or larger trees, we would expect to see a greater proportion of large firebrands, as suggested by the Manzello studies [54]. We have also not considered other types of firebrands such as pine cones or Eucalyptus bark, which can be very dangerous as a spotfire risk [37].

Fortunately, the framework developed in this subsection and the next will allow us to formulate very general models, so that when more detailed experimental information is available, we can incorporate this information to make our models more realistic. In the next two subsections, we present experimentally-derived models for the mass probability distribution $\mu(m)$, which we assume varies continuously on $[0, \overline{m}]$, where $\overline{m}$ is the maximum loftable firebrand *mass*.

4.2.2 Model G1: Regression analysis on Manzello's data

In order to determine a functional form for the effective mass distribution, we reproduced the histograms from ([54], [55]), an example of which is shown in Figure 4.1.

In general between 60 to 70 percent of the mass is needles as discussed in section 4.2.1, which are negligible for long-range spotting. We decided to use linear regression to try to find a *mass distribution* $\mu(m)$, $0 \leq m \leq \bar{m}$. Before

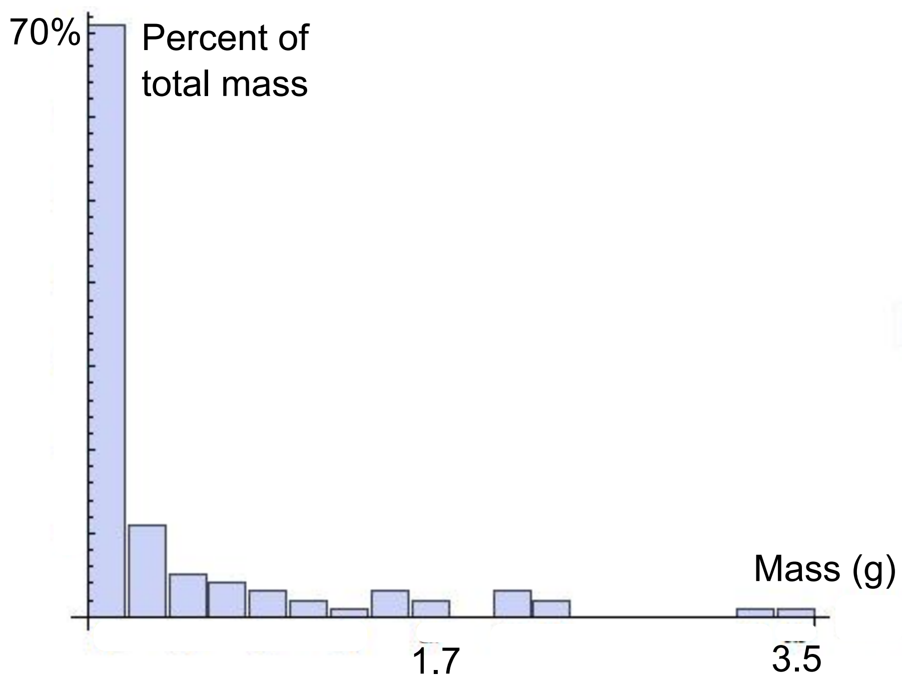

Figure 4.1: The mass distribution for the 5.2m Douglas fir firebrands, reproduced from the histogram in [47]]. The histograms for the other taller specimens for each species studied are similar. Along the x-axis we plot firebrand mass in grams. It should be noted that most of the masses which are less than or equal to 0.1 grams are needles, which make up about 70 percent of the total distribution, and which are insignificant for long-range spotting.

doing this, we first removed the needles lying in the 0.1 gram mass class, to obtain an effective firebrand distribution. To do this, we used Mathematica's FindFit command, which performs least-squares regression analysis on data points chosen from the histograms, employing the functional form:

$$\mu(m) = am^{-b}, \qquad 0 \leq m \leq \bar{m}. \tag{4.1}$$

We set $\bar{m} = 4$, corresponding to the maximum firebrand mass of about 4 grams. Then we found $b = 1/2$, and chose $a = 1/4$ for normalization. We found this was a better fit than an exponential form.

4.2.3 Model G2: Models obtained from burning slash

Another firebrand distribution was suggested in [90], which relates the possible radius r of a firebrand to the mass consumption rate m_f, in the form:

$$p(r) = \frac{\alpha m_f}{r\sigma\sqrt{2\pi}} \exp\left(\frac{-1}{2\sigma^2} \log\left(r/r_0\right)^2\right), \tag{4.2}$$

where r_0 and σ were parameters determined by regression analysis, and α represents the the number of firebrands generated per unit mass.

If we assume a relationship of the form $m = m(r) = \rho V(r)$, where ρ is the density and $V(r)$ is the firebrand volume, then from (4.2) we find the mass density:

$$\mu(m) = \int_0^\infty \delta(m - m(r))p(r)dr, \tag{4.3}$$

where δ denotes the Dirac delta distribution.

Remark: From the experiments of Manzello described in this chapter, it was found that approximately one percent of the total mass lost during combustion appeared as firebrands. This could inform our parameter α, and in turn determine the total mass and total number of firebrands released when a given number of trees begin to spot.

4.3 Firebrand combustion

4.3.1 The combustion operator C and its inverse

Several combustion models have been proposed in the literature, and the interested reader is invited to peruse the review in [93]. They are usually modeled as continuous-time processes, so we will present functional forms for the density, effective radius, or simply the mass as functions of time.

Suppose the mass $m(t; m_0)$ is the unique solution of the initial value problem

$$\frac{dm}{dt} = f, \qquad m(0) = m_0. \tag{4.4}$$

Physically this means given a mass m_0 which is combusting, $m(t; m_0)$ is the mass of the same object observed t units later, and f is the rate of combustion.

We introduce the operator C, defined

$$C(m_0, t) := m(t; m_0). \tag{4.5}$$

We call C the *combustion operator*, and the right hand side f in the differential equation for $m(t)$ is to be specified. The assumption of a unique solution for the initial value problem places constraints on the function f.

Similarly we can define the inverse mass-solution operator $C^{-1}(m, t)$, which is the unique solution to the initial value problem $\frac{dm}{dt} = -f, m(0) = m$ at time $t \geq 0$.

Remark: Before continuing, it is important to note that the combustion process does not continue past the point where the firebrands have masses less than or equal to zero. Hence the combustion operator is only defined up to the burnout time t_b, and similarly for its inverse.

To illustrate with a simple example, suppose the burning rate is a constant $f < 0$, then we have $m(t) = m(0) + ft < m(0)$, and $C(m_0, t) = m_0 + ft$. Then $C^{-1}(C(m_0, t), t) = m_0$.

Remark: The combustion operator C corresponding to Equation (4.5) is the continuous-time, continuous-space analogue of the discrete combustion operator introduced in Chapter 2, described in the paragraph leading to the definition (2.14).

4.3.2 Model C0: Constant burning rate

While not as physically realistic, in several points of this discourse we discuss models where the burning rate, say $f > 0$, is constant. Given an initial mass m_0, our first and simplest model for $m(t)$ is:

$$m(t) = m_0 - ft, \tag{4.6}$$

so long as $m(t) > 0$.

4.3.3 Model C1: Tarifa's original experiments and models

The first experiments on the density and shape changes in combusting firebrands was carried out by Tarifa and collaborators at the Aerospace Corporation [2]. This data was fit by regression analysis obtained from windtunnel experiments, where both spherical and cylindrical firebrands were examined under a variety of ambient windspeeds.

Suppose $\rho(t)$ represents the density of a firebrand at time t, and $\rho(0)$ is the initial density. Then Tarifa found the density varied:

$$\rho(t) = \frac{\rho(0)}{1 + \eta t^2}, \tag{4.7}$$

where the constant $\eta = 2.86 \times 10^{-4}$ is determined from regression analysis.

4.3.4 Models C2, C3: Caricatures of Tarifa's model

C2 A common observation is that initially firebrands lose mass slowly, but gradually this mass loss increases over time. If we assume that the firebrand transport process is very rapid compared to the firebrand combustion timescale, we could assume that the change in shape is negligible. We then could employ an analogue of Tarifa's density evolution for the mass $m(t)$, namely

$$m(t) = \frac{m(0)}{1 + \eta t^2}. \tag{4.8}$$

C3 If we take case C2 to its extreme, sending $\eta \to 0$, then the transport process is seen instantaneous compared to the combustion process, so we assume

$$m(t) = m(0). \tag{4.9}$$

4.3.5 Model C4: Tse and Fernandez-Pello's improvements

Tse and Fernandez-Pello revisited Tarifa's data set [85], and determined the model which best fit the data for the effective radius evolution is:

$$r(t)^4 = r(0)^4 - \frac{\chi\beta^2 t^2}{16}. \tag{4.10}$$

Clearly the latter is only defined while $r(t) > 0$, which implies a finite burnout time. Here the parameter χ depends on the wood species and moisture content of the firebrand, and β is described below in the derivation of Equation (4.15). Based on Tarifa's data, the parameter $\chi = 3.5$ gave the best fit [88].

To determine the mass $m(t)$, we first employ the simple relation:

$$m(t) = \rho(t)\mathrm{Vol}(r(t)), \tag{4.11}$$

where $\mathrm{Vol}(r(t))$ is the volume of the firebrand, and hence dependent on the radius $r(t)$.

As a simple example, suppose the firebrand is approximately spherical, so that $\mathrm{Vol}(r(t)) = \frac{4}{3}\pi r(t)^3$. Then we combine Equations (4.8) and (4.10), so that the mass evolution (4.11) is given by

$$\begin{aligned} m(t) &= \rho(t)\frac{4}{3}\pi r(t)^3 \\ &= \frac{4}{3}\frac{\rho(0)}{1+\eta t^2}\left(r(0)^4 - \frac{\chi\beta^2}{16}t^2\right)^{3/4} \end{aligned} \tag{4.12}$$

Taking for example cedar wood as representative of forest fuel, as did the authors in [16], the initial density $\rho(0)$ of the firebrands would be 513 kg/m^3, while in the experiments of Manzello [54] he found radii ranging from one half to five centimetres.

Remark: Another important result following the analysis in [88], is that one can reasonably approximate extinction of the firebrand to occur once:

$$\frac{m(t)}{m_0} = m_c, \tag{4.13}$$

where m_c is a critical mass ratio which depends on the wood species.

Beyond this point all that remains is non-flaming char, whose temperature then decreases according to Equation (4.23) described in the next subsection. From regression analysis in [88], we find $m_c = 0.24$ for maple and pine.

4.3.6 Model C5: Including more physical realism

Another model has been derived in [16], and is based in part on experimental fitting of data by Tse and Fernandez-Pello [88]. It is based on Nusselt's physically-motivated combustion theory, known as 'shrinking drop theory' ([16],[42]).

We include a discussion of the model here because, as we will see later, the firebrand's burning temperature may influence its flight path significantly [16].

In Nusselt's combustion theory, the firebrand's surface is assumed to be held at constant temperature, maintaining its geometrical shape while a pyrolysis wave propagates inward. One employs the so-called Frossling relation, in which we define the *effective mass diameter* d_{eff}, and an experimental constant β, such that:

$$\frac{d}{dt}\left(d_{\text{eff}}\right)^2 = -\beta. \tag{4.14}$$

The constant β, introduced earlier in Equations (4.10) and (4.12), is determined physically from the equation:

$$\beta = \beta^0\left(1 + 0.276 R_e^{1/2} S_c^{1/3}\right), \tag{4.15}$$

where on the right hand side we have the Reynolds number R_e, and the Schmidt number S_c, and an experimentally determined constant β^0.

The Reynolds number $R_e = \frac{2|v|r}{\nu_{\text{air}}}$, where $|v|$ is the firebrand's speed relative to the surrounding air, r is the firebrand radius, and ν_{air} is the kinematic viscosity of the surrounding air[16]. R_e is a dimensionless constant which measures the ratio of the effects of inertia to viscosity for the firebrand.

The Schmidt number S_c is a dimensionless constant which gives the ratio for viscosity to mass density, for mass-transfer problems. For air S_c is approximately constant, i.e. $S_c \approx 0.7$ for a wide range of temperatures.

Based on the data from [88], which was computed experimentally for firebrands with temperatures at about 993 K, we find the constant β^0 which appears in Equation (4.15) to be $\beta^0 = 4.8 \times 10^{-7}$ m^2/s.

Employing Tarifa's model for the density evolution ρ (4.7), and the solution to the differential equation for d_{eff}, the firebrand mass m is then approximated by:

$$m = \rho \pi d_{\text{eff}}^3 / 6. \tag{4.16}$$

4.3.7 Model C6: Albini's combustion model within line thermals

A final model was derived by Albini [3] in the context of firebrand transport by line thermals. Line thermals are well-mixed horizontal columns of warm air which rise above large forest fires, and are subsequently transported in a coherent manner downwind. Albini modeled line thermals as well-mixed cylinders of air rising above a fire.

If we assume that a firebrand has mass density $\rho(t)$, and terminal velocity v relative to the line thermal, Albini's model reads:

$$\frac{d}{dt}\rho(t) = -k\rho(t)v, \tag{4.17}$$

where the constant $k = 8.15 \times 10^{-}3$ was chosen to match wind-tunnel data [3].

4.3.8 A model for firebrand temperature

A model for firebrand temperature based on energy conservation is given in [16]. Let us define the density ρ, volume V, specific heat capacity at constant pressure c_p, and surface area A for a given firebrand.

Then the temperature $T(t)$ appears in the energy conservation equation,

$$(\rho V c)\,\frac{DT}{Dt} = -A(q_{\text{conv}} + q_{\text{rad}}) \tag{4.18}$$

where the terms q_{conv} and q_{rad}, appearing on the right hand side in the latter equation, represent the heat loss due to convection and radiation; the notation $\frac{DT}{Dt}$ represents the material derivative of T along the firebrand's trajectory.

The convective heat flux can be modelled by Newton's law of cooling [16],

$$q_{\text{conv}} = h(T - T_a), \tag{4.19}$$

where h is an average heat-transfer coefficient, and T_a is the ambient temperature.

To determine the heat-transfer coefficient, we first introduce the average *Nusselt number* Nu,

$$Nu = 2 + 0.6Re^{1/2}Pr^{1/3}, \tag{4.20}$$

where Pr the *Prandtl number* for air, and Re is the Reynolds number as described following Equation (4.15) [16].

The Prandtl number is a dimensionless constant which measures the ratio of viscosity to thermal diffusivity. For example, when $P_r << 1$, heat diffuses quickly compared to momentum. For air, we have $Pr \approx 0.70$ [16].

Then the average heat transfer coefficient is given by:

$$h = \frac{k_{\text{air}} Nu}{2r}, \tag{4.21}$$

where $k_{\text{air}} \approx 2.7 \times 10^{-2}$ m^2/s is the thermal conductivity of air, and r is the firebrand's radius.

The radiative heat flux can be approximated by the Stefan-Boltzmann law, which states:

$$q_{\text{rad}} = \sigma\epsilon(T^4 - T_a^4), \tag{4.22}$$

where σ is the Stefan-Boltzmann constant, and ϵ is the emissivity. From experiment, $\epsilon = 0.9$.

It follows that the energy balance equation for the temperature evolution can be written:

$$\frac{dT}{dt} = -\frac{6}{\rho V c 2\, r(t)} \left[h(T - T_a) + \sigma\epsilon(T^4 - T_a^4) \right]. \tag{4.23}$$

This can be solved assuming the firebrand is initially at flaming temperature, e.g. $T(0) = 993$ K, to determine the temperature evolution once flaming combustion has halted when $m = m_c$.

4.4 Terminal velocity

4.4.1 Drag, gravity and terminal velocity

Firebrands which are being lifted in the fire's convection column are doing so, because the plume's upward drag force exceeds the firebrand's weight. Since the plume's drag decreases with height, the drag is eventually balanced by the firebrand's weight, at which point the firebrand discontinues accelerating in the vertical direction. We say that the firebrand has reached its *terminal velocity* relative to this particular flow.

Similarly, firebrands traveling in the atmosphere experience drag. In order to accurately model the transport of firebrands in the atmosphere, it is important to model the drag experienced by the firebrand.

It is common to assume that either the drag is proportional to the object's speed, or speed squared, depending on the Reynolds number for the flow. For firebrands, it is more accurate to model drag as proportional to the speed squared, since we have a relatively high Reynolds number flow [16].

Let's denote the drag force by D. Then the speed-squared assumption is generally written:

$$D = \frac{1}{2} C_d \rho_a A v^2, \tag{4.24}$$

where ρ_a refers to the mass density of the ambient fluid, and the object is assumed to have constant cross-sectional area A.

The parameter C_d appearing in Equation (4.24) is called the drag coefficient. This is a dimensionless number, with values typically ranging between 0.001 and 2, assumed to vary with shape. This constant is typically determined by experiment.

Mathematically, Newton's Second Law then provides us with an expression for terminal velocity. If we focus on the vertical direction, the balancing of the drag force D with the weight W implies:

$$\begin{aligned} 0 &= \text{Drag} - \text{Weight} \\ &= \frac{1}{2} C_d \rho_a A v^2 - mg. \end{aligned} \tag{4.25}$$

Solving for v in Equation (4.25), we obtain an expression for the terminal velocity:

$$v = \sqrt{\frac{2mg}{C_D \rho_a A}}. \tag{4.26}$$

4.4.2 Model V1: Constant terminal velocity

The general expression for a firebrand's terminal velocity v as given in Equation (4.26) depends on the experimental determination of appropriate parameters. The first effort in this direction was conducted by the Aerospace Corporation in the 1960's [75], which consisted of windtunnel experiments on spherical and cylindrical firebrands.

These experiments found that the firebrands quickly attained their terminal velocity and configuration, for a variety of windtunnel windspeeds. Similar windtunnel experiments performed recently by Ellis [31], on Eucalyptus bark from Australia, found similar results.

While moving through the atmosphere, where the windspeeds tend to increase as a function of height, it is natural to assume that firebrands quickly attain terminal vertical velocity v. The simplest assumption (V1) is to assume the terminal velocity does not change during transport.

4.4.3 Model V2: Experimentally determined model

Experimental analysis on the Aerospace Corporation's experiments, appearing in [63], revealed that for the cylindrical firebrands in the study the mass $m(t)$ is related to the terminal velocity $v(t)$ according to:

$$v(t) = v(0) \left(\frac{m(t)}{m(0)} \right)^{1/2}. \tag{4.27}$$

Since $m(t)$ is decreasing due to combustion, this means that the terminal velocity is also decreasing with time.

4.5 Firebrand lifting in the fire's convection column

4.5.1 Definition and characteristics of wildfire plumes

As stated earlier in this chapter, the greatest challenge in modelling spotting is to determine how many firebrands, distributed according to their various characteristics, are both generated and subsequently launched into the atmosphere. The latter process takes place in the high-velocity, buoyancy-driven flow induced by the combustion at the surface.

A fire plume is a vertically rising column of gas resulting from heating from below by the fire's flame [68]. The plume of a wildland fire is often called its *convection column* [90]. A fire plume is principally buoyancy driven, meaning the upward flow in the plume results from an increase in temperature (or consequent decrease in fluid density) [68].

Any fire plume is more likely to be turbulent than laminar, and most of our knowledge about plumes is experimental, rather than purely theoretical [68]. In addition, in the case of a wildland fire, there is a complicated interaction between the atmosphere and the fire, hereafter referred to as *fire-atmosphere interactions*. This results in a distortion of the plume relative to constant-wind conditions. The fire-atmosphere interaction has been extensively studied from experiments, and from physics and numerical experiments ([1],[2],[16],[23],[24],[22],[27],[28],[59],[64],[66],[76],[83],[84]).

Experimental measurements of Rouse [72] determined that the normalized vertical plume velocity U_p, and temperature T of a turbulent plume, generated by a small source, have Gaussian profiles in horizontal cross-sections across the plume.

These Gaussian profiles are approximate solutions to the full Navier-Stokes equations with combustion and buoyancy, which govern the fire plume's behaviour [68]. A completely accurate physical model is complicated by the fact that there are multiple of scales of turbulence acting on the fire plume. At fine scales, high-frequency turbulence is responsible for fuel-oxygen mixing and local combustion, while at large scales one observes the global 'engulfment' of ambient air by the large eddy structures which curl around outside the plume [68].

There has been recent work which suggests that the fire-atmosphere interaction results in distinctly non-Gaussian distributions [16]. In the physically realistic computer simulations of grass fire plumes of [16], which employs a Large Eddy Simulator to model the atmospheric winds, the time-averaged velocity profiles are not observed to be Gaussian. Further, the authors of this paper call into question the validity of the so-called Baum and McCaffery forest fire plume, which has been used widely in literature and in practice. Their research suggests that the latter model, discussed in detail in the next section, may only be appropriate for modelling the convection column above a stationary fire [16].

As a final encouraging note, one can think of several important fire situations where stationary fires could produce spotting, such as when a fire is approaching the wildland-urban interface [90], or an extended obstacle as in the problem of spotfire breaching. This situation will be briefly discussed in Chapter 5.

4.5.2 The types of spotting considered in this thesis

Depending on the convection column, there are seven types of spotting [73]. We want to be clear about the types of spotting which our impulse-release model can describe.

A type 1 fire consists of a very powerful convection column, with light surface winds, which rises vertically into the atmosphere. A type 2 fire is similar, but the distinction is the presence of strong surface winds, which can lead to spotting [73]. Since we model a vertical release, these fire types are one of the main focuses of this thesis.

Spotting types 3 and 7 consist of spotting over mountainous topography, so our models as they stand would be inadequate to model this type of situation.

Another extreme spotting situation [73] is a type 4 fire, where strong winds aloft cause the shearing off of the top of the convection column. The result is a nearly horizontal column aloft, which rains firebrands down well ahead of the main fire. Clearly our boundary conditions as they stand cannot account for this type of release. In future work, by considering the sheared-off portion of the column as a line thermal, as in the work by Albini [3], we could perhaps obtain initial conditions based on release from such a thermal.

We could consider our model from Chapter 3 as an approximation to spotting type 5, where the convection column leans towards the strong winds but does not break off, and short and long range spotting is possible [73]. The more intense the fire, the straighter the convection column, and the more intense the wind, the more horizontal the convection column. In future work we could consider initial conditions along a slanted line, which would approximate this spotting type much better.

The spotting type 6 situation occurs where there are very strong winds above the ground, so that no convection column forms [73]. In this case, spotting could play an important role [73]. For example, in coniferous forests, chapparal brush, slash, Eucalyptus-grassland forests, or even conflagration fires in cities, enormous amounts of firebrands are generated. In all cases, the firebrands are literally swept along by the wind. Our L3-model, where heights and masses are independent of each other, and the constant wind assumption, here are physically realisitic.

Since the flame height will be of the order of firebrand heights, an adequate flame model should be provided (and do exist [40]). In a crown fire in a coniferous forest, where the average combustion lifetime of needles emitted is less than ten seconds [37], the massive amount of needles emitted could have an effect on the rate of spread. It is likely that this is accounted for in the Fire Behaviour Prediction system [40], though their models are entirely statistical in origin. Perhaps a mechanistic model including this type of spotting, and other effects like radiation and convection could be developed, and compared to the data sets that the Fire Behaviour Prediction system are based on. This is an opportunity for future work, and is relevant since current crown fire models seem inadequate [5] to account for all situations.

4.5.3 The Baum and McCaffery plume

As stated at the end of the previous subsection, the most widely used fire plume model in spotfire modelling is the model developed by Baum and McCaffery ([15],[24]), as used for example in ([2],[3],[16],[34],[66],[89],[93]). The model

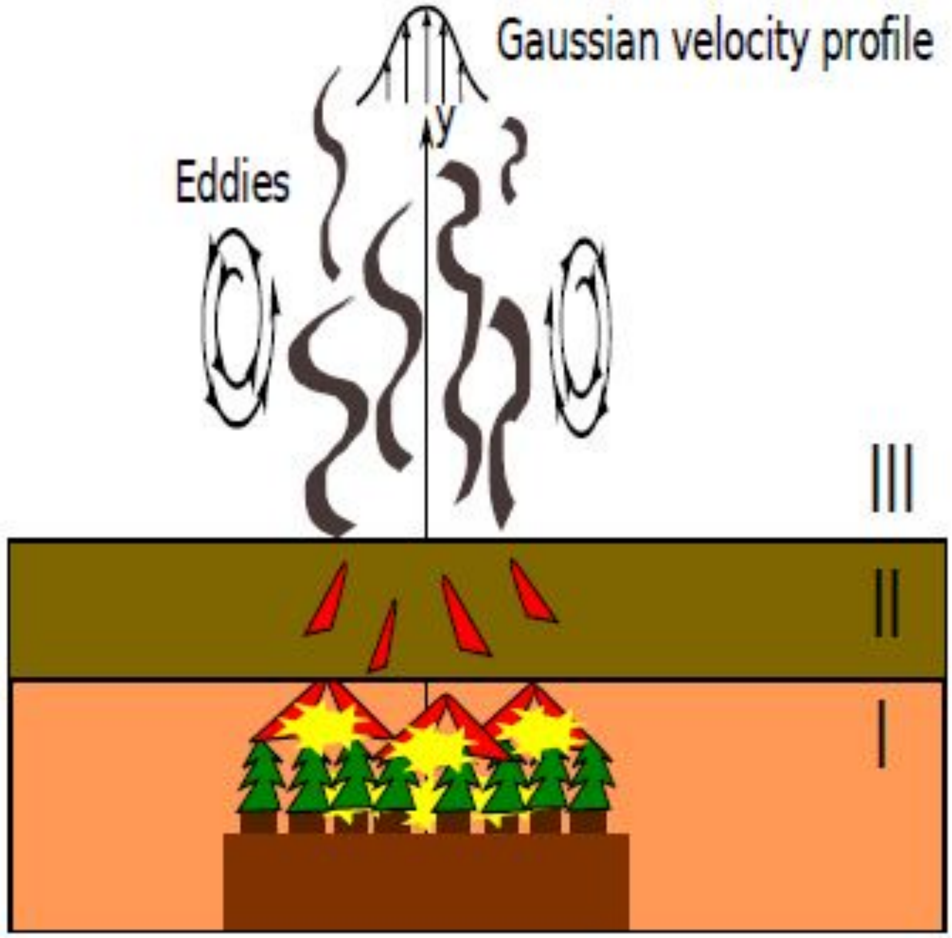

Figure 4.2: Sketch of a cross-section along the burning front. Presented are the three regions of the Baum and McCaffery plume. Region I is the continuous (canopy) burning region. Region II is a transition zone over which the plume velocity is constant; the continuous flames flicker up and break off from Region I. The plume is represented in Region III. The buoyant upward motion of the plume is reinforced by large ambient eddies, which cause entrainment of air into the plume. Both centerline velocity and temperature are assumed to fall off according to a Gaussian profile, for the Baum and McCaffery plume (this assumption may not be valid for real convection columns [16]).

consists of three burning regions, illustrated in Figure 4.2. The discussion here closely follows that of the book [68], and the paper [16].

Region I lies at the base, and is the continuous burning region. Here the flow is pulsating and unsteady. Region II is an intermittent zone, in which flame patches break off from the below-anchored flame, while at the top of Region II all combustion ceases. Finally we have region III, the non-combusting plume, where we assume that the time-averaged upward velocity and temperature drop off radially in a Gaussian manner.

The relevant parameters are height z, plume velocity U_p, and temperature T. These are made dimensionless by the scaling:

$$\frac{z}{z_c} := z^*, \quad \frac{U_p}{U_c} := U^*, \quad \frac{T - T_a}{T_a} := T^*, \tag{4.28}$$

where:

$$z_c := \left(\frac{Q}{\rho_a c_p T_0 \sqrt{g}} \right)^{2/5}, \quad U_c := \sqrt{g z_c}. \tag{4.29}$$

The parameters appearing in (4.29) are the heat release rate Q, the density of air $\rho_a = 1.2$ kg m^{-3}, $c_p = 1$ kg^{-1} K $^{-1}$ is the specific heat capacity of air at constant pressure, T_a is the temperature of the ambient air, and g is the gravitational constant.

The analysis in [57] then leads us to the following relationships in Region III of the plume, providing us the mean plume-centerline velocity and temperature as a function of the rescaled height z^*:

$$U^* = 3.64(z^*)^{-1/3}. \tag{4.30}$$

$$T^* = 8.41(z^*)^{-4/3}. \tag{4.31}$$

Recall from our discussion of terminal velocity, that for a given height z in the plume region there is associated a unique mass $m(z)$, such that this mass attains terminal velocity exactly at height z. In other words, the drag induced by the upward plume velocity U_p is balanced by the weight of the mass at this height.

In the idealized case of a spherical particle, we have a direct connection between the cross-sectional area A, the diameter d, the drag coefficient C_D and the density ρ_s. Employing the relation (4.30), we obtain the unique lofting height:

$$z = \left(\frac{40 C_D \rho_a}{4 d \rho_s g} \right)^{3/2} z_c, \tag{4.32}$$

Employing (4.29) in the latter equation, we can re-write the lofting height as:

$$z = \left(\frac{40 C_D \rho_a}{4 d \rho_s g} \right)^{3/2} \left(\frac{Q}{\rho_a c_p T_0 \sqrt{g}} \right)^{2/5}. \tag{4.33}$$

For simplicity of notation in what follows, we will introduce a constant γ which absorbs all the constants in (4.33), and re-write the Equation:

$$z(m, Q) = \gamma m^{-3/2} Q^{2/5}, \tag{4.34}$$

where the constant γ is defined by

$$\gamma := \left(\frac{40 C_D \rho_a}{4 d \rho_s g \left(\rho_a c_p T_0 \sqrt{g} \right)^{4/15}} \right)^{3/2} \tag{4.35}$$

It should be noted that there is also a maximum loftable diameter d_{max}, which is defined as the maximum diameter above which no firebrands make it beyond Region II [16]. Again solving for the height of force balance, one obtains:

$$d_{max} = \frac{3 m C_D}{4 V \rho_a g} \left(2.45 U_c \right)^2, \tag{4.36}$$

where V is the volume occupied by the firebrand with mass m.

4.5.4 Mathematical models for the launching distribition $\phi(z, m)$

In Chapter 2, we made the assumption that at any point where spotting is occurring, the same vertical launch distribution ϕ is launched into the convection column. We have seen in the previous subsection, in particular in Equation (4.36), the existence of a maximum loftable diameter d_{max}. There is consequently a maximum possible loftable mass, in the plume model described in the previous subsection, which we denote $\overline{m}$.

So we will henceforth assume the launching distribution is a probability density $\phi(z,m)$ on $[0,\infty) \times [0,\overline{m}]$. We will examine specific assumptions, and possible functional forms for $\phi(z,m)$.

Model L1 We assume that each firebrand of mass m is lofted to a unique height $z = z(m)$, as for example in Equation (4.34). We can then define

$$\phi(z,m) = \delta(z - z(m))\mu(m), \tag{4.37}$$

where $\mu(m)$ is a given mass distribution, and δ represents the Dirac delta functional.

This approach has been standard in the literature, where one is interested in long-distance spotting events. The concern is generally in estimating the maximum possible spotting distance for a given fire intensity (e.g. [2]).

Model L2 The convection column is inherently turbulent, due to its interactions with the atmosphere. Instead of assuming that each mass is lofted to a unique height, we might instead suppose that it is launched randomly about the standard lofting height $z(m)$.

For example, we could assume that the heights are normally distributed about the lofting height, so we can write $\phi(z,m) = \mathbb{N}(z(m),\sigma)\mu(m)$, a one-sided normal distribution with mean $z(m)$ and variance σ. Again we are assuming we know the mass distribution $\mu(m)$. We can express this normal distribution as:

$$\mathbb{N}(z(m),\sigma) := \frac{A}{\sigma\sqrt{2\pi}} \exp\left(-\frac{(z - z(m))^2}{2\sigma^2}\right), \tag{4.38}$$

where the constant A chosen so that the distribution is normalized. We allow values of z to lie in some subset of $[0,\infty)$, such as $[H, z_{max}$, where H is the canopy height and z_{max} is the maximum lofting height predicted by the Baum and McCaffery plume.

If we choose $z(m)$ like in the Baum and McCaffery case, this model represents a 'smeared out' version of the Baum and McCaffery distribution. On the other hand, we are also free to explore other launching models, and employ the same approach as in (4.38) to obtain the launching distribution $\phi(z,m)$.

Another avenue for future research could be to examine, for the same launching height formula $z(m)$, which statistical distributions other than the normal distribution may more accurately describe the firebrand's turbulent flight through the convection column. In addition, the Baum and McCaffery plume may need to be replaced by a more accurate flame and plume model, depending on the type of spotting we are modelling.

Model L3

Finally, we could assume that the launching heights z, and masses m, are independent of each other, so we can write

$$\phi(z, m) = \mathbb{Z}(z)\mu(m). \tag{4.39}$$

In this context, $\mathbb{Z}(z)$ is a probability distribution which describes how firebrands are distributed with height z, and has the property that

$$\int_0^\infty \mathbb{Z}(z)dz = 1. \tag{4.40}$$

A similar sort of model was employed by Albini in the context of firebrand transport by line thermals [3]. These are well-mixed columns of air which move downwind as a coherent structure. In this case, we might assume firebrands are well-mixed, between some minimum and maximum lofting heights,

$$\mathbb{Z}(z) = U[z_{min}, z_{max}], \tag{4.41}$$

where U represents the uniform distribution on $[z_{min}, z_{max}]$.

On the other hand, if the maximum launching heights are very large, we might for example model $\mathbb{Z}(z) = \lambda e^{-\lambda z}$ for $z \geq 0$, so that we are exponentially less likely to find firebrands the higher we go. This is just one example; mathematically, exploring the possible statistical distributions, and their outcome on invasions with non-local dispersal, is an interesting and important problem.

4.6 Transport in the atmosphere

4.6.1 The atmospheric boundary layer

The atmospheric boundary layer (ABM) is the lowest portion of the atmosphere, extending on average about one kilometre, and ranging up to at most about three kilometres above the Earth's surface [50]. It consists of a number of distinct sublayers, and it is of utmost importance since the ABM is where firebrand transport occurs.

At the bottom is the laminar sublayer, which has a thickness of only a few millimetres. This is a region where high viscosity, induced by the 'roughness' of the surface, results in molecular diffusion being the basis for transport of momentum and heat [95]. Above the laminar layer is a transition region, leading into the Prandtl layer, in which turbulent convective motion is the dominant transport process [95]. The lower boundary of the Prandtl layer is called the *roughness height* y_0. At the top of the ABM is the Ekman layer, throughout which the effects of turbulent convection lessen with height, decreasing to zero near the top of the Ekman layer [95].

Firebrands are transported by convection, and hence are subject to the turbulent fluctuations in wind velocity present in the ABM. Turbulence is a dissipative process which converts kinetic energy in a fluid into heat energy, and it is essentially three-dimensional and rotational [52].

Turbulent eddies, which may be envisioned as large sheets of wind rolling over one another, exist on length scales from 10^{-3} m to 10^3 m. The largest eddies can therefore extend up to the height of the ABM [52]. In the case of a fire's convection column, the eddies swirling parallel to the column result in the entrainment of ambient air into the column [16].

Because of the inherent variability in the transport process, we introduce the standard Reynolds decomposition for the velocity components [52]. This means we decompose the horizontal velocity w into a slowly-varying mean component $\bar{w}$ and a rapidly-varying component w', so that:

$$w := \bar{w} + w'. \tag{4.42}$$

In general the mean windspeed increases with height, though exactly how this happens is effected by surface roughness and variable topography, to say nothing of the fire-ABM interactions. In our transport model we will be interested in the time-mean behavior of the stochastic flight process, so we will focus exclusively on the mean velocity $\bar{w}$. We will drop the bar in what follows for notational simplicity.

4.6.2 Model W1: Constant horizontal wind

The simplest assumption for the windspeed w is that it does not vary with height z, so that

$$w(z) = w > 0. \tag{4.43}$$

Based on the discussion in the previous subsection, this assumption is not valid throughout the entire ABM. However, there have been reports of fire situations where even short-distance dispersal of firebrands appears to be leading the fire front's advance [31]. In this case, where firebrands are not lofted so high into the ABM, the assumption (4.43) may be better justified.

4.6.3 Model W2: Logarithmic horizontal wind

Another commonly used wind model is the logarithmic profile, introduced in the context of spotting first by Albini [2]. This model is illustrated for some representative cases in Figure 4.3, and mathematically is described as:

$$w(z) = \frac{u_*}{\kappa} \log\left(\frac{z-d}{y_0}\right). \tag{4.44}$$

Appearing on the right hand side of Equation (4.44) is the von Karman constant $\kappa = 0.41$, the roughness height y_0, the zero-datum displacement d, and the friction velocity u_*. The friction velocity is generally defined by

$$u_* := \sqrt{\frac{T}{\rho}}, \tag{4.45}$$

where T is the time-mean flux of tangential momentum towards the surface, borne by turbulence outside the lower ABM and by viscosity within it [58].

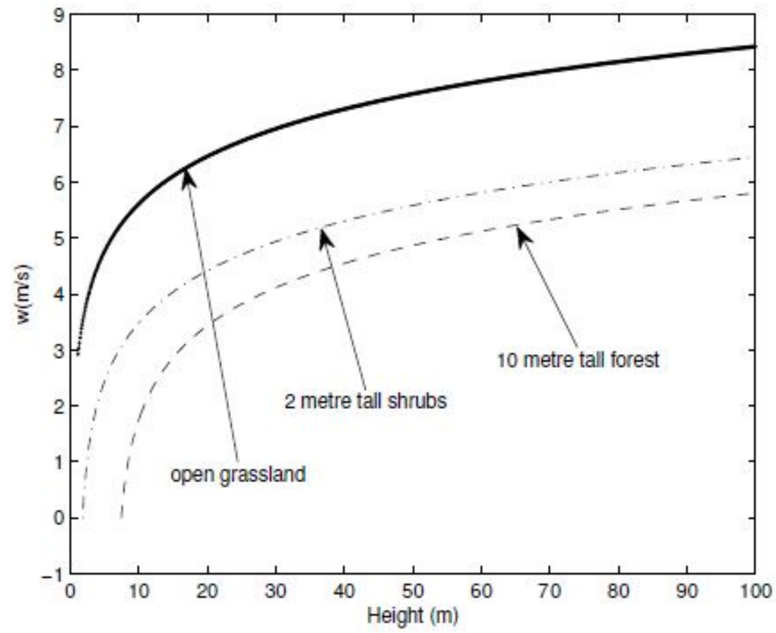

Figure 4.3: Velocity versus height for three of the logarithmic profiles, described in Equation (4.44). We have chosen a canopy height of 10 m, a friction velocity $u_* = 2$ m/s, and three representative values for the roughness height y_0 and zero-datum displacement d.

Typical values for u_* in a strongly upward-convective atmosphere are around $u_* = 2$ m/s, while for a roll-dominated atmosphere $u_* = 0.7$ m/s [84].

Recall from the first subsection that the roughness height y_0 corresponds to the lower boundary of the Prandtl layer. At the upper end examples include $y_0 = 0.5 - 1.0$ m for dense forest or suburbs, $y_0 = 0.1 - 0.5$ m for low crops or bushes, and flat grassland has $y_0 = 0.03$ m.

When there is significant roughness or dense forests, the zero-datum displacement d is employed in Equation (4.44) to offset the height at which the windspeed aloft vanishes. The value of d is usually about 2/3 the average height of the obstacles. We show velocity versus height for three different cases in Figure 4.3.

4.6.4 Model W3: Power-law wind profile

A third wind model was also first introduced in the context of spotting by Albini [2]. It assumes a power-law profile for the horizontal velocity versus

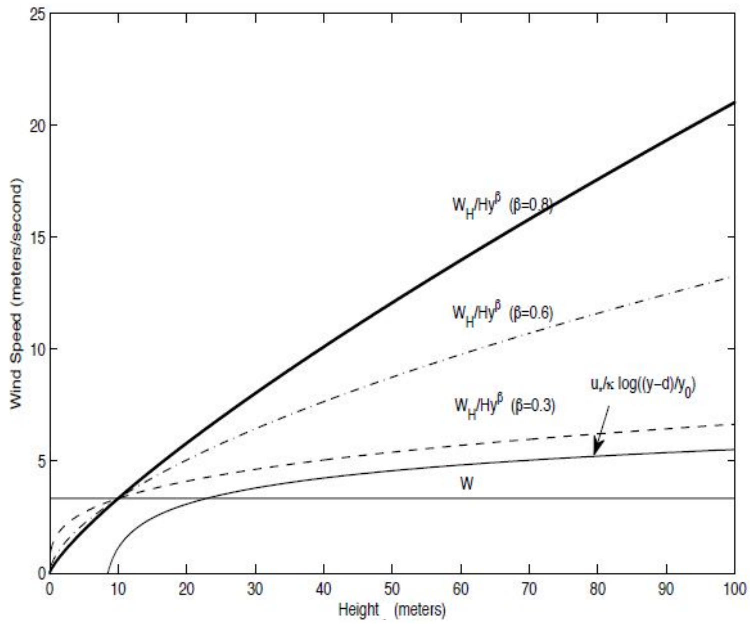

Figure 4.4: A comparison of the wind profiles discussed in this Section. Shown are three power-law models for different values of the parameter β, together with a logarithmic wind profile and a constant wind profile. We have chosen $w_H = 5$ m/s, and the canopy height to be 10 m.

height,

$$w(z) = w_H \left(\frac{z}{H}\right)^{\beta}, \tag{4.46}$$

where H is the canopy height, w_H is the windspeed at the canopy's base, and $\beta \in [0, 1]$. In Albini's work, he chose the constant $\beta = 1/7$ [3].

It should be said that the model (4.46) is a better approximation to the windflow when it is over terrain which is not covered by tall vegetation. Further, this model may be seen as an approximation to the logarithmic profile, and is consistent with the constant-wind model (to see this, set $\beta = 0$ in (4.46)).

A comparison of our three functional forms is presented in Figure 4.4.

4.7 Ignition of fuel beds by firebrands

4.7.1 Challenges in modelling fuel bed ignition

One of the most challenging problems in modelling the spotting process, is to determine the ignition probability E, which is the probability for ignition to occur once a firebrand has made contact with a given fuel bed. Since the fire landscape is very heterogeneous, the ignition probability E may vary spatially, and can depend on a variety of factors, like:

- The species of plants emitting firebrands.
- Landed firebrand characteristics like diameter, length, and mass.
- The travel time t^* from launch to landing.
- The moisture content of the fuel bed and local weather.
- The surface area, and thermal conductivity between firebrand and fuel.
- Whether the firebrand is in a 'glowing' or 'flaming' state upon landing.
- Variability of firebrand type within the launching stand (e.g. a coniferous tree might emit both small branches or cones).
- Whether there is a 're-settling' after landing due to slope or wind.
- Whether there is a shading effect from the sun due to the presence of the convection column.

An ideal model for ignition would account explicitly for all factors just mentioned. Several physics-based models have attempted to do just that (e.g. [76]), but necessarily include many equations whose analysis is mostly limited to computer simulation. Since we are interested mostly in fire fronts, which occur at the macroscopic scale, we can ignore some of the smaller-scale details in our development of ignition models.

4.7.2 Experimental investigations of firebrand ignition

Prior to 2006 the experimental investigation of this topic was limited to qualitative descriptions of ignition. The experiments show that fuel bed moisture, firebrand mass and geometry are the most important characteristics determining ignition probability ([53],[17],[31]).

The Fine Fuel Moisture Code (FFMC) used by the FBP system [40], which provides a numerical measure for the moisture contained in forest litter, has been a useful standard for determining ignition probabilities. It is determined in turn by the Fire Weather Index, another component of the FBP system [40]. The lower the FFMC, the higher the fine fuel moisture content.

Experiments by the Aerospace Corporation ([62],[63]) found that for high fine moisture contents only large flaming brands cause ignition, while for low fine fuel moisture content glowing embers may easily ignite a fuel bed.

Albini [3] reports that spotting can be significant when fine fuel moisture content is below ten percent, and confirmed the earlier results that for by [62] glowing embers can be sources of ignition.

Following these experiments, in about 2006 Manzello [54] began qualitative experiments on firebrand ignition, for brands emitted during controlled laboratory burning of pine and fir trees. This work is a collaboration between the National Institute of Standards and Technology in the USA, and the Building Research Institute in Japan [55], where ongoing experiments may help further quantify the ignition process.

One important result following from the combustion experiments of Manzello, is that firebrands are not produced if the dead fuel moisture content exceeds thirty percent. One can further postulate that there will always be a maximum moisture above which spotting does not occur. Together these results suggest, as is common knowledge, that lower fine fuel moisture content (high FFMC) can correspond to greater spotfire risk.

A still more recent paper [38], is the first to describe ignition probabilities using regression analysis on rigorous experimental data. The authors performed a number of controlled lab experiments to determine the time of ignition, rate of spread, rate of combustion, maximum and mean flame heights, and ignition frequency of fuel beds for a variety of fuel beds, representative of the fuel beds common in the parts of the Mediterranean.

Examples of fuel beds include a variety of pine, eucalyptus, and grass beds, which could also be representative of fine fuels from forests in North America and Australia. These fuels were ignited under varying values for fuel moisture, ambient windflow, bulk density, and fuel arrangement (or loading).

In terms of firebrands, the authors examined pine cones, Eucalyptus bark, acorns and twigs, and assessed their likelihood to cause ignition in terms of the fuel bed properties just mentioned.

The general results of [38] are that grasses present higher flammability risk compared to tree and bush litters, pine litter is more ignitable than hardwood litter, and an increase of the fine fuel moisture and bulk density decreases the time, but not necessarily the likelihood of ignition. Finally, firebrand type and state (i.e., glowing or flaming) are the most important determinants of ignition.

The glowing or flaming state of a firebrand had already been qualitatively discussed in a number of investigations (e.g., [31],[53],[93]). A rigorous analysis of Eucalyptus firebrands by Ellis [31], and pine or fir firebrands by Manzello [54], confirms the results of [38] that flaming firebrands present greater risk of ignition. The time-to-burnout of flaming was investigated from a theoretical perspective in [76]. Flaming ignition most likely plays a more important role in short-range spotting, where 're'-flaming is possible upon landing, and is important to consider [31].

Finally, the results of [37] suggested that there are three firebrand groups which are important for spotting. These include: heavy firebrands with the ability to sustain flames, which are efficient for long-distance spotting (e.g., pine cones, cylindrical brands); light firebrands with high surface area-volume ratios are effective for short-range spotting (e.g., Eucalyptus or pine bark plates); light firebrands with low surface-volume ratios fall somewhere in the middle of the other two classes.

4.7.3 Ignition probabilities: Models I1, I2, I3

We propose a simple assumption, namely that the ignition probability $E(x, m) = E(m)$, where m is the total landed firebrand mass at location x. This corresponds to a homogeneous medium, where the firebrand mass only is important in ignition. We will write $E(m) \in [0, 1]$.

Further, we will assume there is some critical mass $\underline{m}$ above which ignition of a fuel bed occurs with probability one. The existence of such a mass is reinforced by a experimental studies (e.g., [38],[37],[53]). The idea is simply that the greater the mass, the greater the energy exchange between firebrand and fuel bed, increasing the likelihood of ignition.

Model I1: The first possibility is that below the threshold mass $\underline{m}$, there is a non-zero probability of ignition. One functional form appearing in the literature is

$$E(m) := \begin{cases} m/\underline{m}, \, m < \underline{m}; \\ 1, \qquad m \geq \underline{m} \end{cases} \tag{4.47}$$

Model I2 A second possibility is that there is a transition region about a threshold mass $\underline{m}$, throughout which $E(m)$ abruptly but smoothly transitions from zero to one. For example,

$$E(m) = \left(1 + \operatorname{erf}\left(Am - 2\right)\right)\right) /2. \tag{4.48}$$

Here the function $\operatorname{erf}(m)$ denotes the error function, related to the standard normal distribution. The parameter A measures the steepness of the transition region; the larger A, the steeper the transition.

Model I3 A third possibility is that below some threshold mass $\underline{m}$, ignition is impossible, while it is certain to occur above this threshold mass. Using the Heaviside, or unit-step function, we can model the ignition probability in this case by

$$E(m) = H(m - \underline{m}). \tag{4.49}$$

The reader will notice that this model is a caricature or the more physically realisitic model presented in Equation (4.48). In the most extreme fire burning situations, where the fuel beds are so dry almost any landed mass will cause ignition, we can send $\underline{m} \to 0$ as an approximation. This will be relevant, and simplify the analysis in some cases that follow.

We conclude this subsection by presenting some representative examples of the three models presented in this section, in Figure 4.5. One can see the linear increase corresponding to (4.47), the smooth sigmoidal increase about $\underline{m}$ for the model (4.48), and the step function (4.49) as well.

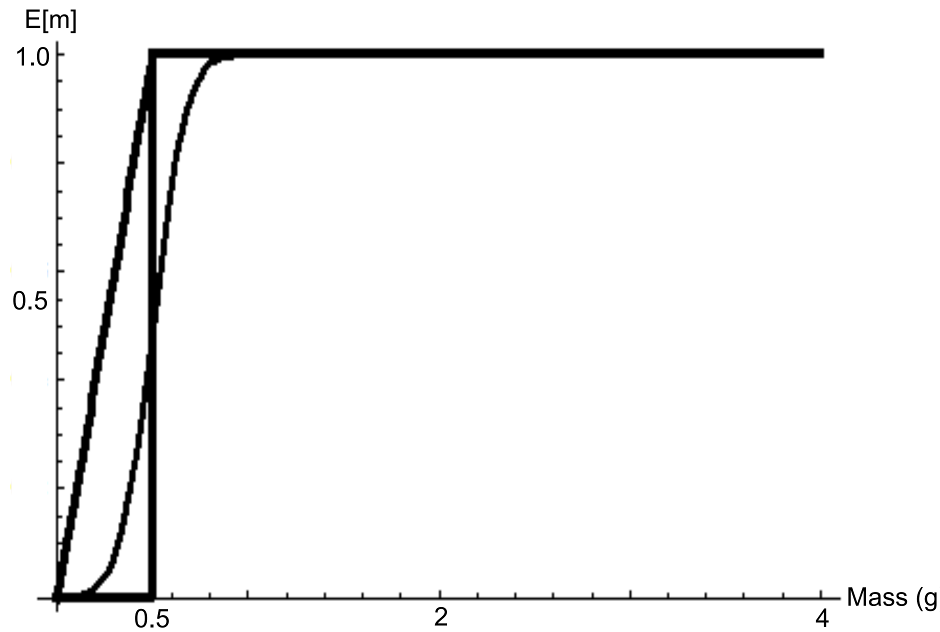

Figure 4.5: A comparison of the ignition models discussed in this section. On the y-axis we have $E(m)$ plotted versus m (measured in grams). The threshold mass is $\underline{m} = 0.5$, the parameter A in (4.48) is $A = 5$. The linear curve represents the ignition model (4.47), the sigmoidal curve represents (4.48), while the discontinuous-jump curve represents the model (4.49).

4.8 Summary of the models considered in this Chapter

Considering the number of models described in this Chapter, it is helpful to display the models, together with their references, in the Table in this Section.

Process	Number	Description	Reference
Mass distribution $\mu(m)$	G1	Power law	New; [54]
	G2	Slash burning	[90].
Combustion models $C(m_0, t)$	C0	Constant burn rate	New.
	C1	Tarifa's model	[2]
	C2	Simplified Tarifa's model	New.
	C3	Negligible combustion	New.
	C4	Fernandez-Pello model	[88].
	C5	Refinements to Fernandez-Pello model	[16],[42].
	C6	Albini's line thermal model	[3].
Temperature $T(t)$		Newton's Law of Cooling, Stefan-Boltzmann law	[16].
Terminal vertical velocity v.	V1	Constant v	[75],[31].
	V2	Experiments on cylindrical firebrands.	[63].
Plume or launching models $\phi(z, m)$		Baum and McCaffery Plume.	
	L1	Unique launching height $z(m)$	[2],[15],[16].
	L2	Normally distributed launching heights $\mathbb{N}(z(m), \sigma)$	New.
	L3	Heights and masses independent: $\phi(z, m) = \mathbb{Z}(z)\mu(m)$	New.
Atmospheric wind transport w	W1	Constant horizontal wind	New.
	W2	Logarithmic wind profile	[2],[58].
	W3	Power-law wind profile	[2],[3].
Ignition probability $E(m)$	I1	Piecewise linear ignition probability	[38],[37],[90].
	I2	Smoothed ignition probability	New.
	I3	Heaviside step function	New.

Table 4.1: Physical and empirical models for spotting subprocesses

Chapter 5

Analytic examples of the spotting distribution

5.1 Chapter Introduction

In this chapter we continue to investigate the one-dimensional impulse-release IBVP for the firebrand transport equation introduced in Chapter 3, incorporating a variety of the physical models explored in Chapter 4.

The goal is to determine the *asymptotic landing distribution* $\mathbb{L}(x, m)$, and then to use one of our ignition models, and in particular the ignition operator $E(m)$, to determine the downwind *spotting distribution* $\mathbb{S}(x) \in [0, 1]$ as in (5.32). This formula is perhaps the most important contribution to science in this thesis, as it synthesizes many possible spotting scenarios (more than 500) into a single formula.

First, in Section 5.2, we concentrate on some analytically-determined examples of the asymptotic landing distribution, obtained for constant terminal vertical velocity, for different wind models, and then in Section 5.3 we derive the general formula for the spotting distribution.

Next, in Section 5.3, we illustrate a type of 'averaged' spotting kernel, in which the realistic mass-evolution model (C4) is used, to illustrate qualitative differences in the types of kernels obtained by varying the ignition model. Which model is most applicable is a question for further research, but as explained in Chapter 4 at least model I1 has been used in the literature. We also explain how we can obtain a family of spotting kernels, including a 'fat'-tailed kernel, which is used in Chapter 7 as the prototypical example.

We also explain, in Section 5.4 and based on the results of 5.3, how we can extend the time-delayed i-PDE models from Chapter 2, to account for different horizontal wind profiles. Finally, in Section 5.5 we discuss how the spotting distribution provides a measure of the probability that an impulse release is able to cross a boundary to local spread, i.e. spotfire breaching. This is an important problem for forest fire fighters, and our approach here will be expanded upon in future work.

Remark: About the combustion models used in this chapter, and with reference to Equation (3.22): All examples discussed employ combustion models whose combustion rate does not depend on the firebrand mass. Hence we do not require an exponential term multiplying the firebrand distribution as in (3.22). In particular, in our averaged distributions, we employ the realistic combustion model (C4), while in the final two examples we assume the burning rate is constant (C0). Clearly both burning rates depend explicitly only on time.

5.2 Analytically-determined landing distributions and travel times

5.2.1 Constant wind, constant terminal velocity

The simplest case results if we choose $w > 0$ and $v < 0$ to be constants, corresponding to constant wind and constant falling terminal velocity. We will also approximate the canopy height $H \approx 0$, as we are interested in describing long-distance spotting events, on which scale the canopy height is negligible. The characteristic equations (see Chapter 4) in this case read:

$$
\begin{aligned}
\frac{dx}{dt} &= w. \\
\frac{dz}{dt} &= v. \\
\frac{\partial m}{\partial t} &= f(t, x, z, m),
\end{aligned}
\tag{5.1}
$$

where the right-hand side f appearing in the mass evolution models is determined by choosing any of the firebrand combustion models C0-C6 examined in Chapter 4.

The first two characteristic equations are easily solved,

$$
\begin{aligned}
x(t; x_0) &= wt + x_0, \\
z(t; z_0) &= vt + z_0,
\end{aligned}
\tag{5.2}
$$

where again x_0 and z_0 are the initial position and height respectively of a particular firebrand. The equation for $z(t; z_0)$ in (5.2) is defined as long as $z \geq 0$.

As explained in the section 4.3.1, we define the combustion operator $\mathcal{C}(m_0, t)$, given an initial mass m_0, so we we can express the mass $m(t; m_0)$ for future times $t > 0$ using the definition $m(t; m_0) = \mathcal{C}(m_0, t)$, provided the function f in (5.1) is Lipschitz continuous, and $m(t; m_0) \geq 0$. Again, we can define the inverse combustion operator $C^{-1}(m, t)$, which we remind the reader is the unique solution to the initial value problem $\frac{dm}{dt} = -f$, $m(0) = m$, evaluated at time $t \geq 0$. We will keep things abstract for now, and explore specific combustion models later.

Now consider a firebrand which has landed on the ground at location x'. Tracing back along the spatial characteristics, we see that the firebrand began its journey when $x_0 = 0$ and $z_0 = \frac{|v|}{w} x'$.

Appearing in the latter expression for z is the landing time $t^*(x')$, defined by:

$$
t^* := \frac{x'}{w}, \tag{5.3}
$$

which is the time that passed before the firebrand reached the ground at x'.

The landing time t^* will be important in what follows. To present a concrete example, if $w = 1$, $v = -1$, then the landing time for firebrands launched initially at $x = 0$ to arrive at $x = 2$ is $t^* = 2$.

Next, fix a point (x, z) in the quarter plane $\{(x, z) \mid x > 0, y > z\}$, and assign a time $t > 0$. If $x > wt$, then the firebrands which started at $x = 0$ have not yet reached location x, so we can determine the firebrand density $p(t, x, z, m)$ from the initial condition for p. However, if $x < wt$, then we must determine the firebrand density by integrating backwards along characteristics to the boundary at $x = 0$.

It is clear, then, that the firebrand density, provided N firebrands are released, is given by

$$p(t, x(t; x_0), z(t; z_0), m(t; m_0)) = \begin{cases} N\delta(t - t^*)\phi(z - vt, \mathcal{C}^{-1}(m, t)), & x \leq wt; \\ p(0, x - wt, z - vt, m_0), & x > wt, \end{cases} \tag{5.4}$$

where $\phi(z, m)$ is the vertical launch distribution discussed in Chapter 3.

We remind the reader that at $t = 0$ we have $p = 0$ for $x > 0$, from our initial condition for an impulse release, so we find:

$$p(t, x(t; x_0), z(t; z_0), m(t; m_0)) = \begin{cases} N\delta(t - t^*)\phi(z - vt, \mathcal{C}^{-1}(m, t)), & x < wt; \\ 0, & x \geq wt. \end{cases} \tag{5.5}$$

Recalling that the distribution of landed branches $L(t, x, m)$ is given by $\int_0^t p(s, x, 0, m)\, ds$ for $t > 0$, so we find:

$$\begin{aligned} L(t, x(t; x_0), m(t; m_0)) &= \begin{cases} N \int_0^t \delta(s - \frac{x(s;x_0)}{w})\phi(-vs, \mathcal{C}^{-1}(m, s))\, ds, & x < wt; \\ 0, & x \geq wt. \end{cases} \\ &= N\mathbb{H}(t - \frac{x(t; x_0)}{w})\phi(|v|\frac{x}{w}, \mathcal{C}^{-1}(m, \frac{x}{w})) \end{aligned} \tag{5.6}$$

where $\mathbb{H}$ represents the Heaviside, or unit-step function, defined by $\mathbb{H}(x) = 0$ for $x < 0$, and $\mathbb{H}(x) = 1$ for $x \geq 0$.

Taking the limit as $t \to \infty$ in (5.6), we obtain the asymptotic landing distribution $\mathbb{L}(x,m)$ in terms of the inverse combustion operator $\mathcal{C}^{-1}(m,t)$:,

$$\mathbb{L}(x,m) = N\ \phi(|v|\frac{x}{w}, \mathcal{C}^{-1}(m, \frac{x}{w})). \tag{5.7}$$

We impose the assumption, that if:

$$\mathcal{C}^{-1}(m, \frac{x}{w}) < 0, \quad \text{we set} \ \ \mathbb{L}(x,m) = 0. \tag{5.8}$$

This is to assure that we do not obtain any negative mass density.

We see that the asymptotic landing distribution in (5.7) is simply the number of firebrands released N, multiplied by the vertical launch distribution $\phi(z,m)$ with its arguments shifted. In Section 5.2.4 we illustrate some sample asymptotic landing distributions, for a simple launch distribution, and how the relative effects of wind, terminal vertical velocity, and combustion can play a role.

5.2.2 Power law profile for w, constant vertical velocity

This section is a generalization of the constant-wind case, which we called (W2) back in Chapter 4. Here we consider again a constant vertical velocity $v < 0$, and we recall that the power-law horizontal wind profile satisfies

$$w(z) = w_H \left(\frac{z}{H}\right)^{\beta}, \tag{5.9}$$

where H is the canopy height, w_H is the windspeed at the canopy's base, and $\beta \in (0,1)$. We are interested solely in values of $z \geq H$. Further, we will not consider resettling or within-canopy winds, so we assume once a firebrand has reached $z = H$, it travels no farther, and may or may not cause ignition at that location.

In this case, the spatial characteristics read:

$$\begin{aligned} \frac{dx}{dt} &= w_H \left(\frac{z}{H}\right)^{\beta}, \\ \frac{dz}{dt} &= v. \end{aligned} \tag{5.10}$$

Again in this case we find the solution $z(t; z_0) = z_0 + vt$, which we then

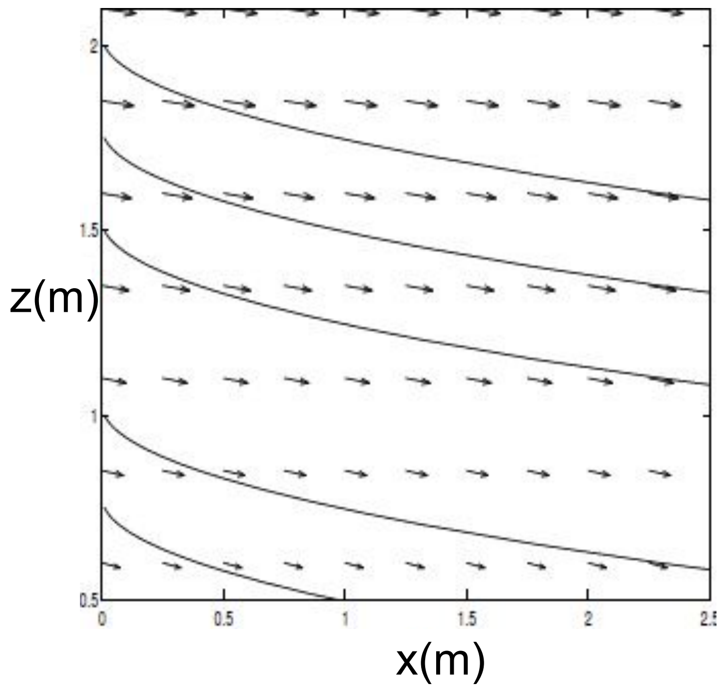

Figure 5.1: Spatial characteristics with velocity field for the power-law wind profile, with constant vertical velocity, described in (5.12). The y-axis represents heights in metres, while the x-axis represents downwind distance in metres. Here $w_H = 5$, $\beta = 0.5$, $H = 0.5$ and $v = -1$.

use to solve the equation for x. Notice that since $v < 0$, the heights z are decreasing with time. The equation (5.10) for x becomes:

$$\frac{dx}{dt} = \frac{w_H}{H^\beta}(z_0 + vt)^\beta \tag{5.11}$$

Integrating both sides with respect to t, we obtain:

$$x(t) = x_0 + \frac{w_H}{v(\beta+1)H^\beta}\left((z_0 + vt)^{\beta+1} - z_0^{\beta+1}\right). \tag{5.12}$$

Trajectories for (5.12) are illustrated in Figure 5.1.

Now consider a firebrand which reaches the canopy at (x, H). We wish to determine the landing time $t^*(x)$ which it took for the firebrand to travel from $x = 0$ at time $t = 0$ to the top of the canopy at $z = H$. As in the preceding subsection, we will run the characteristics in reverse. To do this, we choose

$x_0 = x$, $z_0 = H$, $t = t^*$ and $x(t^*) = 0$, and insert these values into:

$$x(t) = x_0 + \frac{w_H}{|v|(\beta+1)H^\beta}\left((z_0 + |v|t)^{\beta+1} - z_0^{\beta+1}\right). \tag{5.13}$$

We obtain:

$$0 = x + \frac{w_H}{|v|(\beta+1)H^\beta}\left((H + |v|t^*)^{\beta+1} - H^{\beta+1}\right). \tag{5.14}$$

Solving for t^* in terms of x in Equation (5.14), we obtain:

$$t^*(x) = \frac{1}{|v|}[\left(\frac{H^\beta(\beta+1)|v|}{w_H}x - H^{\beta+1}\right)^{\frac{1}{\beta+1}} - H]. \tag{5.15}$$

Similar to the previous subsection, we find the exact solution p of our impulse IBVP for the transport and combustion process:

$$p(t, x(t; x_0), z(t; z_0), m(t; m_0)) = \begin{cases} N\delta(t - t^*)\phi(z - vt^*, \mathcal{C}^{-1}(m, t^*)), & x < \int_0^t \mathbb{F}(s)\, ds; \\ 0, & x \geq \int_0^t \mathbb{F}(s)\, ds, \end{cases} \tag{5.16}$$

where

$$\mathbb{F}(s) := w(z(s; z_0)), \tag{5.17}$$

so that the bounds on x appearing in (5.16) can be written in explicit terms, using the relation (5.12), through the following expression:

$$\int_0^t \mathbb{F}(s)\, ds := \frac{w_H}{|v|(\beta+1)H^\beta}\left((z_0 + |v|t)^{\beta+1} - z_0^{\beta+1}\right). \tag{5.18}$$

We can interpret the latter integral (5.18) as the location of the leading edge of the expanding firebrand distribution $p(t)$, since $p(t) = 0$ for $x \geq \int_0^t \mathbb{F}(s)\, ds$, but $p(t) \geq 0$ when $x < \int_0^t \mathbb{F}(s)\, ds$.

In particular, from (5.18) we see that $\lim_{t\to\infty} \int_0^t \mathbb{F}(s)\, ds = \infty$. Hence we can repeat the steps from the previous subsection (see e.g. (5.7) and the steps leading up to it), and we find the asymptotic landing distribution is again:

$$\mathbb{L}(x, m) = N\phi(H + |v|t^*(x), \mathcal{C}^{-1}(m, t^*(x))), \tag{5.19}$$

but in this subsection the landing time t^* is given by (5.15), and again we set $\mathbb{L}(x, m) = 0$ if $\mathcal{C}^{-1}(m, t^*(x)) < 0$ (i.e. we only consider nonnegative masses).

The asymptotic landing distribution is still determined by the vertical launch distribution $\phi(z, m)$, as in the case (5.7). Again, the asymptotic landing distribution is a scaled version of the launch distribution. In this case the landing time has the more complicated form (5.15), and in addition we include the canopy height H in the final form of the distribution . Further, the formula for the landing time derived here is consistent with the zero-canopy, constant-wind case (5.3), which is easily seen by setting $\beta = 0$ in (5.15).

5.2.3 Logarithmic profile for w, constant vertical velocity

In this subsection, we again assume a constant vertical velocity $v < 0$, and we recall that the logarithmic horizontal wind profile satisfies

$$w(z) = \frac{u_*}{\kappa} \ln\left(\frac{z-d}{z_0}\right). \tag{5.20}$$

where the various parameters are discussed in Chapter 4, Section 5.3. In particular we recall that $z \geq H + d \approx H$, where H is the canopy height and d is the distance above the canopy where horizontal winds begin. We will approximate $d \approx 0$.

In this case, the spatial characteristics read:

$$\begin{aligned} \frac{dx}{dt} &= \frac{u_*}{\kappa} \ln\left(\frac{z-d}{y_0}\right), \\ \frac{dz}{dt} &= v. \end{aligned} \tag{5.21}$$

We will define $A := \frac{u_*}{\kappa}$, and introduce the new variable $\tilde{z} = z - d$. The first differential equation in (5.21) then reads $\frac{dx}{dt} = A \ln \frac{\tilde{z}}{z_0}$ (dropping the tilde under the logarithm in what follows for convenience).

As in the preceding subsection, we consider a point (x_0, H) at the top of the canopy and then determine the landing time t^*. Using the initial condition $z_0 = H$, and running the characteristic equations (5.21) in reverse, we see that $z(t) = H - vt = H + |v|t$, and inserting this into our transformed equation for

x, we find:

$$x(t) = x_0 - A \int_0^t \left(\ln\left(H + |v|s\right) - \ln y_0\right) ds$$
$$= x_0 - tA \ln y_0 - A \int_0^t \ln\left(H + |v|s\right) ds. \tag{5.22}$$

Now setting $u := H - vs$, we see $du = -vds$, so we can further simplify Equation (5.22) to obtain:

$$\begin{aligned} x(t) &= x_0 - tA \ln y_0 + \frac{A}{v} \int_H^{H+|v|t} \ln u du \\ &= x_0 - tA \ln y_0 + \frac{A}{v}(u \ln u - u) \mid_H^{H+|v|t} \\ &= x_0 - tA \ln y_0 + \frac{A}{v}\left(H \ln\left(H + |v|t\right) + |v|t \ln\left(H + |v|t\right) + vt\right). \end{aligned} \tag{5.23}$$

Next we set $x(t^*) = 0$ in the latter Equation (5.23), and substituting back in our original variables for A we find an implicit expression for the landing time t^*, replacing x_0 with x,

$$\frac{u_*}{\kappa} H \ln H - x + \frac{t^* u_*}{\kappa}(\ln H - 1) = \frac{u_*}{v\kappa}\left(\left(H + |v|t^*\right) \ln\left(H + |v|t^*\right)\right) \tag{5.24}$$

For given values of the parameters (u_*, H, v) we can then use a numerical method, like Newton's iterative root-finding method, to compute the landing time as a function of x to any desired precision.

Because the landing time t^* must be increasing with x by uniqueness of firebrand trajectories and the monotonicity of $w(z)$, we repeat the steps of the preceding subsection, leading to Equation

$$p(t, x(t; x_0), z(t; z_0), m(t; m_0)) = \begin{cases} N\delta(t - t^*)\phi(z - vt^*, \mathcal{C}^{-1}(m, t^*)), & x < \int_0^t \mathbb{F}(s)\, ds; \\ 0, & x \geq \int_0^t \mathbb{F}(s)\, ds, \end{cases} \tag{5.25}$$

where

$$\mathbb{F}(s) := w(z(s; z_0)). \tag{5.26}$$

Again we can argue that $\lim_{t\to\infty} \int_0^t \mathbb{F}(s) = \infty$, so as in the previous examples we can first obtain $L(t, x, m)$, and then the asymptotic landing distribution,

$$\mathbb{L}(x, m) = N\phi(H + |v|t^*(x), \mathcal{C}^{-1}(m, t^*(x))), \tag{5.27}$$

which has exactly the form (5.19), except in this case t^* in this case must be solved implicitly from (5.24).

5.2.4 Model (W1, V1, C0, L3): a simple illustration of $\mathbb{L}(x, m)$

In this subsection we consider a simple scenario in order to visualize the asymptotic landing distribution. So, we choose $w > 0$, $v < 0$, and $f < 0$ to be constants. Further, we suppose that the launching distribution $\phi(z, m) := \mathbb{Z}(z)\mu(m)$, so that the launching heights are independent of mass. We denote this model (W1,V1,C0,L3) with reference to Chapter 4. We also assume that N is the total number of firebrands being launched, and $\mathbb{Z}$ and μ are probability distributions for the continuous random variables z and m.

Case 1 First suppose $\mathbb{Z} = U(H, \overline{z})$, where U is the uniform distribution on the interval $z \in (H, \overline{z})$, and $\overline{z}$ is the maximum possible lofting height. That is,

$$\mathbb{Z}(z) := \begin{cases} \frac{1}{\overline{z}-H}, & z \in [H, \overline{z}]; \\ 0, & \text{otherwise.} \end{cases} \tag{5.28}$$

Physically, H denotes the minimum lofting height, like the height of the forest canopy in a crown fire.

Next, let us require that the masses are also uniformly distributed, so that:

$$\mu(m) := \begin{cases} \frac{1}{\overline{m}}, & m \in [0, \overline{m}]]; \\ 0, & \text{otherwise.} \end{cases} \tag{5.29}$$

Again $\overline{m}$ represents that maximum loftable firebrand mass. The experiments of Manzello [54] suggest the maximum firebrand mass is about 4 grams; one

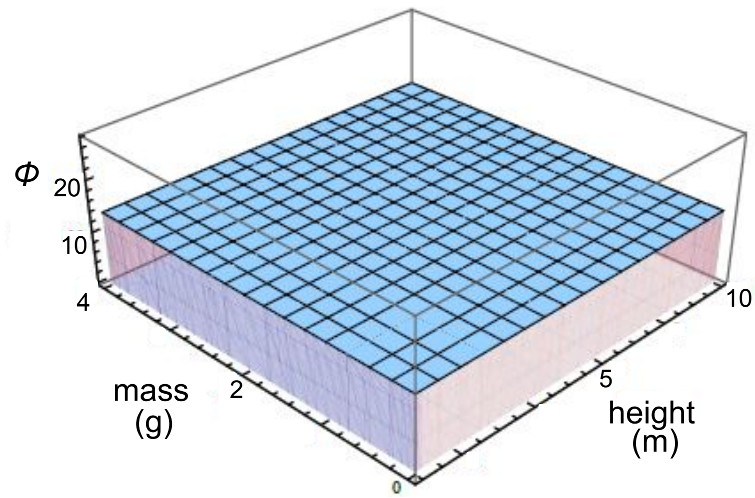

Figure 5.2: We present an illustration of 500 realizations of the random variables for height z and mass m, measured in metres and grams respectively, uniformly and independently distributed as in Equations (5.28) and (5.29). The parameters are $H = 1$, $\overline{z} = 10$, and $\overline{m} = 4$. Because of the number of points, the surface $\phi(z, m)$ appears continuous, although in fact the blue checkered plane is really an interpolation of the 500 random variable realizations from the launching distribution.

must bear in mind this data applies only to cylindrical firebrands emitted from the conifers studied in [54]. If one considers other firebrand classes, like pine cones, one could expect larger values for $\bar{m}$.

Such a launching distribution could correspond, for example, to the lofting of firebrands by well-mixed line thermals, or the prolific and significant short-range spotting which has been observed to drive fire fronts in Eucalyptus-grassland fires in Australia [31].

In Figure 5.2, we show $N = 500$ realizations of the random variables z and m, distributed according to $\phi(z, m)$, for the uniform distributions just described.

Next, we wish to determine how this initial distribution ϕ becomes the asymptotic landing distribution $\mathbb{L}$. As discussed in the derivation of (5.7), we find

$$\mathbb{L}(x, m) = NZ(|v|\frac{x}{w})M(m + f\frac{x}{w}). \tag{5.30}$$

The important parameters are v, w, and f. In Figure 5.3 we show $\mathbb{L}(x, m)$ for $v = w = 1$, and vary the combustion constant f to demonstrate its effect.

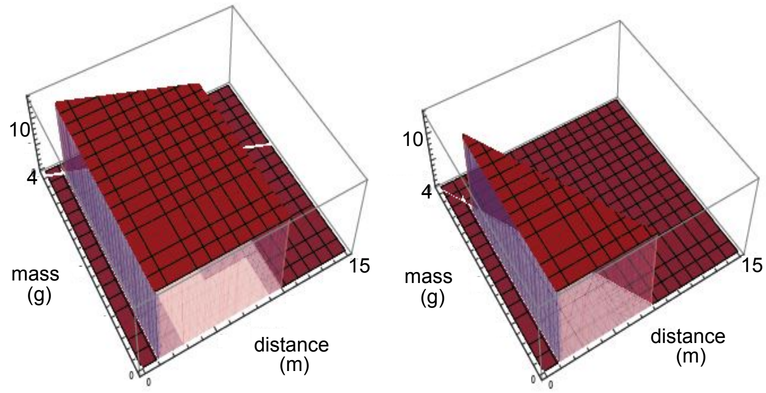

Figure 5.3: Here we illustrate the asymptotic landing distribution as a surface above the (x, m)-plane, corresponding to the initial distribution illustrated in Figure 5.2. Distance is measured in metres, while mass is measured in grams. Here $v = w = 1$ in both graphs, while $H = 1$, $\bar{z} = 10$. In the leftmost graph, the burning rate $|f| = 0.1$, while in the right graph $|f| = 0.5$.

It is clear that if we have higher burning rates, both that less mass is observed asymptotically, and also higher burning rates constrain firebrands to travel less distance. Also notice that there are fewer larger firebrands the further we proceed along the x-axis, as illustrated by the slanted cutoff on the $\mathbb{L}(x, m)$ surfaces.

Next, in Figure 5.4, we have $N = 1000$ firebrands, and we fix $|f| = 0.1$, $v = 1$, and vary w between $w = 4$ and $w = 8$. Doubling the windspeed results in firebrands traveling much further, and in addition less firebrands reach the ground. Another observation is that the lower bound on the distance x at which the firebrand density is non-zero moves to the right when we double the windspeed.

Finally we are interested in the effect of changing the terminal velocity. This is illustrated and described in Figure 5.5. It is clear that more firebrands are conserved, and the firebrands travel farther, when v is made smaller. Also the spatial lower bound at which $\mathbb{L}(x, m)$ drops off to zero increases as we decrease v.

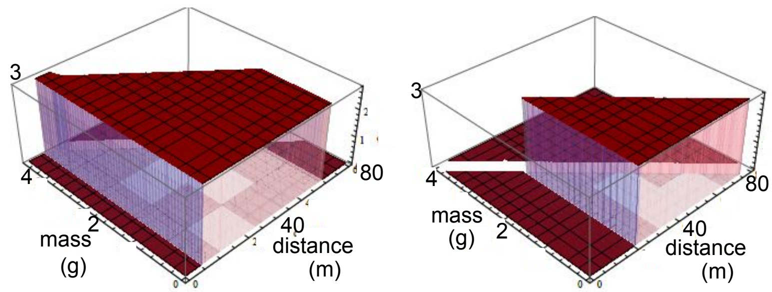

Figure 5.4: Here we illustrate the asymptotic landing distribution as a surface above the (x, m)-plane, corresponding to a similar initial distribution illustrated in Figure 5.2, but this time with $H = 10$, $N = 1000$, $\overline{m} = 4$, $v = 1$, $|f| = 0.1$, and $\overline{z} = 100$. The figure on the left corresponds to setting $w = 4$, while the figure on the right corresponds to setting $w = 8$.

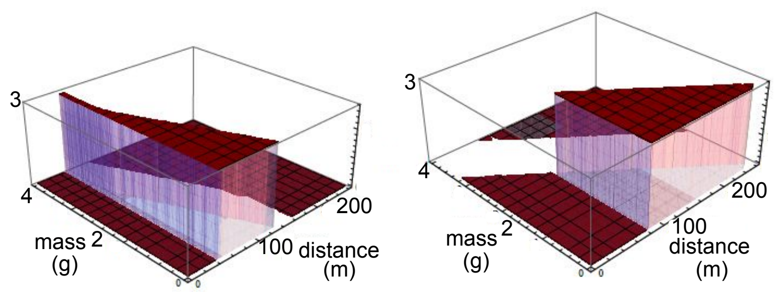

Figure 5.5: Here we illustrate the asymptotic landing distribution as a surface above the (x, m)-plane, corresponding to a similar initial distribution illustrated in Figure 5.2, but this time with $H = 10$, $N = 1000$, $\overline{m} = 4$, $w = 4$, $|f| = 0.1$, $\overline{z} = 100$. The figure on the left corresponds to setting $v = 4$, while the figure on the right corresponds to setting $v = 1$.

5.3 The spotting distribution $\mathbb{S}(x)$ determined from $\mathbb{L}(x, m)$

The uniqueness of firebrand trajectories considered in this Chapter, and the assumption that the ignition probability $E(m)$ depends only on the landed mass, will allow us to use the asymptotic landing distributions $\mathbb{L}(x, m)$ obtained in the previous section, to obtain the spotting distribution $\mathbb{S}(x)$.

Recall that $\mathbb{L}(x, m)$ denotes the mass distribution which eventually lands at location x due to an impulse release at location $x = 0$. Hence the *total landed mass distribution* $M(x)$ is what we need to determine the ignition distribution, since we are assuming our medium is homogeneous, and ignition is approximated to be instantaneous.

We can determine the total landed mass distribution by integrating $\mathbb{L}(x, m)$, in terms of the inverse combustion operator $\mathcal{C}^{-1}(t, m)$:

$$\begin{aligned} M(x) &= \int_0^{\bar{m}} m \, \mathbb{L}(x, m) \, dm \\ &= N \int_0^{\bar{m}} m \, \phi(H + |v| t^*(x), \mathcal{C}^{-1}(m, t^*(x)) \, dm. \end{aligned} \tag{5.31}$$

Finally, since the continuous ignition operator $E(m) \in [0, 1]$ depends only on the landed mass, it follows that the *spotting distribution* $\mathbb{S}(x) \in [0, 1]$, which characterizes the probability of a spotfire igniting due to an impulse release from $x = 0$, is given by:

$$\begin{aligned} \mathbb{S}(x) &= E\left(M(x)\right) \\ &= E[N \int_0^{\bar{m}} m \, \phi\left(H + |v| t^*(x), \mathcal{C}^{-1}(m, t^*(x))\right) \, dm], \end{aligned} \tag{5.32}$$

where the time $t^*(x)$ is the landing time.

We can extend this concept to firebrands released at location $x - y$, at time $t - t^*(x - y)$, to determine:

$$\mathbb{S}(x - y) = E\left(M(x - y)\right). \tag{5.33}$$

The expression $\mathbb{S}(x)$ in (5.32) will be used to define spotting redistribution kernels, which appear in our i-PDE models from Chapter 2. The formula (5.33) describes the kernel for a firebrand release at $x - y$, at time $t - t^*(x - y)$. We notice that our formula generalizes the expression for the spotting distribution determined in Chapter 2, where we considered the continuous limit of a discrete-time transport and ignition model.

5.4 Some example spotting kernels

In this section, we will make the approximation $H \approx 0$, or instead one could consider the line $y = 0$ as the canopy height H.

5.4.1 Case (I1): Spotting kernel for (W1,V1,C4,L1)

The ignition model (I1) prescribes a threshold mass $\underline{m}$, with the probability of ignition $E(m)$ increasing in a piecewise linear manner. We can rewrite the functional form for the ignition probability as

$$E(m) = \frac{m}{\underline{m}} + \left(1 - \frac{m}{\underline{m}}\right) H(m - \underline{m}), \quad m \in [0, \bar{m}]. \tag{5.34}$$

Example 1. Consider the combustion model (C4) from Chapter 4. We further assume constant windspeed w and terminal velocity v. Finally we assume we have the launching model L1, which assumes a unique launching height for each firebrand mass. We denote this model (W1,V1,C4,L1).

The total landed mass distribution was described in Equation (5.31). Since we assume we have cylindrical firebrands, we can compute their masses:

$$m = \rho Vol(r, L) = \rho \pi r^2 L, \tag{5.35}$$

where ρ is the mass density, r and L are values for the firebrand radius and length respectively. According to the results of Manzello [53], the average radius is $r = 0.004$ m, and the average length is $L = 0.05$ m. There is a linear relationship between the radius and length [53], so we could determine an upper and lower bound for the masses using the relationship (5.35) and the results from [53]. Of course, we already know from [53] that the masses range between 0.1 and 4 grams.

For the combustion model (C4), it follows that the mass $m(t)$ resulting due to combustion of a single firebrand, with initial mass $m(0) = \rho(0)\pi L r(0)^2$ (for the average choices of L and $r(0)$ listed in the previous paragraph), after an impulse release at the origin satisfies:

$$m(t) = \rho(t) Vol(r(t), L) = \pi\ L\ (\frac{\rho(0)}{(1 + \eta t^2)} (r(0)^4 - \frac{\chi \beta^2}{16} t^2))^{1/2}, \tag{5.36}$$

Recall that in the model (I1), each firebrand mass $m(0)$ is launched to a unique height $z(m(0))$. In this example we do not necessarily assume the same launching height as the Baum and McCaffery plume's predictions from Chapter 4, but just that there is such a unique launching height.

Because of the uniqueness of the spatial firebrand trajectories, we can determine the distribution $M(x)$ resulting from an impulse release of firebrands of mass $m(0) = \rho(0)L\pi r(0)^2$ at $x = 0$ and time $t = 0$. The uniqueness of trajectories implies the uniqueness of a landing time $\frac{x}{w}$ for each location x. By inserting this landing time into (5.36), we obtain the landed mass distribution $M(x)$:

$$M(x) = 4\left(\frac{\rho(0)}{(1+\eta(\frac{x}{w})^2)}(r(0)^4 - \frac{\chi\beta^2}{16}(\frac{x}{w})^2)^{1/2}\right), \tag{5.37}$$

provided $M(x) \geq 0$, and otherwise we set $M(x) = 0$.

This is a sort of average mass distribution, in the sense that we fix $r(0)$ to be the average firebrand radius, and L to be the average length. We do not compute the launching height $z(M(r(0), L))$, but know that the launching height varies continuously, so as to produce a continuum of landing locations x and corresponding landing times $\frac{x}{w}$.

We then replace the mass at that height $z(M(r(0), L))$ with four times the average firebrand mass (determined by average values for $r(0)$ and L in (5.35)), to produce the *averaged spotting distribution*. The mass was chosen so that approximately four grams of firebrands are launched at each point. We will examine a similar model with the other two ignition models I2 and I3, so that we will demonstrate a simple way of visualizing some qualitative differences between spotting distributions for models I1,I2, and I3.

Then according to our ignition model (5.34), and the expression (5.37), the spotting distribution $\mathbb{S}(x)$ is given by:

$$\begin{aligned}\mathbb{S}(x) = &\frac{1}{\underline{m}}\left(4\,\pi L\frac{\rho(0)}{(1+\eta(\frac{x}{w})^2)}(r(0)^4 - \frac{\chi\beta^2}{16}(\frac{x}{w})^2))^{1/2}\right)\\ +&\frac{1}{\underline{m}}\left(1 - 4\,\pi L\frac{\rho(0)}{(1+\eta(\frac{x}{w})^2)}(r(0)^4 - \frac{\chi\beta^2}{16}(\frac{x}{w})^2)^{1/2}\right)\times\\ &H\left(4\,\pi L\frac{\rho(0)}{(1+\eta(\frac{x}{w})^2)}(r(0)^4 - \frac{\chi\beta^2}{16}(\frac{x}{w})^2)^{1/2} - \underline{m}\right),\end{aligned} \tag{5.38}$$

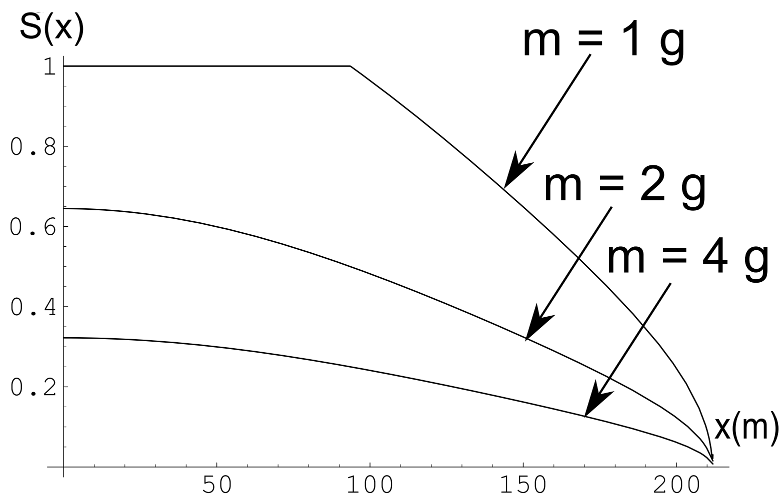

Figure 5.6: Here we show the spotting distribution $\mathbb{S}(x)$ corresponding to Equation (5.38) and the case (I1) of unique launching heights, for mass threshold values $\underline{m} = 0.001$ kg, $\underline{m} = 0.002$ kg, and $\underline{m} = 0.004$ kg. The variable x is measured in metres and is plotted along the x-axis. The parameters are $\chi = 3.5$, the initial density of wood is $\rho(0) = 513$ kg/m^3, the Schmidt number is 0.7, the Reynolds number is 2, the windspeed $w = 4$ m/s, $r(0) = 0.004$ m, $\beta = 6.5 \times 10^{-7}$ m while $L = 0.05$ m.

provided $\mathbb{S}(x) > 0$, and otherwise we set $\mathbb{S}(x) = 0$. The parameters χ and β are as described in the subsections from Chapter 4 which discuss the model (C4). We will plot this distribution for a variety of the possible ignition thresholds $\underline{m}$, in Figure 5.6. The probability of spotting clearly decreases with an increase in the threshold $\underline{m}$. The square root appearing in the formula (5.34) means in this case the spotting distribution is 0 for $x > 210$ m.

5.4.2 Case (I2): Spotting kernel for model (W1,V1,C4,L1)

The ignition model (I2) is similar to the case (I1), in that there is again a threshold mass $\underline{m}$, except that $E(m)$ is smoothed out. In particular, we recall that

$$E(m) = (1 + \operatorname{erf} A(m - 2))/2, \tag{5.39}$$

where A is a parameter which determines the steepness of the transition from $E = 0$ to $E = 1$.

We could choose, for example, $A = 1$, and we find a smooth transition to

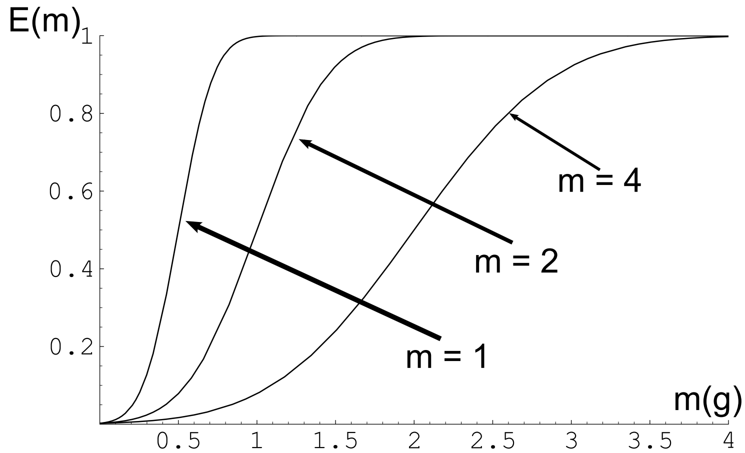

Figure 5.7: A plot of the ignition probability $E(m)$ described in (5.39), for the choices $A = 1,\ 2,\ 4$, which correspond to the transition of E to 1 at $m = 1, 2, 4$ grams respectively. Modifying the parameter A can be thus be thought of as changing the ignition threshold.

$E(m) = 1$ when $m = 4$ g. Alternatively, by choosing $A = 2$ we find this the probability goes to 1 about when $m = 2$, and choosing $A = 4$ we find the probability E goes to 1 at about $m = 1$. This is visualised in Figure 5.7 below.

Example 2: As Example 1 from the preceding subsection, consider the case of constant wind w and terminal velocity v, and apply the combustion model (C4). We will again assume the launching model L1, so each mass is launched to a unique height. So again we deal with the model (W1,V1,C4,L1).

For comparison's sake we follow the same steps as in Example 1 leading to the expression (5.37) for the *averaged landed mass distribution.* Recall that we assume there is a unique launching height for each z as is usual with model L1, however here the height is not necessarily that specified by the Baum and McCaffery plume. However, because of uniqueness of firebrand trajectories, there is a continuum of landing locations and times, and consequently a continuum of launching heights, so we can safely assume the existence of these unique launching heights for each mass. Our trick is then to replace each mass by four times the average firebrand mass.

Having repeated the steps to arrive at (5.37), employing the ignition model

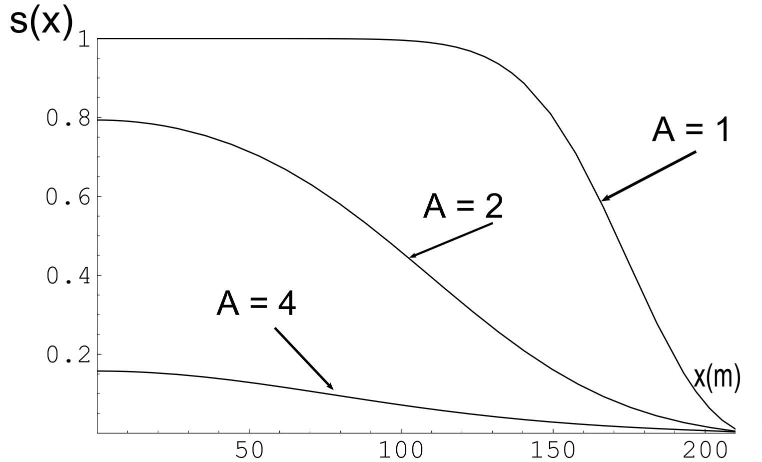

Figure 5.8: A plot of the spotting distribution (5.40) versus x (measured in metres), for the same choices of parameter described in the caption to Figure 5.6, but allowing A to vary between $A = 1, 2, 4$. Varying A like this corresponds to changing the threshold mass m at which ignition is certain, from $m = 4, 2$, and 1 grams respectively.

(5.39) we find the spotting kernel reads:

$$\mathbb{S}(x) = 4\frac{1}{2}\left[1 + \operatorname{erf}\left[N\left(4\,\pi L\frac{\rho(0)}{(1+\eta(\frac{x}{w})^2)}(r(0)^4 - \frac{\chi\beta^2}{16}(\frac{x}{w})^2))^{1/2}\right) - 2\right]\right], \tag{5.40}$$

where the factor $N = 1000$ is required to convert from kg to grams.

In Figure 5.8 below, we illustrate the spotting kernel $\mathbb{S}(x)$ for (5.40), for the different values of A appearing in the ignition probability considered in this Section, and as illustrated in Figure 5.7.

5.4.3 Case (I3): The kernel for model (W1,V1,C4,L1); The kernel for (W1,V1,C0,L3) from 5.1.4.

Our final ignition model I3 again contains a threshold mass $\underline{m}$, except in this model we suppose that below the threshold no ignition occurs, while above the threshold ignition is certain. We repeat that the functional form for $E(m)$ is given by

$$E(m) = \mathbb{H}(m - \underline{m}), \tag{5.41}$$

where $\mathbb{H}(m)$ is the Heaviside, or unit step function.

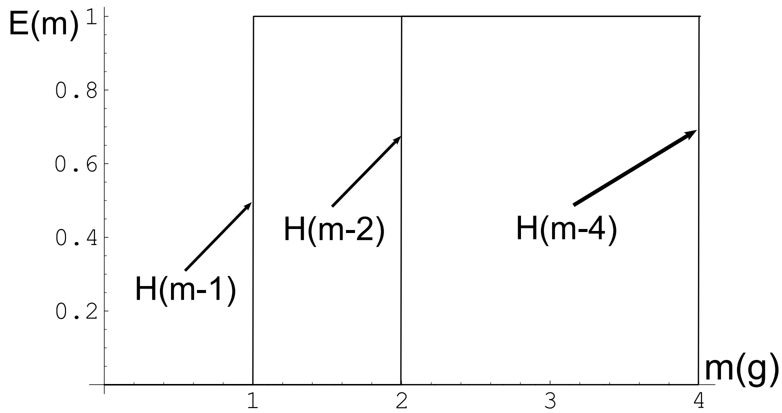

Figure 5.9: A plot of the ignition probability densities given in (5.41), changing the threshold mass $\underline{m}$ at which ignition is certain, from $\underline{m} = 4, 2$, and 1 grams respectively. These ignition probabilities assume that ignition does not occur if the landed mass is less than the threshold mass, so that for example $\mathbb{H}(m-1)$ is zero for $m < 1$.

This ignition model is illustrated for three threshold masses, namely $m = 1$, 2, or 4 grams, in Figure 5.9.

It will also be useful to consider the case where $\underline{m} \to 0$, which results in

$$E(m) = \mathbb{H}(m), \tag{5.42}$$

and since $E(m) > 0$ for any $m > 0$, consequently *any* landed mass will result in ignition. This would correspond to a fire scenario where the fuel beds are extremely dry.

Example 3: First we consider the model (W1,V1,C4,L1), and as discussed in Examples 2 and 3 we will determine the landed mass distribution by assuming each mass is launched to a unique height, to obtain an *averaged landed mass distribution* by replacing the mass at each height by four times the average initial firebrand mass. To reiterate, we assume constant $w > 0$, $v < 0$, and the combustion process is governed by Equation (5.36).

Repeating the process from Examples 1 and 2 used to arrive at (5.37), assuming that N firebrands are launched, employing the ignition model (5.39)

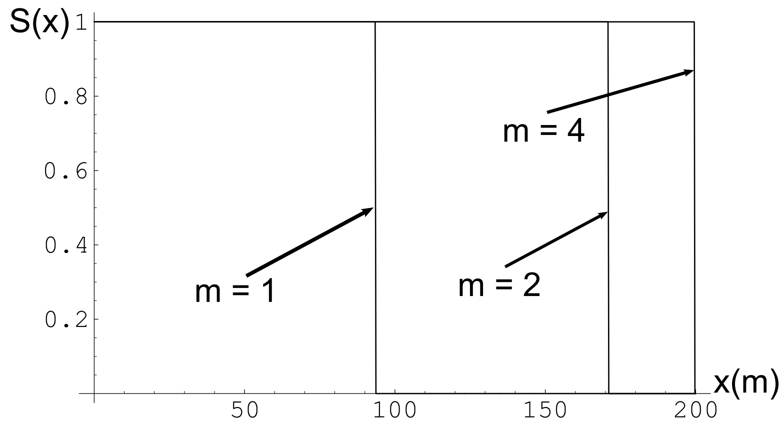

Figure 5.10: A plot of the spotting distribution (5.43), changing the threshold mass m at which ignition is certain, from $m = 4, 2$, and 1 grams respectively (see Figure 5.9 for an illustration of the corresponding ignition operators $E(m)$). We notice that in contrast to Examples 1 and 2, the spotting distribution suddenly jumps from $E = 1$ down to $E = 0$ at a single point. The support of the spotting kernel $\mathbb{S}(x)$ for the cases $\underline{m} = 1$ or $\underline{m} = 2$ is considerably less than the corresponding spotting kernels described in the Examples 1 and 2 above.

we find the spotting kernel reads:

$$\mathbb{S}(x) = \mathbb{H}\left(10004\,\frac{\rho(0)}{(1+\eta(\frac{x}{w})^2)}(r(0)^4 - \frac{\chi\beta^2}{16}(\frac{x}{w})^2)^{1/2} - \underline{m}\right), \tag{5.43}$$

where the constant 1000 appearing in (5.43) is the conversion factor between g and kg, and it is required since we measure $\underline{m}$ in grams.

In Figure 5.10 below, we illustrate the spotting kernel $\mathbb{S}(x)$ for (5.43), for different values of $\underline{m}$ appearing in the ignition probability considered in this subsection, in particular for the ignition operators E depicted in Figure 5.9.

Example 4:

In this example we assume constant $w > 0$, $v < 0$, we choose the combustion model C0 with burning rate $f < 0$. The launching model L3 means that the launching heights z and masses m are independent, so that the launch distribution has the general form $\phi(z, m) = \mathbb{Z}(z)\mu(m)$. We denoted this model (W1,V1,C0,L3) earlier in this chapter. Further, we assume a constant canopy height H and consider only values of $z \geq H$.

Let's prescribe the threshold mass to be $\underline{m} = 1$, and consider the asymptotic landing distributions determined in Chapter 5.1.4. Recall there we chose $\mathbb{Z}(z) = U(H, \bar{z})(z)$, the uniform distribution on $z \in [H, \bar{z})$, where $\bar{z}$ is the maximum possible lofting height. To determine the landed mass distribution $M(x)$, we will employ the formula (5.31), for an impulse release on N firebrands.

For the choice prescribed in Equation (5.30), we find:

$$\begin{aligned} M(x) &= N \int_0^4 mZ(|v|\frac{x}{w})\mu(m + f\frac{x}{w})dm \\ &= NZ(|v|\frac{x}{w}) \int_0^4 m\mu(m + f\frac{x}{w})dm. \end{aligned} \tag{5.44}$$

The quantity under the integral in the final equality is zero if $m + f\frac{x}{w}$ does not lie in the interval $[0, 4]$, and $1/4m$ otherwise. In particular if $m + f\frac{x}{w} < 0$, then the integral is zero, and similarly if $m + f\frac{x}{w} > 4$ then the integral is also zero. So to get a nonzero value for $M(x)$ we require that:

$$x < \frac{m\ w}{|f|} \qquad \text{and} \qquad x > (4 - m)\ \frac{w}{f}. \tag{5.45}$$

So, the region where we expect a nonzero value for $M(x)$ is the interval $((4 - m)\frac{w}{f}, \frac{mw}{|f|})$. However, since $m \leq 4$, $w \geq 0$ and $f < 0$, it follows that the lower bound $(4 - m)\frac{w}{f} < 0$, so instead we could expect non-zero values for $M(x)$ possibly for $x \in (0, \frac{m\ w}{|f|})$.

Further, we require that $H < |v|\frac{x}{w} < \overline{z}$ in order to get a nonzero solution i.e. we require $x > \frac{H\ w}{|v|}$ and $x < \frac{\overline{z}w}{v}$. Set

$$\delta = \min\left(\frac{\overline{z}w}{v}, \frac{mw}{|f|}\right). \tag{5.46}$$

. Then we can only expect non-zero values for $M(x)$ for:

$$x \in \left(\frac{Hw}{|v|}, \delta\right). \tag{5.47}$$

Finally, for x satisfying (5.47), we now know that (5.44) simplifies to:

$$\begin{aligned} M(x) &= \frac{1}{\underline{m}} \frac{N}{\overline{z} - H} \frac{1}{4} \int_{\frac{Hw}{|v|}}^{\delta} m dm \\ &= \frac{Hw}{|v|} \frac{N}{8} ((\delta)^2 - (\frac{Hw}{|v|})^2). \end{aligned} \tag{5.48}$$

So our spotting operator becomes, for values of x where $M(x) \geq 0$ as above,

$$\mathbb{S}(x) = E[M(x)] = H(1 - \frac{Hw}{|v|} \frac{N}{8} ((\delta)^2 - (\frac{Hw}{|v|})^2)), \tag{5.49}$$

for values of x satisfy (5.47), and we find $\mathbb{S}(x) = 0$ for all other values of x.

Kernels of compact support like the one derived here will be generic in realistic spotting models.

5.4.4 A family of 'fat-tailed' kernels

Let us consider again the ignition law presented in the introduction to the previous subsection, in the case where $\underline{m} \to 0$ (see Equation (5.42)). Then any firebrand landing on a location which is not burning will instantly generate a fire. We again have constant w and v, and further we will suppose that no mass is lost during transport corresponding to the burning law C0 with zero rate of combustion (the transport process being assumed very rapid).

Let's assume that the firebrand vertical launching distribution $\phi(z, m)$ satisfies the assumption (L3), so that

$$\phi(z, m) = \mathbb{Z}(z)\ \mu(m). \tag{5.50}$$

This says the lofting heights z are independent of the masses m. We can choose the mass distribution $\mu(m)$ in accordance with experiments such as in the experiments by Manzello [53], or out of mathematical curiosity we could consider any other probability distribution.

What is most important is to assume that $\mathbb{Z}(z)$ is not exponentially bounded,

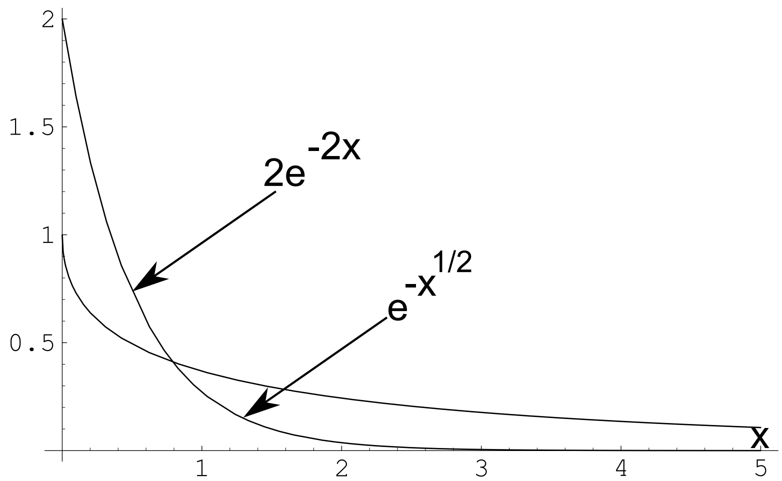

Figure 5.11: A comparison of the exponentially bounded kernel $2e^{-2x}$ versus the exponentially unbounded kernel $e^{-x^{1/2}}$. We see that there is more weight in the 'tail' of the unbounded kernel.

in order to obtain a fat-tailed kernel. For example, one could assume:

$$\mathbb{Z}(z) = e^{-z^{\beta}}, \tag{5.51}$$

for $\beta \in (0,1)$. This kernel decays sub-exponentially, and has been shown in integro-difference models equations to give rise to accelerating propagation of the corresponding solution in space [47]. Physically this could correspond to extreme spotting conditions like in the presence of fire whirls. A comparison of an exponentially bounded kernel versus kernels of the form (5.51) is given in Figure 5.11.

From Equation (5.31), with the form (5.51) appearing in the landed mass distribution $M(x)$, we find that for a release of N firebrands is:

$$\begin{aligned} M(x) &= N \int_0^{\bar{m}} m\ \mathbb{Z}(|v|\frac{x}{w})\ \mu(m)\ dm \\ &= N \int_0^{\bar{m}} m\ e^{-(|v|\frac{x}{w})^{\beta}}\ \mu(m)\ dm \\ &= e^{-(|v|\frac{x}{w})^{\beta}}\ N \int_0^{\bar{m}} m\ \mu(m)\ dm \\ &:= he^{-(|v|\frac{x}{w})^{\beta}}, \end{aligned} \tag{5.52}$$

where $h > 0$ is the total landed mass at x, namely

$$h := N \int_0^{\bar{m}} m \; \mu(m) \; dm < \infty. \tag{5.53}$$

Since we are assuming instant ignition, the spotting distribution is the same as the landed mass distribution. Referring to (5.52), we can then write the spotting kernel in this case:

$$\mathbb{S}(x) = he^{-(\frac{|v|x}{w})^\beta}. \tag{5.54}$$

Of course, this whole procedure can be generalized. If instead of the kernel (5.51) we use an arbitrary kernel $\mathbb{Z}(z)$, fat-failed or not, repeating the steps leading to (5.54), we obtain the spotting distribution:

$$\mathbb{S}(x) = h\mathbb{Z}(|v| \; \frac{x}{w}). \tag{5.55}$$

We can also extend the latter formula to include our other combustion models, by altering h defined in (5.53) to read

$$h := N \int_0^{\bar{m}} m \; \mu \left(\mathcal{C}^{-1}(m, \frac{x}{w}) \right) \; dm, \tag{5.56}$$

however the resulting kernel (5.55) will now have compact support, since we define $\mathcal{C}^{-1}(m, \frac{x}{w})$ only for values of x where $\mathcal{C}^{-1}(m, \frac{x}{w}) \geq 0$.

5.5 Extending the delayed-(iPDE) model derived in Chapter 2

Recall the delayed integro-partial differential equation model introduced in Chapter 2. We defined the landed mass distribution $M(x-y)$ as usual by:

$$M(x-y) = N \int_0^{\overline{m}} m \; \phi(|v|t^*(x-y), \mathcal{C}^{-1}(m, t^*(x-y)))dm. \tag{5.57}$$

And then defined the spotting redistribution kernel in terms of the formula

(5.57):

$$\mathbb{S}(x-y) = E[M(x-y)]. \tag{5.58}$$

In the expression (5.57) we have a mass $M(x-y)$. This mass is found by tracing back in time, starting from the ground, using the inverse combustion operator, to find the total mass which was launched to height $|v|t^*(x-y)$ at time $t - t^*(x-y)$. Clearly this total mass is eventually decreasing as we increase the magnitude of the y variable, since the probability of finding firebrands eventually decreases with increasing height.

Since we are taking ignition to be instantaneous relative to the fire's overall progress, and we are only considering models where the spatial trajectories of firebrands do not cross, we can extend our time-delayed iPDE model to include two different landing times, for the power-law profile, and the logarithmic profile (5.24). This gives us two new families of models, each corresponding to a different landing time model for $t^*(x-y)$:

$$\begin{aligned} \frac{\partial u(x,t)}{\partial t} &= D\frac{\partial^2}{\partial x^2}(u(x,t)) + f(u(x,t)) \\ \int_0^\infty & \mathbb{S}(x-y)\; u(x-y, t-t^*(x-y))\; dy, \end{aligned} \tag{5.59}$$

This is a natural extension of our delayed i-PDE model from Chapter 2, since (5.59) reduces to the equation derived there when w and v are constant. Models where the time delays have such complicated expressions will be very difficult to treat analytically, but numerical simulations of (5.59) with the new landing times discovered in this section should provide more realistic simulation results.

5.6 The spotting distribution and spotfire breaching

The formulae for the spotting distributions $\mathbb{S}(x)$ obtained in this section were obtained from an *impulse release* of firebrands at $x = 0$ and at $t = 0$. One can imagine the situation in which a large front reaches an impasse to local spread at $x = 0$, and then one wants to know whether the fire will spot across the impasse. In this section, we limited ourselves to the case of a homogeneous medium, which could be relevant for spread in a relatively flat, densely canopied environment, as in large coniferous industrial plantations.

The spotting distributions obtained in this chapter can then provide an estimate, depending on the downwind location x, of the probability that a spotfire ignition will occur at x, namely $\mathbb{S}(x) \in [0, 1]$.

Considering Example 1 from this chapter, in the case where the threshold mass $\underline{m} = 1$, we see in Figure 5.6 that spotting can occur up to 200 metres downwind of the firebreak. Hence, if the obstacle to local spread is less than 200 metres in length, it is almost certain that a spotfire will be ignited downwind, sometime shortly after the initial release. Further, we find a non-zero probability up to about 200 metres that a spotfire event will take place at a given location. It is important to note how increasing the threshold mass leads to a decrease in the spotting distribution's magnitude.

5.7 Chapter summary

In this chapter, we began by examining a specific case of the asymptotic landing distribution, starting from a very simple vertical launch distribution, and illustrated the effect of varying the windspeed, falling speed, or combustion rate. We then showed how the asymptotic landing distribution can be used to obtain the spotting distribution, by employing the ignition operator $E[m]$ introduced in Chapter 2. The general formula obtained reads:

$$S(x) = E[N \int_0^{\overline{m}} m\phi(H + |v|t^*(x), \mathcal{C}^{-1}(m, t^*(x)))\, dm].$$

This formula is somewhat remarkable, in that we are free to explore an enormous number of possible spotting kernels. However, given the limited knowledge of many of the spotting subprocesses at the moment, it is difficult to decide which is the most realistic model. In particular, the sparcity of data from real fires currently makes this an impossible task, but in the future it may be possible to use satellite data, or infrared imaging of real fires to determine real spotting distributions.

We chose three different 'averaged' spotting distributions for each of the three ignition models, and their differences can be seen by examining Figure 5.6, Figure 5.8, and Figure 5.10. The purpose of this comparison is to illustrate the very distinct differences between the ignition types, rather than to achieve maximum physical realism. Prior to the commencement of this thesis, very little was known about threshold masses for various fuel types. Experimental work like that in [37] should eventually lead to our ability to choose a best ignition model, and to fit it to data so that our models could be applicable in real world application.

At the macroscopic scale, the rapid variations in spread conditions within a typical 'grid' cell, which could for example be 100 square metres in area [89], must be homogenized so as to produce a threshold mass for the entire cell. This is a challenging problem, both from a modelling as well as from an experimental perspective. The Fire Behaviour Prediction system [40] contains predictive models for weather and other spread factors, based on experiment, and could be of use in this homogenization procedure.

In this chapter we showed some realistic and some extreme examples of the spotting distribution. As we discussed in Chapter 4, there is an impossible number of permutations of the submodels to treat in this thesis. One result of importance is how compactly supported, or 'fat'-tailed spotting distributions can be obtained; in fact, all manners of distribution. The scarcity of data on the spotting distribution from real world fires makes the choice of the most physically correct distribution impossible at this stage.

Our physically realistic but simple models show, as in Figure 5.8, spotting distributions that we might expect to occur in the field. The extreme cases discussed in section 5.4.4 allow for fat-tailed distributions, which we will further analyze in Chapters 6 and 7. In fact, in Chapter 6 we will show analytically in the context of our i-PDE models, that such fat-tailed kernels can accelerate a fire front, and we will observe this behaviour through numerical examples in Chapter 7.

Chapter 6

Analytic investigation of solutions to the i-PDE models: rates of spread and acceleration

6.1 Chapter Introduction

Having derived a host of spotting kernels $\mathbb{S}(x)$ in Chapter 5, in this chapter we will revisit our i-PDE fire probability spread model derived in Chapter 2. Recall that $u(x,t)$ denotes the probability density for there to be a fire spotting at location x at time t, while $v(x,t)$ denotes the total fuel loading fraction at location x at time t.

We will focus on the case where $v = 1$ everywhere, assume the medium is homogeneous and isotropic, and ignore time delays in the integral term, which as explained in Chapter 2 results in a model:

$$\frac{\partial u(x,t)}{\partial t} = D\frac{\partial^2 u(x,t)}{\partial x^2} + \int_0^\infty u(x-y,t)\ \mathbb{S}(y)\ dy + f(u(x,t)). \tag{6.1}$$

Also of interest is the spotting-dominated case, where we set $D = 0$ in the above equation.We will be interested in problems of existence and uniqueness, as well as spreading speeds for initial value problems with compact support, and travelling wave solutions to initial value problems. Recall that we are modelling the spread of a wildfire front in a one-spatial dimensional habitat.

In Sections 6.2 and 6.3, we employ results from Appendix B on semigroups to establish well-posedness of the initial value problem for (6.1), first on a bounded domain, and then on an unbounded domain.

In Section 6.4 we present a brief history of modelling of biological invasions, and introduce some important concepts which we elaborate on in the rest of the chapter, in which we focus on the spotting dominated case. In particular, in Section 6.5 we discuss travelling wave solutions, in Section 6.6 we discuss spreading speeds, and in Section 6.7 we show how to obtain solutions which accelerate.

In each section we deal with possibly different assumptions, which we try to make as clear as possible without disrupting the flow.

6.2 Existence and uniqueness of solutions in $L^2(\Omega)$, for bounded $\Omega \subset \mathbb{R}$

In this first section we will consider well-posedness for Equation (6.1), on a smooth bounded subset $\Omega \subset \mathbb{R}^n$, with Dirichlet boundary conditions:

$$u(x,t) = 0, \quad x \in \partial\Omega, \quad t \in [0,T]. \tag{6.2}$$

And with initial conditions $u_0 \in L^2(\Omega)$. The case of Neumann or periodic boundary conditions are similar, but must be treated separately.

We recall Theorem B.5 from Appendix B, which gave us existence and uniqueness of a solution $u \in C^0(0,T; L^2(\Omega))$ for $T > 0$, and continuity of the map $u_0 \to u(t)$ in $L^2(\Omega)$. We will assume the hypotheses of (B.5) hold in what follows.

The existence, uniqueness, and continuous dependence on initial conditions for this problem, established in Appendix B, allow us to define solution operators $\psi(t)$ for the Dirichlet problem, which forms a C_0 semigroup of bounded linear operators on $L^2(\Omega)$. In particular, the solution $u(x,t;u_0) := \psi(t)[u_0](x)$.

To use the Bounded Perturbation Theorem (Appendix B, Theorem B.4), we must discuss the generator A of the semigroup $\psi(t)$, which happens to be:

$$Af := f_{xx}, \quad D(A) := \{f \in C^2(\Omega) \mid f(x) = 0, x \in \partial\Omega\}. \tag{6.3}$$

It can be shown ([32], E.g. 2.2.12) that A is the generator of a strongly continuous semigroup on $C_c^0(\Omega)$. Its maximal domain of definition $D(A)$ can be extended by the density of C_c^0 in L^2, so that A generates a C_0 semigroup on $L^2(\Omega)$.

Let us now recall spotting operator $\mathcal{S}$ from Chapter 2,

$$\begin{aligned}(\mathcal{S}u(t))(x) &:= \int_0^\infty \mathbb{S}(y)u(x-y,t)dy \\ &:= \mathbb{S} * u(t),\end{aligned} \tag{6.4}$$

where $\mathbb{S} * u(t)$ denotes the *convolution* of the kernel $\mathbb{S}(x)$ with the function $u(t)$ on $[0,\infty)$.

We will require that $\mathcal{S}$, equipped with Dirichlet boundary conditions, is bounded from $L^2(\Omega)$ into itself. A special case is if $\mathcal{S}$ a Hilbert-Schmidt operator, so that the kernel $\mathbb{S}(y)$ satisfies (B.2.31) from Appendix B. Alternatively, as stated in Appendix B, if $\mathcal{S}$ satisfies Holmgren's inequality (B.2.32), then it is bounded. It should be noted that many important integral operators, such as the Fourier transform or the Laplace transform, may fail to satisfy either of these inequalities, yet are bounded in L^2 nonetheless.

By the Bounded Perturbation Theorem, $\mathcal{S}+A$ is the generator of a C_0 semigroup $(T(t))_{t\geq 0}$. The maximal domain of definition is $D(A+\mathcal{S}) = D(A)$ [32].

We may then rewrite the i-PDE (6.1) in the abstract form:

$$\frac{du}{dt} = (A+\mathcal{S})u(t) + f(u(t)), \tag{6.5}$$

to which we can express the unique solution u in terms of the variation-of-constants formula [65]:

$$u(t) = T(t-s)u(s) + \int_s^t T(t-\tau)f(u(\tau))\, d\tau. \tag{6.6}$$

Strong continuity of the solution operators also implies continuity of the map $u_0 \to u(t)$ in $L^2(\Omega)$, so with the assumptions in this section the IBVP for (6.1) is well posed.

6.3 Existence and uniqueness of solutions in $L^2(\mathbb{R})$

We consider the model (6.1) on $\mathbb{R}$, by extending $\mathbb{S}$ to all of $\mathbb{R}$ by setting $\mathbb{S}(x) = 0$ if $x < 0$. We assume that $f \in L^2(\mathbb{R})$ is Lipschitz continuous, and further that the integral operator is a Hilbert-Schmidt operator (or at least bounded from $L^2 \to L^2$). As in the preceding section, we can then use the Bounded Perturbation theorem twice, for each of the bounded terms $f(u)$ and $\mathbb{S} * u$, so as to obtain another strongly continuous semigroup which solves the IVP for (6.1), since we already know that the heat semigroup forms a strongly continuous semigroup (B.2.58) on $\mathbb{L}^2(\mathbb{R})$, by Theorem B.6 in Appendix B.

We thus have established existence, uniqueness, and continuous dependence on initial conditions for the IVP for (6.1), in the case of an unbounded domain. We will now proceed to examine the spotting-dominated case, where we neglect the effect of diffusion.

6.4 The spotting-dominated case: Some background and notation

Recall that the spotting-dominated case is a special case of Equation (6.1),

$$\frac{\partial u(x,t)}{\partial t} = \left(\mathbb{S} * u(t)\right)(x) + f(u(x,t)), \tag{6.7}$$

where the convolution term $\left(\mathbb{S} * u(t)\right)(x)$ was defined in Equation (6.4), on the domain $x \in [0, \infty)$. In the remainder we will assume f is at least Lipschitz continuous, and the convolution defines a regular Borel measure, for Borel measurable functions $u(t)$ on $[0, \infty)$.

In Chapter 7 we divide the possibly nonlinear kinetics term f into a negative contribution due to to heat loss, and a positive contribution due to the availability of fuel,

$$f(u(x,t)) = \tilde{c}(u(x,t)) - du(x,t), \tag{6.8}$$

so that an alternative to Equation (6.7) reads:

$$\frac{\partial u(x,t)}{\partial t} = \left(\mathbb{S} * u(t)\right)(x) + \tilde{c}(u(x,t)) - du(x,t), \tag{6.9}$$

where $\tilde{c}$ is a Lipschitz-continuous and monostable function of u, and $d > 0$ is constant.

The non-linear Equations (6.7) and (6.9), which differ only in their description of the kinetics term, and even systems of such equations, have been studied for some time in epidemiology, invasion ecology and combustion modelling, amongst other subjects. Such models go beyond Fisher's PDE, allowing for a finer description of the 'tail' of the spotting distribution, and the analysis of their invasion properties ([35],[45]) go far beyond those outlined in the Introduction.

The first spreading results for an i-PDE system, resulted from the study of a model for an epidemic invasion, and presented in Kendall [43], was an investigation of an extension of the classic epidemic model due to Kermack and McKendrick [44]. This paper utilized a diffusion approximation to the right hand side of (6.7), and in this approximation Kendall was able to show that the possible velocities had a lower bound c_0, and hence the velocity spectrum for such epidemics is $[c_0, \infty)$.

Mollison then proceeded to investigate the 3-component i-PDE system of Kendall directly, and Mollison showed that for an exponentially bounded, non-negative, probability kernel the diffusion approximation due to Kendall works well [60]. Mollison did this by reducing the study to that of a single equation.

Definition: A *travelling wave* solution with profile $\Gamma(z)$ to Equation (6.7), is a solution $u(x,t)$ which depends only on the variable $z = x - ct$, i.e. $u(x,t) = \Gamma(x - ct)$, where $c \geq 0$ is the *wavespeed*. Such solutions simply propagate to the right with time, without changing their shape. Typically we require $\lim_{z\to\infty} \Gamma(z) = 0$, while $\lim_{z\to-\infty} \Gamma(z) = \sigma$, where $\sigma > 0$.

Mollison constructed travelling wave solutions for all speeds greater than or equal to a minimum speed c_0, for exponentially bounded kernels [61]. For exponentially unbounded kernels, Mollison explained how no finite bound can be placed on the speed of propagation of such waves [60].

Definition: We define an *exponentially unbounded kernel*, to be a kernel S which decays super-exponentially as $x \to \infty$, so that

$$\forall\, \eta > 0, \;\; \exists\, x_\eta \in \mathbb{R}, \;\; \mathbb{S}(x) \geq e^{-\eta x}, \;\; x \in [x_\eta, \infty) \tag{6.10}$$

The opposite case is that of an exponentially bounded kernel, where there exists $\eta > 0$ such that:

$$\int_{\mathbb{R}} \mathbb{S}(x)\, e^{\eta|x|}\, dx < \infty, \tag{6.11}$$

for a kernel defined on all of $\mathbb{R}$.

The value $\sigma > 0$ described in Definition 6.4 is often the spatially homogeneous steady state, i.e. the long-time solution of the ODE $u_t = f(u)$ for $u_0 \geq 0$. The problem of constructing a connection between $u = 0$ and $u = \sigma$ depends on the model one deals with, and the initial conditions provided.

Another relevant parameter in mathematical models of invasion is the asymptotic speed of spread c_*, or simply the spreading speed, a concept introduced by Aronson and Weinberger in the context of reaction-diffusion equations [10]. The concept was then applied by Aronson to Kendall's model [9], given certain assumptions on the kernel and kinetics function. The techniques employed in [9] re-appear as part of the construction of spreading speeds for many subsequent models.

Definition: Suppose $u(x,t)$ is the unique continuous and bounded solution to (6.7) in $L^\infty(\mathbb{R})$. Suppose further that $u(x,0) := u_0(x)$ is compactly supported. We say that c is a spreading speed of an invasion [9], governed by Equation (6.7), if:

$$\liminf_{t\to\infty, |x|>c\,t} u(x,t) = 0, \tag{6.12}$$

and

$$\limsup_{t\to\infty, |x|\leq c\,t} u(x,t) > 0, \tag{6.13}$$

In words, the first item in the latter definition says if you move faster than speed c, you outrun the invasion, while if you move at any speed c', where $c_0 < c' < c$, the invasion overtakes you.

For the models studied by Kendall [43], both Diekmann [30] and Thieme [86] independently proved that the asymptotic speed of spread c_* corresponds to the minimum travelling wave speed c_0 found by Mollison. Weinberger extended these results to a finite-time recursion process, which has had much subsequent applications in the study of spreading speeds [92].

An assumption which appears frequently in these papers, and which we will employ in our study, is that there is a unique positive, stable fixed point for the kinetics f, captured in the following definition.

Definition: A kinetics term $f \in C^1([0,1], \mathbb{R})$ is *monostable* on $[0,1]$, if

$$f(0) = f(1) = 0, \quad f(s) > 0 \text{ for all } s \in (0,1), \quad f'(0) > 0. \tag{6.14}$$

6.5 Spotting dominated case: existence of travelling wave solutions

6.5.1 Some recent results on travelling waves

In this subsection we discuss some results concerning travelling wave solutions of $u_t = \widehat{\mathbb{S}} * u + f(u)$, where $\widehat{\mathbb{S}}$ defines a nonnegative, regular, probability Borel measure on $\mathbb{R}$.. We assume f is Lipschitz continuous and monostable on $[0,1]$ (unless otherwise specified).

Then as noted in Yagista [94], the function

$$G(u) := \widehat{\mathbb{S}} * u + f(u), \tag{6.15}$$

is Lipschitz-continuous on $L^\infty(\mathbb{R})$. By the usual well-posedness theory of ordinary differential equations [65], the Equation:

$$u_t = \widehat{\mathbb{S}} * u + f(u) \tag{6.16}$$

generates a semiflow on $\mathbb{L}^\infty(\mathbb{R})$.

Given these assumptions, Schumacher determined that there is a minimal speed c_* of travelling wave solutions to (6.16), such that travelling wave solutions with speeds $c \geq c_*$ exist, provided the KPP condition:

$$f(u) \leq f'(0)u, \tag{6.17}$$

and some further conditions hold ([77], [78]).

More recently, Yagista has generalized these results to discuss existence and nonexistence of travelling waves as follows [94]:

Theorem 6.1: *([94], Theorem 1) Suppose there exists a positive constant $\lambda > 0$ such that*

$$\int_{-\infty}^{\infty} \widehat{\mathbb{S}}(y)\, e^{\lambda y}\, dy < \infty. \tag{6.18}$$

Then there exists a constant c_* such that Equation (6.16) has a traveling wave solution with monotone profile and speed $c \geq c_*$. There are no traveling wave solutions when $c < c_*$.

We notice that the integral appearing in (6.18) is the moment-generating function of the density $\widehat{\mathbb{S}}$, so by requiring it to exist for a single value of $\lambda > 0$, we are placing weak constraints on the kernel $\widehat{\mathbb{S}}$, as well as weaker conditions on the non-linearity f relative to the monostable-KPP assumptions, in order to guarantee the existence of monotone travelling waves. There is also no symmetry assumption on the kernel, which is assumed in almost all such models in the literature.

6.5.2 Travelling wave solutions for our model (6.9)

We would like to connect our model (6.9) to the results in the preceding subsection. To do so, we first extend our nonnegative kernel $\mathbb{S}$ from $[0, \infty)$ to all of $\mathbb{R}$, by defining

$$\tilde{\mathbb{S}}(\chi) := \begin{cases} \mathbb{S}(x), & x \geq 0; \\ 0, & x < 0 \end{cases}, \tag{6.19}$$

where in what follows we will drop the tilde $\tilde{\mathbb{S}}$, and instead write $\mathbb{S}$, where it is understood that $\mathbb{S}$ is the fully supported kernel in (6.19).

We suppose that our kernel $\mathbb{S}$ integrates to a finite positive value s_0,

$$\int_{\mathbb{R}} \mathbb{S}(x)\, dx = s_0. \tag{6.20}$$

We introduce a scaling in space:

$$\chi = s_0^{-1} x. \tag{6.21}$$

Employing our change of variables (6.21), we obtain:

$$\begin{aligned}\int_{\mathbb{R}} \mathbb{S}(x)\, dx &= \int_{\mathbb{R}} \mathbb{S}(s_0\chi) s_0 \, d\chi \\ &= s_0,\end{aligned}$$

from which we define yet another kernel

$$\bar{\mathbb{S}}(\chi) := \mathbb{S}(s_0 \chi), \tag{6.22}$$

with the property that it integrates to one:

$$\int_{\mathbb{R}} \bar{\mathbb{S}}(\chi)\, d\chi = 1. \tag{6.23}$$

Further, let's recall the function $f(u)$ in (6.9) reads:,

$$f(u) := \tilde{c}(u) - d\, u,$$

where $\tilde{c}(u)$ is assumed to be Lipschitz continuous and monostable on $[0, 1]$.

Then with our change of variables, the differential equation (6.9) becomes:

$$\frac{\partial u(\chi, t)}{\partial t} = (\bar{\mathbb{S}} * u(t))(\chi) + f(u(\chi, t)). \tag{6.24}$$

It is clear that $f(0) = 0$, and $f(1) = d$ since $\tilde{c}(1) = 0$, so the latter equation is not monostable on $[0, 1]$. The roots of f are $u = 0$, and the value $\gamma > 0$ where $\tilde{c}(\gamma) - d\,\gamma = 0$, which we assume to exist.

Let us next introduce a new dependent variable y,

$$y(\chi, t) = \frac{1}{\gamma}\, u(\chi, t), \tag{6.25}$$

The differential equation (6.24) becomes

$$\frac{\partial y(\chi, t)}{\partial t} = (\bar{\mathbb{S}} * y(t))(\chi) + \frac{1}{\gamma} f(\gamma\, y(\chi, t)). \tag{6.26}$$

For simplicity of notation, we set

$$g(y) := \frac{1}{\gamma} \; + f(\gamma\, y), \tag{6.27}$$

so that our original equation (6.9), following from (6.24), becomes:

$$\frac{\partial y(\chi, t)}{\partial t} = (\bar{\mathbb{S}} * y(t))(\chi) + g(y(\chi, t)). \tag{6.28}$$

Lemma 6.1: *Assume that there is a constant $\lambda > 0$ such that (6.18) holds for our kernel $\bar{\mathbb{S}}$, where $\bar{\mathbb{S}}$ is a probability measure, and $g(y)$ is Lipschitz continuous and monostable on $[0, 1]$. Then Theorem 6.1 implies that there exists some constant c_*, such that there exist monotone travelling wave solutions $y(\chi, t)$ to Equation (6.28), for speeds $c \geq c_*$.*

Proof. Notice $\bar{\mathbb{S}}$ is nonnegative and integrates to one, and the function g defined in (6.27) Lipschitz continuous, and monostable on $[0, 1]$. By assumption the technical condition (6.18) holds for some $\lambda > 0$. Then we are guaranteed the existence of a monotone travelling wave solution $y(\chi, t)$ to (6.28), for all $c \geq c_*$, by Theorem 6.1. □

Thus for our spotting model (6.9), we are able to establish the existence of monotone travelling waves:

Theorem 6.2: *Suppose the hypotheses of Lemma 6.1 hold. Then there exists a constant $c_*^{(1)}$ such that Equation (6.9) has a monotone travelling wave solution, for all speeds $c \geq c_*^{(1)}$. The amplitude of the travelling wave solution for (6.9) is γ times the amplitude of the corresponding travelling wave solution for (6.28). Further, the travelling wave solution for (6.9) travels at speed $s_0\, c$, relative to the corresponding travelling wave speed c for (6.28).*

Proof. According to Lemma 6.1, Equation (6.28) has a unique monotone travelling wave solution $y(\chi, t)$, for each wave speed $c \geq c_*$, for some constant $c_* > 0$. Of course, Equation (6.28) is related to (6.9) by the scaling of variables introduced in this subsection. Let us denote this solution $u(\chi, t)$. Let us now invert our transformations determined in this chapter, to obtain the solution $u(x,t)$ to (6.9):

$$u(s_0\, x, t) = \gamma y(\chi, t). \tag{6.29}$$

Hence we see that the solution u to (6.9) is a scaled version of the solution (6.28). So necessarily the solution $u(x,t)$ describes a monotone travelling wave. The amplitude of $u(\chi,t)$ is γ times the magnitude of the travelling wave $y(\chi,t)$.

However, in terms of our original variable x, we have $u(x,t) = u(s_0\chi, t)$. So if the travelling wave $y(\chi,t)$ travels at speed c, the travelling wave for $u(x,t)$ moves at speed $s_0\, c$. This can be seen by approximating the wavespeed for $y(\chi,t)$ as $c \approx \frac{\Delta\chi}{\Delta t} = s_0^{-1}\frac{\Delta x}{\Delta t}$. □

6.6 Spotting dominated case: spreading speeds and acceleration

6.6.1 Spreading speeds in the linearized case

In this subsection, we will explore spreading speeds for our model (6.7). We will follow a method which is old in the literature, probably due to Mollison [61]. In this method, we will suppose that the leading edge of the wave is linearly determined. To explore this, we consider a linearized version of the nonlinear model (6.7),

$$u_t = ru + \bar{\mathbb{S}} * u(t), \tag{6.30}$$

where $r := f'(0) > 0$ is the linearization of $f(u)$ at $u = 0$, and $\bar{\mathbb{S}}$ is as defined in the preceding section, in Equation (6.26). Recall that $\bar{\mathbb{S}}$ is the normalized extension of our one-sided kernel $\mathbb{S}$ from $[0,\infty)$ to all of $\mathbb{R}$.

We assume a solution of the form:

$$u(x,t) = \Gamma(x - ct), \tag{6.31}$$

where c is the wavespeed. Further, we assume a wave profile Γ of the form:

$$\Gamma(z) := e^{-\lambda z}. \tag{6.32}$$

We also impose the requirement:

$$\lim_{z\to\infty} \Gamma(z) = 0. \tag{6.33}$$

Inserting the forms (6.31),(6.32) for the solution into the equation $u_t = ru + \hat{\mathbb{S}} * u(t)$, we obtain:

$$c\lambda e^{-\lambda z} = re^{-\lambda z} + \int_{-\infty}^{\infty} \bar{\mathbb{S}}(y) e^{\lambda[(x-ct)-y]}\, dy, \tag{6.34}$$

which leads us to the formula:

$$c\lambda = r + \int_{-\infty}^{\infty} \bar{\mathbb{S}}(y) e^{\lambda y}\, dy. \tag{6.35}$$

We define the moment generating function $\mu_0(\lambda)$ for a given kernel $\bar{\mathbb{S}}$,

$$\mu_0(\lambda) := \int_{-\infty}^{\infty} \bar{\mathbb{S}}(y) e^{\lambda y}\, dy. \tag{6.36}$$

Comparing the formulas (6.35) and (6.36), we find an expression for a candidate for the invasion speed c, in the exponentially bounded case:

$$c = \frac{r + \mu_0(\lambda)}{\lambda}. \tag{6.37}$$

Now, from the preceding expression, we define the following quantities, which will define the right and left-traveling wavespeeds respectively:

$$\begin{aligned} c^+ &:= \inf_{\lambda>0} \frac{r + \mu_0(\lambda)}{\lambda} \\ c^- &:= \inf_{\lambda>0} \frac{r + \mu_0(-\lambda)}{\lambda}, \end{aligned} \tag{6.38}$$

The latter formulae (6.38) were derived heuristically, by examining a particular form for the leading edge of a traveling wave. In order to justify that they are in fact the spreading speeds for the nonlinear model, we will appeal to the theory for spreading speeds, for asymmetric dispersal kernels, developed in Jin and Lewis [41].

6.6.2 Recent results on spreading speeds and accelerating solutions

Jin and Lewis [41] consider a model which is very similar to our own, namely

$$u_t = u(x,t)g(t,u(x,t)) - a(t)u(x,t) + a(t)\int_\Omega k(t,x-y)\ u(y,t)\ dy, \quad (6.39)$$

where each of g, a, and k are positive and ω-periodic in t [41].

In order to obtain spreading speeds, Jin and Lewis make the following assumptions about Equation (6.39): (H1):

- $g \in C(\mathbb{R}_+^2, \mathbb{R})$, and $g_u(t,u) < 0$ for all $(t,u) \in \mathbb{R}_+^2$. This says the per capita combustion rate decreases with an increase in fire probability u.
- There is a $\hat{u} > 0$ such that $g(t,\hat{u}) \leq 0$, so that the growth rate is negative if the population exceeds $\hat{u}$.
- $\int_0^\omega g(t,0)\ dt > 0$.
- The transfer rate $a(t) > 0$, and $a(t)$ is continuous.
- There exists a constant $L > 0$ such that

$$|u_1 g(t,u_1) - a(t)u_1 - (u_2 g(t,u_2) - a(t)u_2)| \leq L|u_1 - u_2|, \quad (6.40)$$

  for all u_1,$u_2 \in [0,\hat{u}] := W$. This implies $ug(t,u) - du$ is uniformly Lipschitz continuous in u on W.

(H2):

- $k(t,x) \geq 0$, and $\int_{\mathbb{R}} k(t,x)dx = 1$, for all $t \geq 0$.
- $k(t,x)$ is continuous in $t \in \mathbb{R}$ uniformly in x on any bounded interval of $\mathbb{R}$.
- The moment generating function, defined in (6.36)

$$\mu_0(t,\lambda) := \int_{\mathbb{R}} k(t,y)e^{\lambda y}dy,$$

exists for all $\lambda \in (-\Delta_-, \Delta_+)$ and $t \geq 0$, with $M(t_0, -\Delta_-) = \infty$ and $M(t_1, \Delta_+) = \infty$ for some t_0,$t_1 \geq 0$, where $\Delta_\pm$ are positive and may be infinity. In the case where $\Delta_\pm = \infty$, the dispersal kernel $k(t, x)$ has exponentially bounded tails, and the tails are uniformly bounded for all $t \geq 0$.

The spreading speeds are then obtained as follows, in terms of the Poincare map Q_ω, which maps the solution at time t into the solution at time $t+\omega$, i.e. one period later from time t.

Proposition 6.1: *(Jin and Lewis [41], Proposition 2.1) Assume that (H1) and (H2) hold. Let Q_ω be the Poincare map of Equation (6.39). The spreading speeds of Q_ω in the downstream (c_ω^+) and upstream (c_ω^-) directions are, respectively,*

$$c_\omega^+ = \inf_{0<\alpha<\Delta_+} \frac{\int_0^\omega (g(s,0) - a(s))\, ds + \int_0^\omega a(s) \int_{\mathbb{R}} k(s,y) e^{\alpha y}\, dy\, ds}{\alpha}, \tag{6.41}$$

and

$$c_\omega^- = \inf_{0<\alpha<\Delta_-} \frac{\int_0^\omega (g(s,0) - a(s))\, ds + \int_0^\omega a(s) \int_{\mathbb{R}} k(s,y) e^{-\alpha y}\, dy\, ds}{\alpha}, \tag{6.42}$$

Now let

$$c^+ = \frac{c_\omega^+}{\omega}, \tag{6.43}$$

and

$$c^- = \frac{c_\omega^-}{\omega}. \tag{6.44}$$

Theorem 6.3: *(Remark following, and established by, Theorem 2.1 in Jin and Lewis [41]): c^+ and c^- are the spreading speeds of solutions to (6.39), in the downstream and upstream directions, respectively.*

Since constant functions are ω-periodic for any $\omega \in \mathbb{R}$, the results which apply for (6.39) also apply in the case where g, a, and k do not depend on time, as in our models (6.7) or (6.9). Indeed, this is described in Section 4.1 from Jin and Lewis, where they deal explicitly with the autonomous case, where g, a, and k are time-independent, which results in an equation of the form [41]:

$$u_t(x,t) = u(t,x)\ f(u(t,x)) - du(t,x) + d \int_{\mathbb{R}} u(y,t)\ k(x-y)\, dy. \tag{6.45}$$

As stated in Section 4.1 from Jin and Lewis [41], it follows from Theorem 6.3, that we have the following Theorem:

Theorem 6.4: *Suppose f, d, and k in (6.45) satisfy the corresponding conditions for g, a, and k in (H1) and (H2), then the spreading speeds for (6.45) in the upstream and downstream directions are given by*

$$c_0^+ = \inf_{0<\alpha<\Delta_+} \frac{f(0) - d + d\int_{\mathbb{R}} k(y)\, e^{\alpha y}\, dy}{\alpha}, \tag{6.46}$$

and

$$c_0^- = \inf_{0<\alpha<\Delta_-} \frac{f(0) - d + d\int_{\mathbb{R}} k(y)\, e^{-\alpha y}\, dy}{\alpha}. \tag{6.47}$$

The reader will notice that the latter spreading speeds are consistent with the formulae (6.38). In the next section we will apply the formulae (6.46) and (6.47) to our model (6.9) to establish results concerning spreading speeds.

To describe accelerating solutions, we employ the following Theorem:

Theorem 6.5: *(Jin and Lewis [41], Theorem 2.4) Consider the model (6.39), and the spreading speeds c^+ and c^-, given in (6.43) and (6.44), and established in Theorem 6.3.*

Then the spreading speed c^+ (c^-) in the downstream (upstream) direction of the solution to (6.39), is infinite if and only if $\int_{\mathbb{R}} k(x)e^{\lambda x}dx = \infty$ for all positive λ (negative λ).

The latter theorem tells us that if the spotting kernel does not possess a moment generating function, then there is no upper bound on the spreading speeds. Numerical investigation in Chapter 7 for analogous models suggests that such solutions have a leading edge which accelerates.

6.6.3 Computing spreading speeds, or acceleration for our model (6.9)

Let us recall our model (6.9),

$$\frac{\partial u(x,t)}{\partial t} = \tilde{c}(u(x,t)) - d\, u + \int_0^\infty \mathbb{S}(y)\, u(x-y,t)\, dy.$$

In this subsection, we will make use of the following assumptions for the kernel $\mathbb{S}$, denoted (S1):

- The kernel $\mathbb{S}$ is nonnegative and bounded,
- The kernel $\mathbb{S}$ is nonzero only on some subset of $[0, \infty)$, because we assume spotting occurs only from left to right.
- The kernel is exponentially bounded, i.e. there is some $\tilde{\eta} > 0$ such that

$$\int_0^\infty \mathbb{S}(x) e^{\tilde{\eta}\, x}\, dx < \infty. \tag{6.48}$$

The previous subsection modelled movement in a stream, which is analogous to our wind-driven flow. What we called the upstream spreading speed, is here the upwind spreading speed, and the downstream spreading speed is called the downwind spreading speed. We expect the upwind spreading speed to be zero, while the downwind spreading speed should be nonzero.

Comparing our model to (6.45), we see that the kernel k appearing there plays an analogous role to our spotting kernel $\mathbb{S}$ appearing in (6.9). However, the results in Theorem 6.3 and Theorem 6.5 are for kernels defined on all of $\mathbb{R}$. We define the extension of our kernel $\mathbb{S}(y)$ to all of $\mathbb{R}$, by requiring $\mathbb{S}(y)$ to be zero for $y \leq 0$, as done before. We will continue to refer to this extended kernel using the same notation, namely $\mathbb{S}$.

We thus rewrite (6.9) in our usual notation,

$$\frac{\partial u(x,t)}{\partial t} = \tilde{c}(u(x,t)) - d\, u(x,t) + (\mathbb{S}(y) * u(t))(x),$$

where it is understood that $x \in \mathbb{R}$.

Now, consider that $\mathbb{S}(y) = d\, \frac{\mathbb{S}(y)}{d}$, which allows us to define a new kernel

$$\mathbb{S}_1(y) := \frac{\mathbb{S}(y)}{d}. \tag{6.49}$$

Examining the conditions (H2) from the preceding subsection, our spotting kernel $\mathbb{S}$ is nonnegative, but does not necessarily integrate to one. We will normalize the kernel $\mathbb{S}_1$.

We suppose that our kernel $\mathbb{S}_1$ integrates to the finite value s_1,

$$\int_{\mathbb{R}} \mathbb{S}_1(x)\, dx = s_1. \tag{6.50}$$

Next we introduce a scaling in space:

$$\chi = s_1^{-1} x, \tag{6.51}$$

such that

$$\bar{\mathbb{S}_1}(\chi) := \mathbb{S}_1(s_1 \chi), \tag{6.52}$$

integrates to one.

Since we assume $\mathbb{S}$ is nonnegative, it follows $\bar{\mathbb{S}_1}$ is also nonnegative. Since we assume that $\mathbb{S}$ is exponentially bounded, so is $\bar{\mathbb{S}_1}$. Our kernel does not depend on time t.

Further, the moment generating function of $\bar{\mathbb{S}_1}$ is defined analogously to (6.36),

$$\mu_0(\lambda) = \int_{\mathbb{R}} e^{\lambda\chi}\, \bar{\mathbb{S}_1}(\chi)\, d\chi. \tag{6.53}$$

Since our kernel $\bar{\mathbb{S}_1}$ is zero for all $y \leq 0$, we can rewrite the moment generating function μ_1 in (6.53) as

$$\mu_1(\lambda) = \int_0^\infty e^{\lambda\chi}\, \bar{\mathbb{S}_1}(\chi) d\chi. \tag{6.54}$$

It is natural to suppose that $\tilde{c}(0) = 0$, since if there is no fire, there is no combustion. Hence we can define a new function, $\hat{f}(u)$, which describes the per capita growth rate of the expected fire probability, so that:

$$\tilde{c}(u(\chi, t)) := u(\chi, t)\hat{f}(u(\chi, t)). \tag{6.55}$$

In terms of this new expression for $\tilde{c}$, we may rewrite our Equation (6.9):

$$\frac{\partial u(\chi, t)}{\partial t} = u(\chi, t)\hat{f}(u(\chi, t)) - d\, u(\chi, t) + d\, (\bar{\mathbb{S}_1} * u(t))(\chi). \tag{6.56}$$

The function $\hat{f}(u)$ defined in (6.55) is analogous to the function $f(u)$ appearing in (6.45), in that both are per capita growth rates. Let's examine the assumptions from (H1), which must be met, adapted to our autonomous situation.

We call the following group of assumptions (J1):

- $\hat{f} \in C(\mathbb{R})$, and $\hat{f}'(u) < 0$ for all $u \in \mathbb{R}_+$.
- There exists a threshold value $\hat{u} > 0$, such that $\hat{f}(u) \leq 0$, for all values of $u \geq \hat{u}$. This says once the fire probability reaches a threshold value, the per capita growth rate of fire probability is negative.
- We assume $\frac{\int_0^\omega \hat{f}(0)ds}{\omega} = \hat{f}(0) > 0$.
- The constant $d > 0$ (and constants are continuous).
- We assume that $G(u) := u\hat{f}(u) - d\,u$ is uniformly Lipschitz continuous, with respect to u, on $[0, \hat{u}]$.

Lemma 6.2: *If the assumptions (S1) on $\mathbb{S}$ presented in this subsection, as well as the assumptions in (J1) hold, then the spreading speeds for solutions to Equation (6.56) are given by:*

$$c_0^+ = \inf_{0<\lambda<\eta} \frac{\hat{f}(0) - d + d\int_0^\infty \bar{\mathbb{S}}_1(\chi)\, e^{\lambda\chi}\, d\chi}{\lambda}, \tag{6.57}$$

in the downwind direction (positive x), and in the upwind direction (negative x) by:

$$c_0^- = \inf_{0<\lambda<\infty} \frac{\hat{f}(0) - d + d\int_0^\infty \bar{\mathbb{S}}_1(\chi)\, e^{-\lambda\chi}\, d\chi}{\lambda}. \tag{6.58}$$

Proof. Our model (6.56) is completely analogous to the autonomous model by Jin and Lewis presented in (6.45). We will check to see that assumptions (H1) and (H2) are satisfied, so that we may use the spreading speed formulae (6.46) and (6.47), adapted to our model (6.56).

By assumption, our kernel $\bar{\mathbb{S}}_1$ is exponentially bounded, there exists $\eta > 0$ such that:

$$\mu_0(\eta) = \int_0^\infty \bar{\mathbb{S}}_1(\chi)\, e^{\eta\chi}\, d\chi < \infty, \tag{6.59}$$

which guarantees that $\mu_0(\lambda)$ exists at least for $\lambda \in [0, \eta)$ for the kernel $\bar{\mathbb{S}}_1$. We also know $\mu_0(\lambda) < \infty$ for each $\lambda < 0$, since again by the assumption of exponential boundedness we have

$$\mu_0(-|\lambda|) = \int_0^\infty \bar{\mathbb{S}}_1(\chi)\, e^{-|\lambda|\chi}\, d\chi < \infty, \tag{6.60}$$

which is the Laplace transform of the kernel $\bar{\mathbb{S}}_1$ on $[0, \infty)$. Since the condition for the existence of the Laplace transform is that kernel $\bar{\mathbb{S}}_1$ is itself exponentially bounded, our assumption of exponential boundedness implies that the moment generating function exists for $\lambda \in (-\infty, 0]$.

In the language of the preceding subsection, the moment generating function exists on $(-\Delta_-, \Delta_+]$, where $\Delta_- = \infty$ and $\Delta_+ = \eta$. Since our kernel $\bar{\mathbb{S}}_1$ is in addition nonnegative, and integrates to one, all assumptions in (H1) are satisfied for the kernel $\bar{\mathbb{S}}_1$ (for comparison, recall the kernel was denoted with the symbol k).

Further, the assumptions (J2) imply that the assumptions (H2) are met for (6.56). Hence all conditions in (H1) and (H2) are met for the autonomous model (6.45), so Theorem 6.4 guarantees that the spreading speeds are (6.57) and (6.58). □

Finally, since Equation (6.45) is directly connected to our model (6.9), we can establish spreading speeds for the solution $u(x, t)$ to (6.9). We must be careful however, since the solution to (6.45) is given as $u(\chi, t)$. We can approximate the spreading speeds $c^{\pm}$ given in (6.57) and (6.58) respectively as $c_0^{\pm} \approx \frac{\Delta\chi}{\Delta t} = s_0^{-1} \frac{\Delta x}{\Delta t}$. It is clear that the spreading speeds in x-coordinates are $s_1\, c_0^{\pm}$.

We thus have our main spreading result:

Theorem 6.6: *Suppose the assumptions in (S1), and (J1), described in this subsection hold. The spreading speeds for solutions of Equation (6.9), with compactly supported initial data in $\mathbb{R}$, are:*

$$c^{+} = s_1 \inf_{0<\lambda<s_0\eta} \frac{\frac{d\tilde{c}}{du}(0) - d + s_1^{-1} \int_0^\infty \mathbb{S}(y)\, e^{\lambda s_1^{-1}\, y}\, dy}{\lambda}, \tag{6.61}$$

in the downwind direction (positive x), and in the upwind direction (negative x) by:

$$c^{-} = s_1 \inf_{0<\lambda<\infty} \frac{\frac{d\tilde{c}}{du}(0) - d + s_1^{-1} \int_0^\infty \mathbb{S}(y)\, e^{-\lambda\, s_1^{-1} y}\, dy}{\lambda}. \tag{6.62}$$

Proof. This Theorem follows from Lemma 6.2, as we will see. As explained in that Lemma, the assumptions (H1) and (H2) required in Theorem 6.4 are satisfied. By definition, $\bar{\mathbb{S}_1}(\chi) = \mathbb{S}_1(s_1\chi) = \frac{1}{d}\mathbb{S}(x)$, from which it follows

$$d\int_0^\infty \bar{\mathbb{S}_1}(\chi)\, e^{\lambda\chi}\, d\chi = \int_0^\infty \mathbb{S}(x)\, e^{\lambda s_1^{-1}\, x}\, d(s_1^{-1}\, x) \tag{6.63}$$

which explains the absence of d, and the presence of the term s_1^{-1} multiplying the integral term in Equations (6.61) and (6.62), when one compares the latter formulae to the spreading speeds (6.57) and (6.58) respectively (established in Lemma 6.2).

Further, that $\frac{d\tilde{c}}{du}(0) = \tilde{f}(0)$ is easily seen from Equation (6.55). Finally, the bounds on λ are determined by noticing that $\chi \in [0, \eta] \Rightarrow x \in [0, s_1\eta]$, so in addition $\chi \to \infty \Rightarrow x \to \infty$. □

As an important note, consider that as $\lambda \to 0^+$, we have c^- appearing in (6.62) tending to infinity. Further, it is clear that the infimum term in c^- is a decreasing function of λ for $\lambda > 0$, and tends to zero as $\lambda \to \infty$. It follows that c^- for our model is zero, as expected: there is no spread in the wind direction, in the spotting dominated case.

Finally, we notice that if $\mathbb{S}$ does not possess a moment generating function, then neither does $\mathbb{S}_1$. This establishes our final primary result of this chapter, namely the existence of spotting accelerated solutions.

Theorem 6.7: *With the assumptions (S1) on $\mathbb{S}$ in this subsection,* except the assumption of exponential boundedness*, the spreading speed c^+ in the downwind direction of the solution to (6.9), is infinite if and only if $\int_0^\infty \mathbb{S}(x)e^{\lambda x}dx = \infty$ for all positive λ.*

Proof. As in the proof of Lemma 6.2, Equation (6.45) is completely analogous to the model (6.56), and consequently we can apply Theorem 6.5 to (6.56). Hence the spreading speed of solutions to (6.56) is infinite if and only if $\int_0^\infty \mathbb{S}(x)e^{\lambda x}dx = \infty$ for all positive λ. But the spreading speed of solutions to (6.56) are proportional to the spreading speeds for (6.9), with proportionality constant $s_1 > 0$. So if compactly supported data for (6.56) evolves to an accelerating solution, so does compactly supported data for (6.9), as required. □

6.7 Chapter summary

In this Chapter we investigated the well-posedness of initial value problems for Equation (6.1) and (6.9), which were derived in Chapter 2.

For the case where local spread occurs on the same timescale as spotting, in Sections 6.2 and 6.3 we proved the well-posedness of (6.1). This will be relevant for future study, where we would like to study conditions under which spotting is the dominant spreading mechanism. Further, it is important to know we have unique solutions before embarking on numerical investigation, as we will do for analogues of these equations in Chapter 7.

In addition, for the spotting-dominated case, which will prove to be the most important case in our numerical investigations in Chapter 7, we obtained several results. By appealing to abstract results on traveling waves in [94], in Chapter 6.5 we were able to establish the existence of monotone travelling wave solutions to (6.7). In Chapter 6.6, in the case of an exponentially bounded kernel, we found expressions for the asymptotic rate of spread of initially compactly supported solutions, by appealing to spreading results established by Jin and Lewis [41]. We further demonstrated that if the kernel is exponentially unbounded, then there is no lower bound for the spreading speed, and we must have acceleration. Numerical investigation of analagous equations, for exponentially unbounded kernels explored in Chapter 7, reveal acceleration in the leading edge of solutions.

The spreading speed results obtained in Chapter 6.7 indicate that the spread rate depends on the kinetics, the heat loss rate, as well as the spotting kernel. This result is significant, since we will see that even compactly supported spotting kernels may give rise to spreading speeds greater than that predicted for a corresponding reaction-diffusion equation.

Chapter 7

Numerical investigation of traveling waves and pulses for the iPDE models from Chapter 2.

7.1 Chapter Introduction

In this Chapter we perform numerical investigation of the continuous-type equations derived in Chapter 2, with no time delay. We proceed in increasing levels of complexity, first examining the one-component model for the expected fire probability $u(x,t)$, as in Equations (2.39) or (2.45). We discuss numerical methods used to solve initial value problems in Section 7.2.

In Section 7.3 we display that solutions arising from an i-PDE model with a compactly-supported kernel, with compactly supported initial conditions for $u(t)$ evolve into right-travelling wavelike solutions, with constant wavefront shape and spreading speed. For a choice of an exponentially unbounded kernel, we show a solution whose shape and spreading speed are changing with time. The leading edge of this solution appears to be increasing its spread rate with time, i.e. accelerating. Further, for a compactly supported uniform kernel (an approximation to some of the 'averaged' spotting kernels, in particular example 1, from Section 5.3), we show a constant-speed travelling wave.

In the remainder of the chapter, we augment our models for u, to consider models including the total fuel loading fraction v. In section 7.3 we begin by investigating some kinetic models for u and v, ignoring the spatial parts of the process. We propose some qualitative models for how the presence of v can increase u. This is analogous to combustion, or to a predator-prey type model, where u is the predator that 'feeds' off v. These models provide the nonlinear growth/decay terms appearing in the modified version of (2.39), given by

$$\frac{\partial u(x,t)}{\partial t} = c(u(x,t), v(x,t))v(x,t) - du(x,t), \tag{7.1}$$

and the Equation governing v is again (2.36), namely $v_t = -c(u,v)v$ Similar models for combustion waves have been proposed in the literature and are mentioned where they appear.

In Section 7.5 we add diffusion to the temporal dynamics of fire probability and fuel loading fraction, outlined in the preceding paragraph. We obtain a reaction-diffusion equation for the expected fire probability u. We do so by adding a diffusion term to the right hand of the kinetic equations, and for compactly supported initial data we see the emergence of travelling pulse-type solutions, which move with constant shape and spreading speed. We investigate how different kinetics result in different pulse shapes and speeds, as well as the total fuel loading fraction v remaining.

Such models can be compared to real data: spread rates are known for various scenarios [40], and these can be related to the diffusion coefficient. Further, the expected fuel loading fraction remaining, as well as well as the 'residence time' (think of the lapse of time during which the leading edge at a given location takes until the trailing edge reaches the same location), are both outputs of the FBP system [40]. An important question, for future research, is to address the relative effect of local spread and spotting on realistic models of fire invasions.

In Section 7.6 we add in the spotting operator, and for the parameter, kinetics, and kernel choices we make, spotting dominates the dynamics. Diffusion is seen to have little to no influence for the latter choices, so we confine our investigation to the spotting-dominated case (2.45). We investigate how different choice of kinetic models, as well as different spotting kernels, can effect the spreading speed and possible acceleration of initially compactly-supported initial data. Our purpose here is qualitative, since by combining all possible spotting kernels derivable from our general formula, we must consider more than 500 models together with their parameters. Such an investigation is beyond the scope of this thesis.

It has been noted as early as Mollison's 1972 paper [60], for one-component models, that exponentially bounded kernels allow finite spreading speeds, while exponentially unbounded kernels do not. Hence the exponentially bounded kernel provides a measure of how fat the 'tail' of a spotting kernel can be. We include it in our analysis in Section 7.6, in addition to the uniform and exponentially unbounded kernels explored in Section 7.3, in part to illustrate analogous results for our two-component models. In future research we would like to explore analytically how the travelling pulses exhibited in this chapter are connected to model parameters, given a more realistic spotting kernel and improved local spread/combustion modelling.

7.2 Numerical solutions of the equations in this Chapter

We wrote code in Matlab to determine solutions to the types of initial value problems from this Chapter. We used very simple numerical methods in each case.

Each of the ordinary differential equations is solved by forward-differencing [6]. We divide time and space into a mesh, with constant $\Delta x = 1$, which we interpret to represent 1 metre, and set time $\Delta t = 0.5$. To approximate the temporal derivative at $u(x_i, t)$, where t is a nonnegative integer, we approximate

$$\frac{\partial u(x_i, t)}{\partial t} \approx \frac{u(x_i, t+1) - u(x_i, t)}{\Delta t} + O(\Delta t), \tag{7.2}$$

where the order symbol $O(\Delta t)$ indicates that we have first-order convergence in time [6].

Similarly, we use the approximation (7.2) in the other equation types to model the temporal derivative. This restricts our scheme to first order accuracy. Higher-order solvers, e.g. Runge-Kutta solvers, could be implemented

[6] to improve temporal convergence.

Wherever a diffusion term appears, we use central differencing in space to approximate the second-derivative term, this time to second-order accuracy [6],

$$\frac{\partial^2 u(x_i,t)}{\partial x^2} \approx \frac{u(x_i+\Delta x,t)+u(x_i-\Delta x,t)-2u(x_i,t)}{4\Delta x^2} + O(\Delta x^2) \qquad (7.3)$$

The integral term is approximated using Matlab's trapz routine, a trapezoidal rule.

The error in the solution arising from the use of the trapezoidal rule can be reduced by using improved quadrature methods for approximating the integral term, like when using Legendre polynomials as the quadrature weights in a Newton-Cotes formula [81]. This may be needed in situations where the diffusion-wave is close in speed to the spotting-driven wave for the fire probability, in future research.

7.3 Traveling waves for the single equation model in the spotting-dominated case, with no time-delay

In this section, we will consider the model:

$$\frac{du}{dt} = \alpha\, r\, u(1-u) - d\, u + \int_0^\infty \mathbb{S}(y)\, u(x-y,t)\, dy, \qquad (7.4)$$

where the nonlinearity is of logistic form. In the final sections of this chapter, we will consider other types of kinetics and their influence on spotting, in the context of the full model where we include the total fuel loading fraction v.

Unless otherwise specified, the parameters are $\alpha = 0.7$, $r = 1$, and $d = 0.5$.

7.3.1 An uniform spotting kernel, travelling waves

In this section we consider the spotting kernel $\mathbb{S}$ given in (7.4), with compactly supported initially conditions for u. We choose a uniform spotting kernel for u given in Equation (7.23) below. The results are plotted in Figure 7.1.

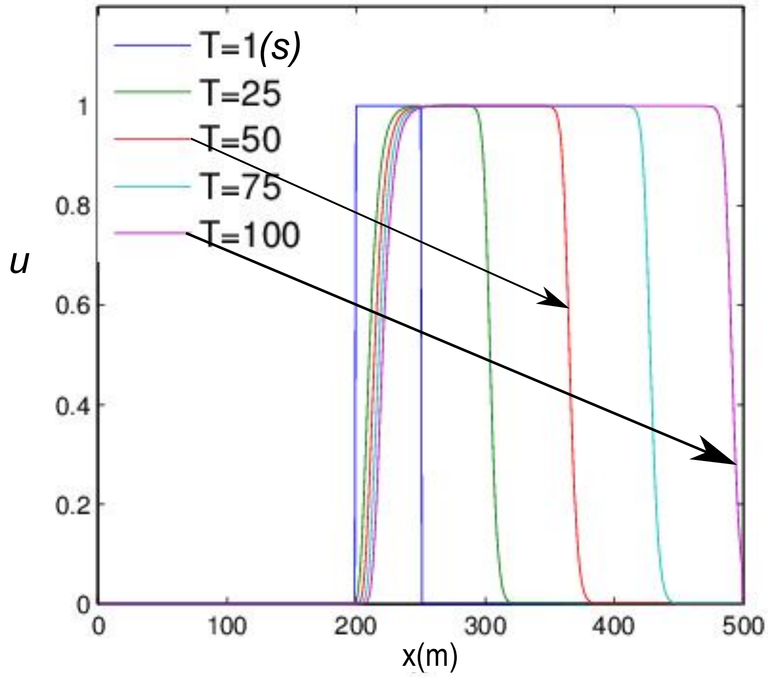

Figure 7.1: We illustrate how a compactly supported initial condition for (7.4), with uniform spotting kernel given in (7.23) for $L = 5$ We plot $u(t)$ versus x, for various snapshots in time; the arrows point out the leading edge.

We see that the solution grows into a right-travelling wave, moving with constant speed and shape after an initial transient period. We notice that u is zero for $x < 0$, since in this spotting-dominated case we only have motion to the right (and no diffusion term). Hence this is not a travelling wave in the traditional sense, since $\lim_{x\to-\infty} u(x,t) = 0$.

Of notice is that the spreading speed of this wave, which is compactly supported, is significantly greater than the diffusion wave with the corresponding T4 kinetics model descried in Section 7.5.

7.3.2 A fat-failed kernel, accelerating solution

Here we consider the model (7.4), with the fat-tailed kernel

$$\mathbb{S}(y) = \exp\left(-\sqrt{y}\right). \tag{7.5}$$

For compactly supported initial data $u(0)$, the solution evolves into an

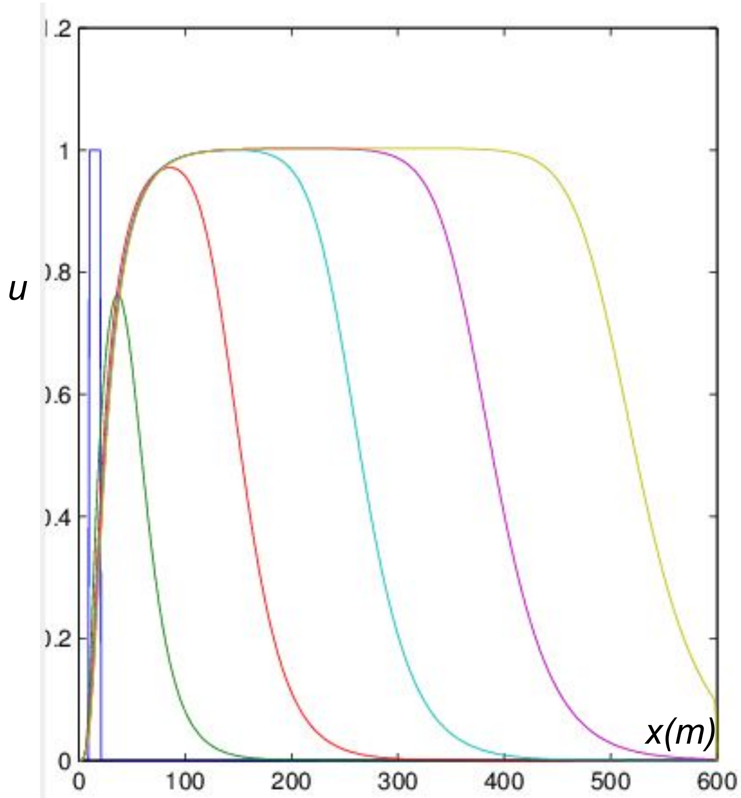

Figure 7.2: We plot accelerating solutions $u(t)$ to (7.4) versus x, where x is measured in metres, for the exponentially unbounded kernel $\mathbb{S}(y)$ from (7.5), showing the solution at various snapshots in time (measured in seconds), and the spatial extent reached. Different coloured waves correspond to different instances of time. Upon close comparison of the level sets at the different snapshots, close to $u \approx 0.2$ one can distinctly note the spatial separation between level sets expanding with time. Further, the wave does not evolve to have a constant shape.

accelerating wave, depicted in Figure 7.2 below.

Notice that the distance between the leading edges of the u-waves is growing with time, a clear indication of acceleration. Further, the shape of the wave is evolving with time, rather than becoming a wave of fixed shape.

7.4 The temporal dynamics of combustion and heat loss

Here for the first time we determine the time-evolution of fire probability density $u(x,t)$ and total fuel loading fraction $v(x,t)$ first defined in Chapter 2, ignoring the spatial process. That is, we consider the system of equations:

$$\begin{aligned}\frac{du}{dt}(x,t) &= \alpha\,\underbrace{c\,(u(x,t),v(x,t))\;\; v(x,t)}_{\text{Combustion}} - \underbrace{\delta\;(u(x,t))}_{\text{Heat loss}}\\ \frac{dv}{dt}(x,t) &= -\,\underbrace{c\,(u(x,t),v(x,t))\;\; v(x,t)}_{\text{Combustion}},\end{aligned} \tag{7.6}$$

where $\alpha \in [0,1]$ represents the efficiency with which the burning of combustible fuel is converted into an increase in the local fire probability.

The specific functional forms which we will employ in Equations (7.6), are based on the combustion wavefront models in ([1], [11]), with the exception of the logistic model which is new (at least in this context). We will assume that the heat loss term is linear, so we write

$$\delta(u(x,t)) = d\;u(x,t), \qquad\qquad d > 0. \tag{7.7}$$

This type of heat loss is analogous to Newton's Law of Cooling, with heat being lost to the surrounding environment.

Unless otherwise specified as in the preceding section we assume $\alpha = 0.7$, $d = 0.5$.

7.4.1 Case T1: Mass-action kinetics

In our first model we consider mass-action kinetics with heat loss:

$$\begin{aligned}\frac{du}{dt}(x,t) &= \alpha\; u(x,t)\; v(x,t) - d\; u(x,t)\\ \frac{dv}{dt}(x,t) &= -u(x,t)\; v(x,t).\end{aligned} \tag{7.8}$$

This type of model was used by Billingham and Needham, as reported in [1], to model an isothermal autocatalytic chemical reaction of mixed order, where

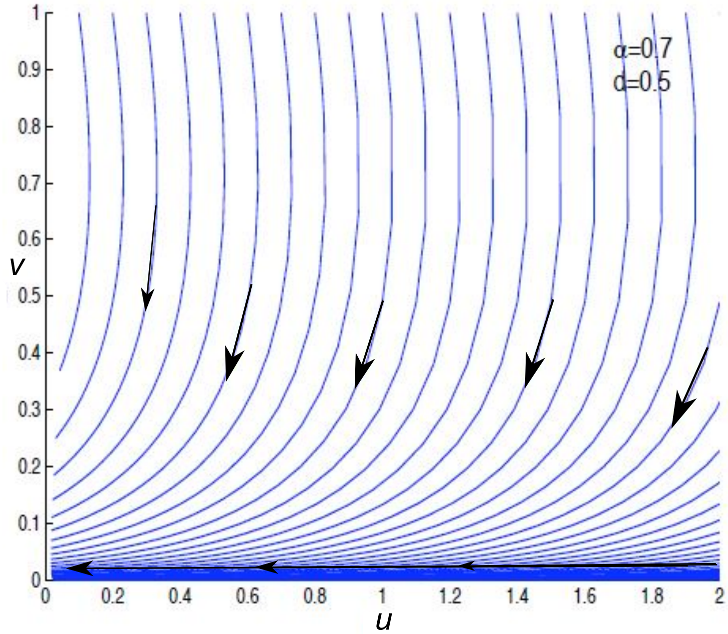

Figure 7.3: We plot a partial phase portrait for mass-action kinetics model (7.8), with a few arrows to indicate the direction of trajectories. The parameters are $\alpha = 0.7$, and $d = 0.5$. On the $y-$axis we plot the total fuel loading fraction v, while on the x-axis we plot the fire probability density u.

u is the reactant and v is the autocatalyst. There is a direct analogy between reactant/autocatalyst and fire probability/total fuel loading fraction densities.

Presented in Figure 7.3 below is a partial phase portrait for the dynamics of u, v, illustrating the general behavior of the model. In particular, both u and v are decreasing, and u decreases to zero very rapidly as v tends to zero.

7.4.2 Case T2: Second-order kinetics in u

In this section we present another model used by Billingham and Needham [1], corresponding to a higher-order autocatalytic reaction, and which is non-linear in u:

$$\begin{aligned}\frac{du}{dt}(x,t) &= \alpha\, u(x,t)^2\, v(x,t) - d\, u(x,t)\\ \frac{dv}{dt}(x,t) &= -u(x,t)\, v(x,t).\end{aligned} \tag{7.9}$$

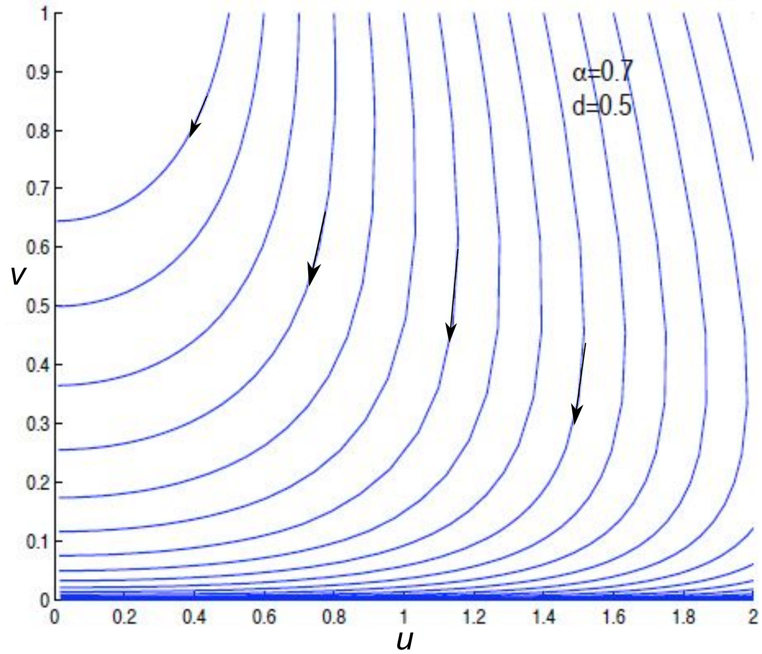

Figure 7.4: We plot a partial phase portrait for u-nonlinear kinetics model (7.9), with a few arrows to indicate the direction of trajectories. The parameters are $\alpha = 0.7$, and $d = 0.5$. On the $y-$axis we plot the total fuel loading fraction v, while on the x-axis we plot the fire probability density u.

Again, in the following Figure 7.4 below we show a partial phase portrait for the dynamics of u, v described in (7.9).

Relative to the mass-action case, the trajectories are similar, with most of the trajectories accumulating close to $v = 0$ where trajectories are very rapidly decreasing in u. Notice also the relatively higher end-values of v along trajectories, relative to Figure 7.3.

7.4.3 Case T3: Arrhenius kinetics

Another commonly used model [12] is the so-called Arrhenius kinetics, described by the system

$$\begin{aligned}\frac{du}{dt}(x,t) &= \alpha\ \exp\left(\frac{-k}{u(x,t)}\right) v(x,t) - d\ u(x,t)\\ \frac{dv}{dt}(x,t) &= -\exp\left(\frac{-k}{u(x,t)}\right) v(x,t),\end{aligned} \tag{7.10}$$

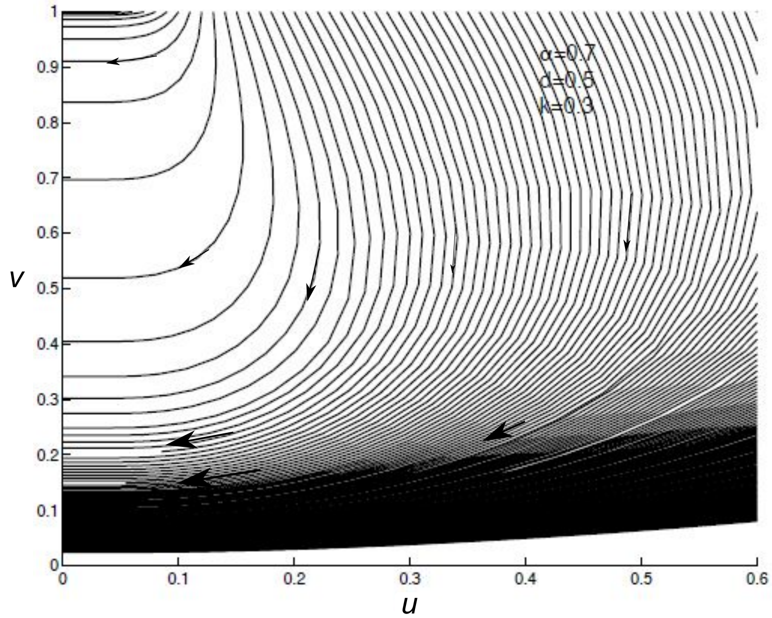

Figure 7.5: We plot a partial phase portrait for the Arrhenius kinetics model (7.10). On the $y-$axis we plot the total fuel loading fraction v, while on the x-axis we plot the fire probability density u.

where $k > 0$ is a constant. In the heat-flow analogy, k is related to the activation energy E_a, and the universal gas constant R.

Plotted in Figure 7.5 below we show a sample phase portrait for the system (7.10). Relative to the preceding cases, we find a very strong accumulation of trajectories which head to the v-axis, for low values of v.

Examining the upper left portion of Figure 7.5, we notice that for $u < 0.1$, trajectories head straight to the v-axis, while for slightly larger values there is first an increase in u, followed by a subsequent decrease. Notice also it is only for approximately $u < 0.2$ that the final total fuel loading fraction is above about $v \approx 0.2$.

Finally, we choose $k = 0.5$, as we did in the first section of this chapter.

7.4.4 Model T4: Logistic-type kinetics

In this section we will build a model around the idea of logistic growth for u,

$$\frac{du}{dt}(x,t) = \alpha\ r\ u(x,t)(1-u(x,t))\ v(x,t) - d\ u(x,t)$$
$$\frac{dv}{dt}(x,t) = -r\ u(x,t)(1-u(x,t))\ v(x,t). \tag{7.11}$$

where r is the linearized growth rate for r near $u = 0$, called the intrinsic growth rate. Irrespective of the initial conditions, $u = 1$ is the unique global attracting equilibrium of the ODE $u' = r\ u(1-u)$.

Plotted in Figure 7.6 below we show a sample phase portrait for the system (7.11), with $r = 1$ (since we have $\alpha = 0.7$ already, and it's only the product $r\ \alpha$ which matters). We find that for $u > 1$, we have trajectories where the fuel fraction v is *increasing*, which is clearly not physical. Hence we must restrict our choice of model parameters so that u stays below unity.

7.4.5 Model T5: Ignition thresholds

It is important to note that many models (see e.g. [11]) use the notion of an ignition temperature, below which combustion does not occur.

We would like to use an analogy here, namely that if the fire probability is below a threshold $\underline{u}$, then combustion does not occur. This can be modeled using the Heaviside (or unit step) function $\mathbb{H}(u)$, to produce a very general model:

$$\frac{du}{dt}(x,t) = \alpha\ \mathbb{H}(u-\underline{u})\ h(u(x,t))\ v(x,t) - d\ u(x,t)$$
$$\frac{dv}{dt}(x,t) = -\mathbb{H}(u-\underline{u})\ h(u(x,t))\ v(x,t), \tag{7.12}$$

where $h(u(x,t))$ is a prescribed function which determines the burning kinetics.

In the extreme case of timbre-dry conditions, we may approximate $\underline{u} \approx 0$ in (7.12), so that we may obtain any of the preceding kinetic models in this limit. We will not pursue the case (7.12) for $\underline{u} \neq 0$ in what follows.

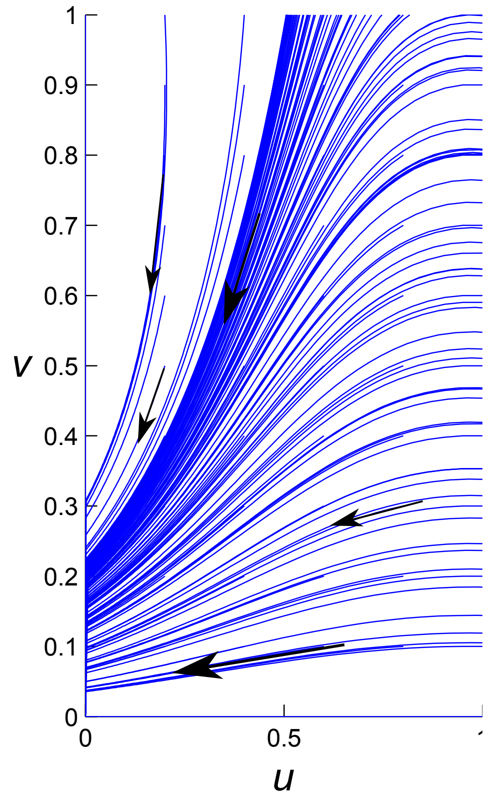

Figure 7.6: We plot a partial phase portrait for the logistic kinetics model (7.11). On the $y-$axis we plot the total fuel loading fraction v, while on the x-axis we plot the fire probability density u. The parameters are $\alpha = 0.7$, $d = 0.5$ and $r = 1$. We notice that for $u > 1$, there are trajectories where v is increasing with time, which is physically impossible. Hence we must restrict ourselves to choices of the parameters such that $u \leq 1$.

7.5 Adding diffusion to the temporal dynamics

In this section, we add diffusion to most of the temporal dynamical models introduced in the previous section. We do this because many fires travel primarily by local spread, which we are modelling using diffusion. In addition, a major question for further research is when the local spread drives the invasion, as opposed to the cases considered in Section 7.6, where spotting dominates the fire's invasion.

Here and in what follows, I choose the parameters $\alpha = 0.7$, $d = 0.5$, and $D = 0.5$, unless specified otherwise. This is for comparison's sake, so we can examine the effect of changing the type of kinetic model used.

7.5.1 Traveling pulses for the mass-action model T1

Let's first consider the type of behavior we expect to find for the augmented diffusion model corresponding to the case T1. The augmented model for (7.8) reads:

$$\begin{aligned} \frac{du}{dt}(x,t) &= D\frac{\partial^2 u(x,t)}{\partial x^2} + \alpha\, u(x,t)\, v(x,t) - d\, u(x,t) \\ \frac{dv}{dt}(x,t) &= -u(x,t)\, v(x,t). \end{aligned} \tag{7.13}$$

In Figure 7.7, we illustrate how a compactly supported initial condition for u, given $v = 1$ everywhere, evolves with time. Instead of traditional traveling waves, we observe traveling pulses for $u(x,t)$, appearing in the left-most picture, propagating rightward with space. Notice that behind the wavefront, u tends to 0, as the combustion ends and heat is lost to the environment.

The right-most picture in Figure 7.7 illustrates the time-evolution of v, which is effected only by the presence of fire. The fuel fraction in this case decreases as the front passes through a region, but not to zero for this choice of parameters, indicating incomplete combustion.

7.5.2 Traveling pulses for the non-linear case T2

Next let's consider the diffusion model corresponding to the T2-kinetics, namely

$$\begin{aligned} \frac{du}{dt}(x,t) &= D\frac{\partial^2 u(x,t)}{\partial x^2} + \alpha\, u(x,t)^2\, v(x,t) - d\, u(x,t) \\ \frac{dv}{dt}(x,t) &= -u(x,t)^2\, v(x,t). \end{aligned} \tag{7.14}$$

This model also exhibits traveling pulses, but not necessarily for the parameter values we've been assuming thus far. To observe the pulses in Figure 7.8, we choose $\alpha = 0.9$ and $d = 0.5$. Clearly the stability of these pulses depends on the model parameters. We find that the shape of the u-waves is

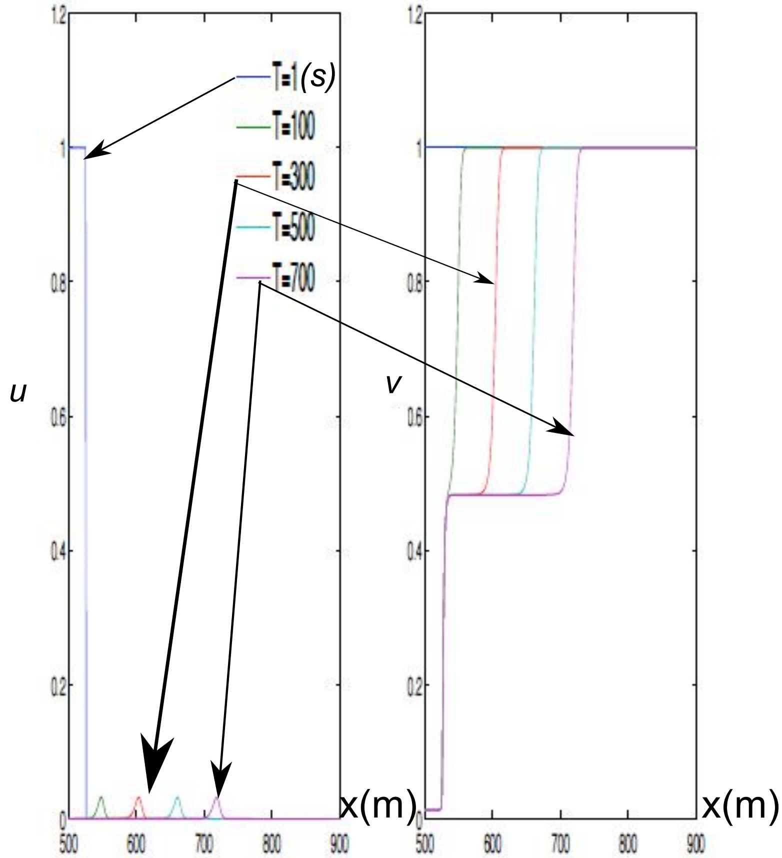

Figure 7.7: Illustration of traveling pulses for the solution to the system (7.13), with dynamics determined by model T1. In the left figure we plot $u(t)$ versus x, measured in metres, for several values of the time t, measured in seconds. The different colours represent different snapshots in time, and the arrows serve to identify the wavefront's location at each of these times. In the right graph we show similar snapshots in time of the total fuel loading fraction $v(t)$ versus x.

more sharply peaked than those exhibited in Figure 7.7, the peaks have greater amplitude, and the u-waves travel more slowly relative to the T1 case.

In addition, in the right-most graph in Figure 7.8 we observe that the total fuel loading fraction $v \to 0$ as the front passes by, corresponding to complete combustion.

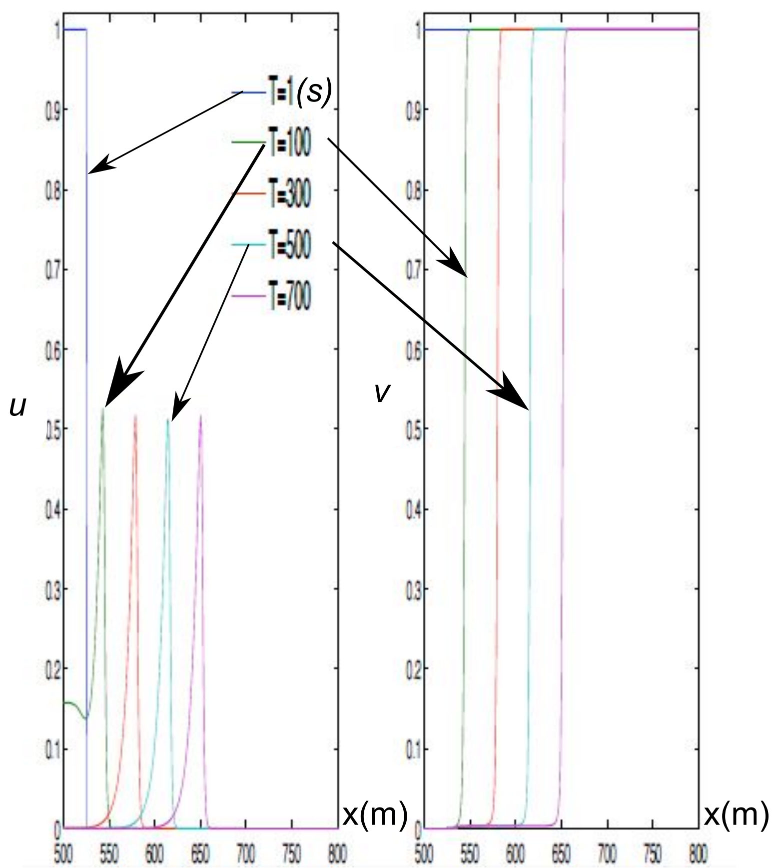

Figure 7.8: Illustration of traveling pulses for the solution to the system (7.14), with dynamics determined by model T2. In the left figure we plot $u(t)$ versus x for several values of the time t. In the right graph we show similar snapshots in time of the total fuel loading fraction $v(t)$ versus x.

7.5.3 Travelling pulses for the Arrhenius model T3

In this subsection we consider the diffusion model corresponding to the Arrhenius kinetics model (7.10),

$$\begin{aligned} \frac{du}{dt}(x,t) &= D\frac{\partial^2 u(x,t)}{\partial x^2} + \alpha \ \exp\left(\frac{-k}{u(x,t)}\right) v(x,t) - d\ u(x,t) \\ \frac{dv}{dt}(x,t) &= -\exp\left(\frac{-k}{u(x,t)}\right) v(x,t), \end{aligned} \tag{7.15}$$

The dynamics are demonstrated in Figure 7.9 below. Analogous to the T2 case, traveling pulses do not appear for all parameter values. In particular,

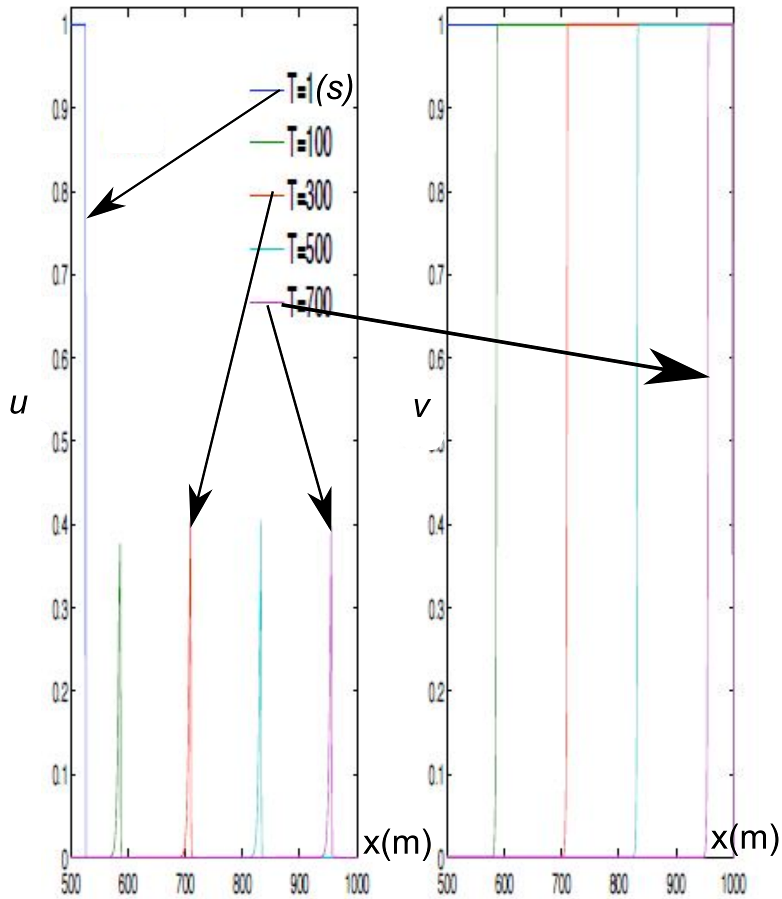

Figure 7.9: Illustration of traveling pulses for the solution to the system (7.15), with dynamics determined by the Arrhenius model T3, in the case where $k = 0.5$. In the left figure we plot $u(t)$ versus x for several values of the time t. In the right graph we show similar snapshots in time of the total fuel loading fraction $v(t)$ versus x.

setting $k = 3$, and keeping the values for α and d, the initial condition for u simply decreases to zero without propagating.

We observe in Figure 7.9 very sharply peaked traveling pulses for u, which travel the fastest of all cases considered so far. Further, the right-most graph shows that again $v \to 0$ as the fire front passes by, corresponding to complete combustion.

7.5.4 Traveling pulses for the logistic model T4

Next let's consider the diffusion model corresponding to the logistic kinetics model (7.11),

$$\begin{aligned}\frac{du}{dt}(x,t) &= D\frac{\partial^2 u(x,t)}{\partial x^2} + \alpha\, r\, u(x,t)(1-u(x,t))\, v(x,t) - d\, u(x,t)\\ \frac{dv}{dt}(x,t) &= -r\, u(x,t)(1-u(x,t))\, v(x,t),\end{aligned} \tag{7.16}$$

In Figure 7.10 below, we illustrate traveling pulses for this model, with the choice $r = 1$ for simplicity (it is only the product $\alpha\ r$ which is important). We have also illustrated the early evolution of the left-traveling pulse. Notice that the magnitude of the traveling pulses for u are small compared to the preceding cases, and the speed of propagation is dramatically slower.

From the right-most graph in Figure 7.10, the resulting fuel fraction v is not completely exhausted by the passage of such a front. One can also notice from the right-most graph, at the leftmost portion, a dip in the total fuel loading fraction, which corresponds to the effect of the left-traveling u-wave.

7.6 The spotting-dominated case: traveling pulses

In this section we consider finally the full model including the spotting term,

$$\begin{aligned}\frac{du}{dt}(x,t) &= D\frac{\partial^2 u}{\partial x^2}(x,t) + \alpha\, c\,(u(x,t),v(x,t))\ v(x,t) - d\, u(x,t) \qquad (7.17)\\ &\quad + \int_0^\infty \mathbb{S}(y)\, u(x-y,t)\, dy\\ \frac{dv}{dt}(x,t) &= -c\,(u(x,t),v(x,t))\ v(x,t). \qquad (7.18)\end{aligned}$$

Simulations with all cases in this section indicate that the effect of diffusion is negligible on the evolution of u and v. In particular, the right-most region of the right-traveling u-pulse is identical if we include diffusion or not, and the right-traveling pulse moves with the same speed and shape in either case. The left-spreading speed is negligible compared to the right-spreading speed for the u-pulses in all cases. This is partly due to 'sweeping up' of leftward diffused probability by the spotting process. Finally, after an initial transient

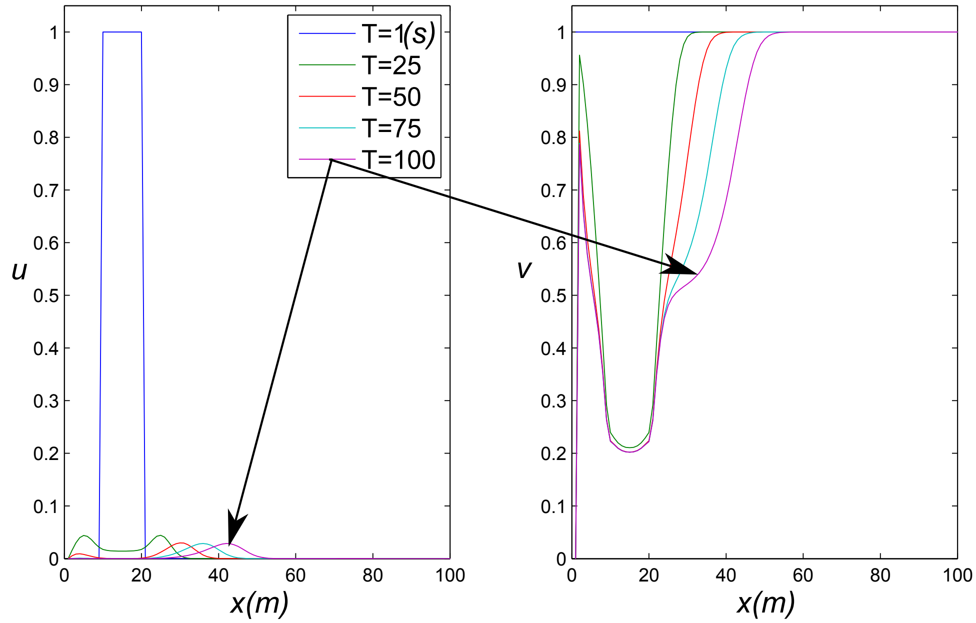

Figure 7.10: Illustration of traveling pulses for the solution to the system (7.16), with dynamics determined by the logistic model T4. In the left-most graph we plot $u(t)$ versus x for several values of the time t. In this case we also illustrate the left-traveling pulse which results from the compactly supported initial condition, at least up to $t = 25$. It evolves identically in shape and speed to the right-traveling pulse. In the right-most graph we show similar snapshots in time of the total fuel loading fraction $v(t)$ versus x.

period, the region behind the right-traveling u-pulse looks essentially identical with or without diffusion.

Perhaps more importantly, the spotting-dominated case is the one of primary interest for this thesis: if the diffusion-wave is faster than the spotting-wave, then the main front will overrun all spot fires, so there is no need to account for spotting. An interesting problem, which we will leave open, is for completely realistic spotting kernels $\mathbb{S}(y)$, to determine conditions on the model parameters such that the diffusion-pulse overruns the spotting-pulse.

It is therefore sufficient to consider the spotting-dominated model:

$$\begin{aligned}\frac{du}{dt}(x,t) &= +\alpha\, c\,(u(x,t),v(x,t))\;\, v(x,t) - d\, u(x,t) + \int_0^\infty \mathbb{S}(y)\; u(x-y,t)\; dy \\ \frac{dv}{dt}(x,t) &= -c\,(u(x,t),v(x,t))\;\, v(x,t).\end{aligned} \tag{7.19}$$

This results of this section show explicitly how spotting can drive a front's spread. The results are qualitative, and the kernels we determine are chosen for comparative purposes, as opposed to attempting to employ the most physically realistic kernels. To see how one could derive the spotting kernels seen here, see the 'fat'-tailed kernel example from Chapter 5.

In keeping with the preceding sections, unless otherwise specified we set $\alpha = 0.7$, $d = 0.5$, and where relevant $k = 0.5$ and $r = 1$.

For T4 kinetics, we choose

$$c\,(u(x,t), v(x,t)) = r\; u(x,t)\;(1 - u(x,t)). \tag{7.20}$$

For T1 kinetics, we choose

$$c\,(u(x,t), v(x,t)) = u(x,t). \tag{7.21}$$

For T3 kinetics, we choose

$$c\,(u(x,t), v(x,t)) = \exp\,(-\frac{k}{u(x,t)}). \tag{7.22}$$

Remark: The results for T2 type kinetics are very similar to those for the T3 kinetics, with appropriate choice of parameters, so we will not consider them in this section, for the sake of brevity.

7.6.1 T4 kinetics, uniform probability distribution kernel

The first case we consider is that of a uniform kernel spotting kernel $\mathbb{S}$, defined by $\mathbb{S}(y) := U(0, L)(y)$, where:

$$U(0, L)(x - y) := \begin{cases} \frac{1}{L},\ (x - y) \in [0, L]; \\ 0,\ \text{otherwise}. \end{cases} \tag{7.23}$$

We choose $L = 5$ in Figure 7.11, in which we initially set $v = 1$ everywhere, and observe how a compactly supported initial condition for u evolves into a traveling pulse with constant shape and speed.

The cusp appearing in Figure 7.11 in the right-most graph for v appears

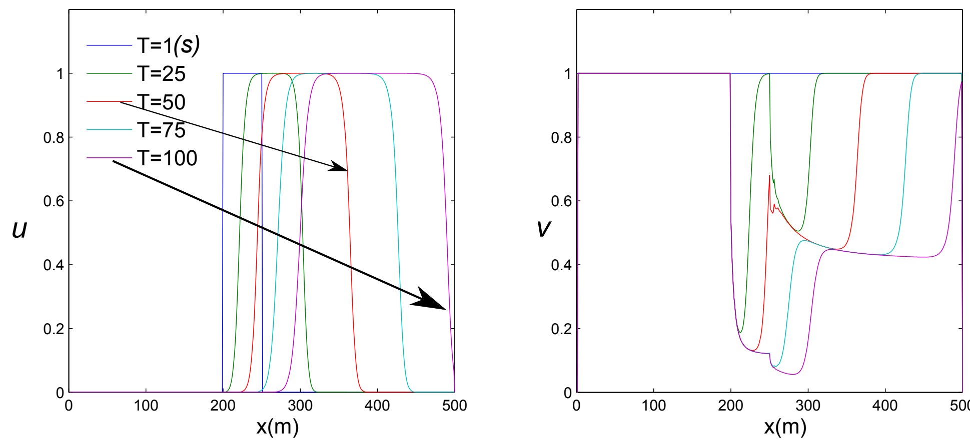

Figure 7.11: Illustration of traveling pulses for the solution to the system (7.19), with dynamics determined by the logistic model (7.20), with uniform spotting kernel given in (7.23), and with $L = 5$. In the left-most graph we plot $u(t)$ versus x for several values of the time t. The different colours represent different snapshots in time, and the arrows point out the leading edge. In the right-most graph we show similar snapshots in time of the total fuel loading fraction $v(t)$ versus x.

to stabilize, indicating that v need not be differentiable everywhere. We can also see the in the right-most graph that the progress of the u-front is with constant speed, by comparing the spatial separation for the level set $v = 0.8$ between the final few snapshots for v.

7.6.2 T4 kinetics, exponential spotting kernel

Next we consider the case where our spotting kernel $\mathbb{S}$ is exponentially bounded,

$$\mathbb{S}(y) = \lambda \exp\left(-\lambda\, y\right), \tag{7.24}$$

and in this section we choose $\lambda = 0.5$.

In Figure 7.12 we show the solutions to the model (7.19), with the spotting kernel as in (7.24), and with logistic kinetics (7.20).

Notice that a rightward propagating traveling pulse $u(t)$ moving with constant shape and speed to the right develops, and that the shape of the pulses is different from those displayed in Figure 7.11. Also of importance is that u-pulse's peak travels much more slowly relative to those shown in Figure 7.11.

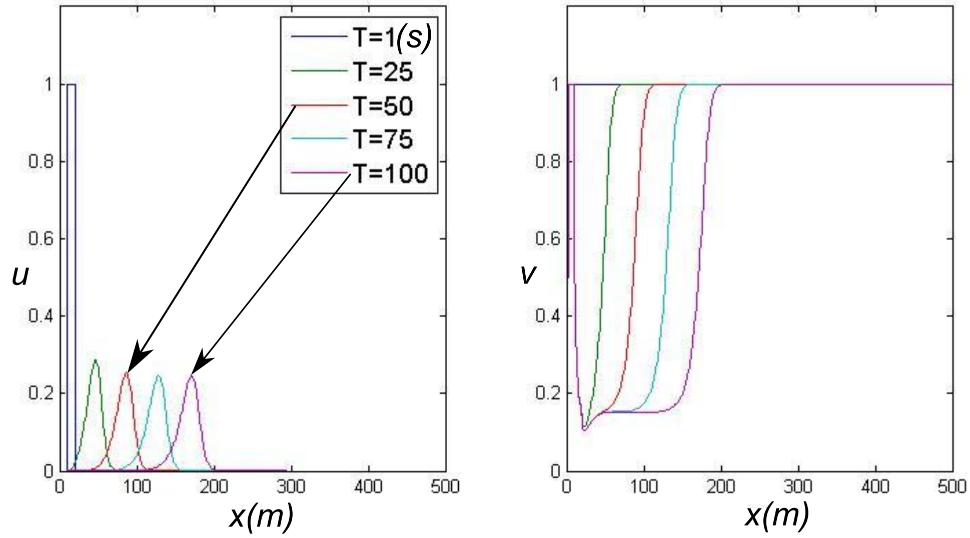

Figure 7.12: Illustration of traveling pulses for the solution to the system (7.19), with dynamics determined by the logistic model (7.20), with exponential spotting kernel given in (7.24), and with $\lambda = 0.5$. In the left-most we plot $u(t)$ versus x for several values of the time t. In the right-most graph we show similar snapshots in time of the total fuel loading fraction $v(t)$ versus x.

This is an example of a compactly-supported kernel (7.23) producing faster invasion speeds than a kernel supported on $\mathbb{R}$ (as in (7.24)).

The snapshots for v in the right-most graph indicate incomplete combustion, though the fuel fraction remaining after the fire's passage is less than that remaining with the uniform spotting kernel (7.23).

7.6.3 T4 kinetics, fat-tailed kernel, : acceleration

Next we consider the fat-tailed kernel

$$\mathbb{S}(y) = \lambda \exp\left(-\sqrt{y}\right), \tag{7.25}$$

where we choose $\lambda = 0.5$. Again we choose logistic kinetics (7.20).

For compact initial data for $u(t)$ as usual, in Figure 7.13 we illustrate an example of an accelerating wave for u. The shape is changing with time, and the spatial extent is growing much more rapidly than in the previous two examples. The level sets of u are spreading apart from each other from one

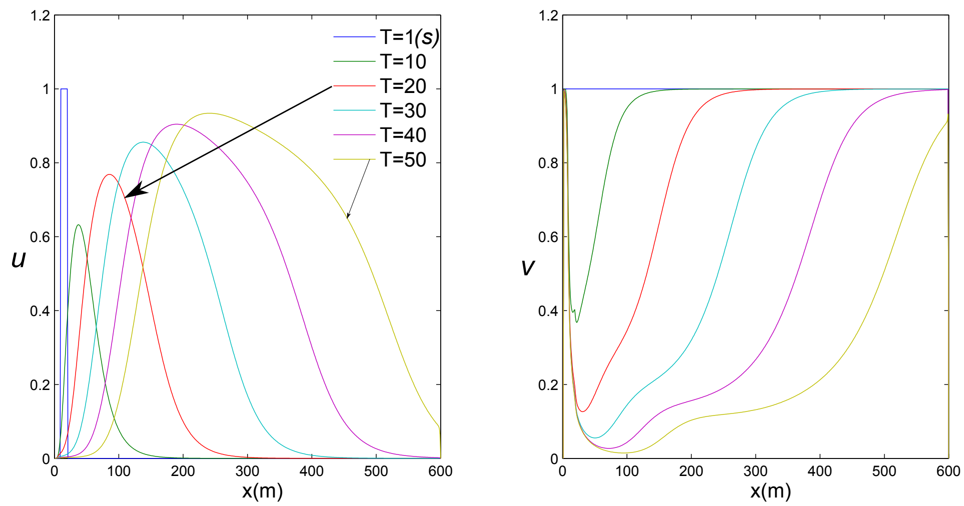

Figure 7.13: Illustration of traveling pulses for the solution to the system (7.19), with dynamics determined by the logistic model (7.20), with exponential spotting kernel given in (7.24), and with $\lambda = 0.5$. In the left-most graph we plot $u(t)$ versus x for several values of the time t. In the right-most graph we show similar snapshots in time of the total fuel loading fraction $v(t)$ versus x. Notice that the shape of the graph for v is also continually evolving with time.

time step to the next, as the leading edge accelerates forward.

The acceleration may also be seen by examining the total fuel loading fraction remaining, displayed in the right-most graph in Figure 7.13, by noticing spatial separation growing between subsequent level sets $v = 0.8$ for the final few snapshots.

7.6.4 T1 kinetics, uniform kernel

Here and in the following two subsections, we repeat the steps as in the preceding three subsections, examining solutions to the system (7.19), but now we use the mass-action kinetics model T1 as in (7.21). We will again assume throughout that $\alpha = 0.7$, and $d = 0.5$ in (7.19).

In this subsection we choose the same spotting kernel as in (7.23), again for the value $L = 5$. We examine such an evolution in Figure 7.14 below.

In the left-most graph we plot snapshots of $u(t)$ versus x. As in the logistic kinetics case, again the initially compactly supported initial condition for u

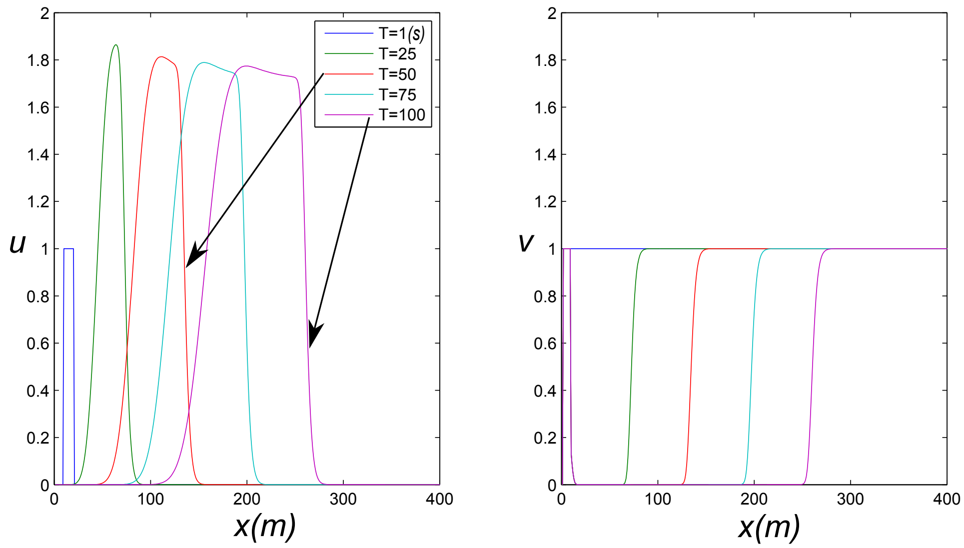

Figure 7.14: Illustration of traveling pulses for the solution to the system (7.19), with dynamics determined by the mass-action model (7.21), with uniform spotting kernel given in (7.23). In the left-most graph we plot $u(t)$ versus x for several values of the time t. In the right-most graph we show similar snapshots in time of the total fuel loading fraction $v(t)$ versus x.

evolves into a traveling pulse u-pulse, eventually assuming constant shape and speed. Notice however that the magnitude of the u-pulses are significantly higher in this case, relative to the corresponding T4 kinetics as illustrated in Figure 7.11, while the shape of the waves are similar.

Further, from the right-most graph in Figure 7.14, where we plot snapshots of $v(t)$ versus x, we observe that we have complete combustion as such a wave passes by, in contrast to the logistic kinetics example with the same uniform spotting kernel.

7.6.5 T1 kinetics, exponential kernel

Next, we examine solutions to (7.19), with mass action kinetics T1, and spotting kernel given by the exponential kernel (7.23), again choosing $\lambda = 0.5$. The results are plotted in Figure 7.15 below.

The evolution for $u(t)$ and $v(t)$ is almost identical in this case to the corresponding T4 kinetics case (which is illustrated in Figure 7.12). In particular,

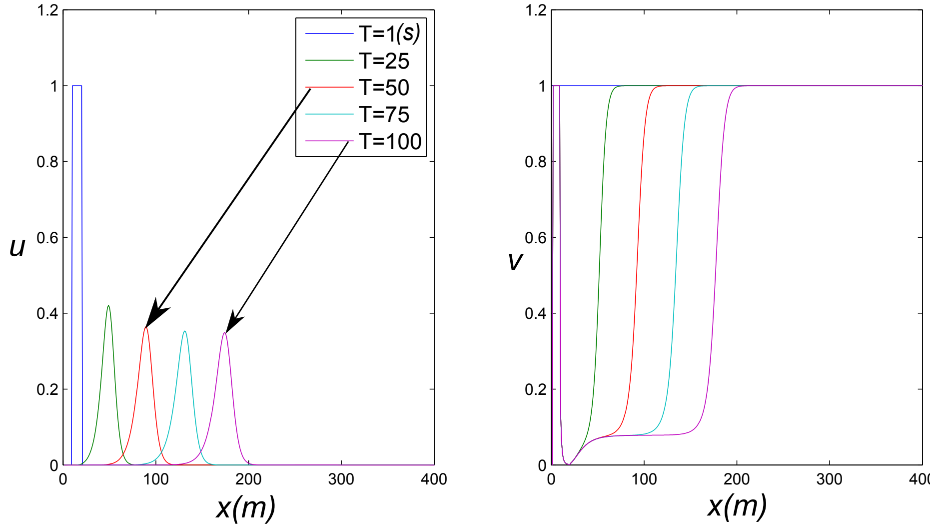

Figure 7.15: Illustration of traveling pulses for the solution to the system (7.19), with dynamics determined by the mass-action model (7.21), with exponential spotting kernel given in (7.24). In the left-most graph we plot $u(t)$ versus x for several values of the time t. In the right-most graph we show similar snapshots in time of the total fuel loading fraction $v(t)$ versus x.

in the left-most graph we see that $u(t)$ evolves into a traveling pulse, with approximately the same shape and rate of spread as in the T4 kinetics case, although the amplitude of the u-pulses is greater relative to the T4 kinetics case.

The most noticeable difference between the evolutions displayed in Figure 7.12 and Figure 7.15 is observed in the right-most graph for $v(t)$, where we see that initially the total fuel loading fraction drops to zero. After the initial transient period, by examining subsequent snapshots for $v(t)$, we see that the total fuel loading fraction remaining is constant, and slightly lower than the corresponding snapshots in Figure 7.12. This makes sense, since the amplitude of the u-waves is higher in this case.

7.6.6 T1 kinetics, fat-tailed kernel: acceleration

To complete this group of results, we examine solutions to (7.19), with mass action kinetics T1 (7.21), and spotting kernel given by the exponentially un-

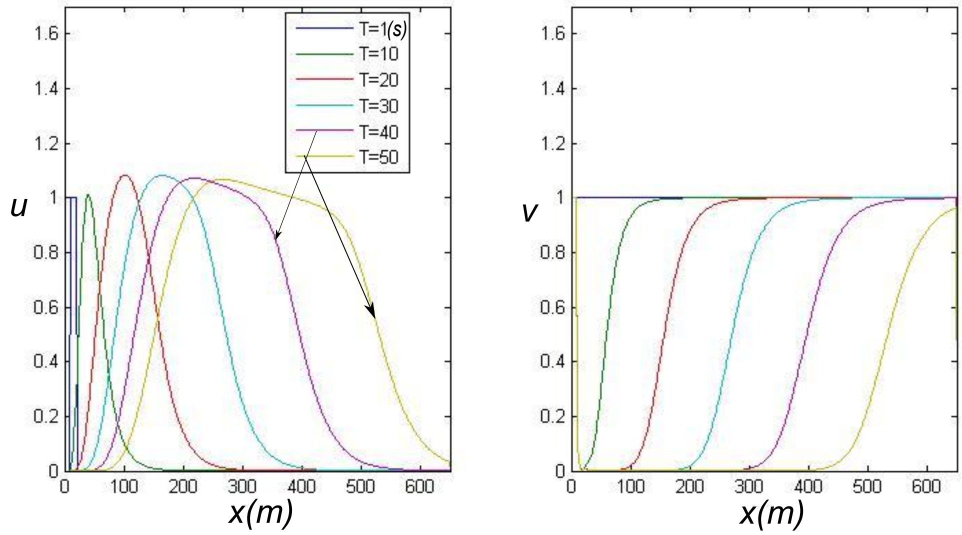

Figure 7.16: Illustration of traveling pulses for the solution to the system (7.19), with dynamics determined by the Arrhenius model (7.21), with exponentially unbounded spotting kernel given in (7.25), with parameter $\lambda = 0.5$. In the left-most graph we plot $u(t)$ versus x for several values of the time t. In the right-most graph we show similar snapshots in time of the total fuel loading fraction $v(t)$ versus x.

bounded kernel (7.25), again choosing $\lambda = 0.5$. The results are plotted in Figure 7.16.

As in the T4-kinetics case, in the left-most graph of Figure 7.16 we observe that the solution $u(t)$ grows into an accelerating wave, whose shape is changing continuously with time. The farthest distance reached at the final time is very similar to that displayed in Figure 7.13, though we see that the amplitude of the solution grows much more rapidly with time. Specifically, the solution $u(t)$ is of greater magnitude, over a much larger spatial extent, relative to the preceding case.

In this case, by comparing subsequent level set for $v(t, x) = 0.6$ in the right-most graph of Figure 7.16, we can see acceleration by noting that these level sets are spreading apart spatially. Further, we have complete combustion in this case, for the time period considered, in contrast to the evolution for the fuel fraction displayed in Figure 7.13. In addition, notice that the shape of the total fuel loading fraction curve is evolving with time, with the transition

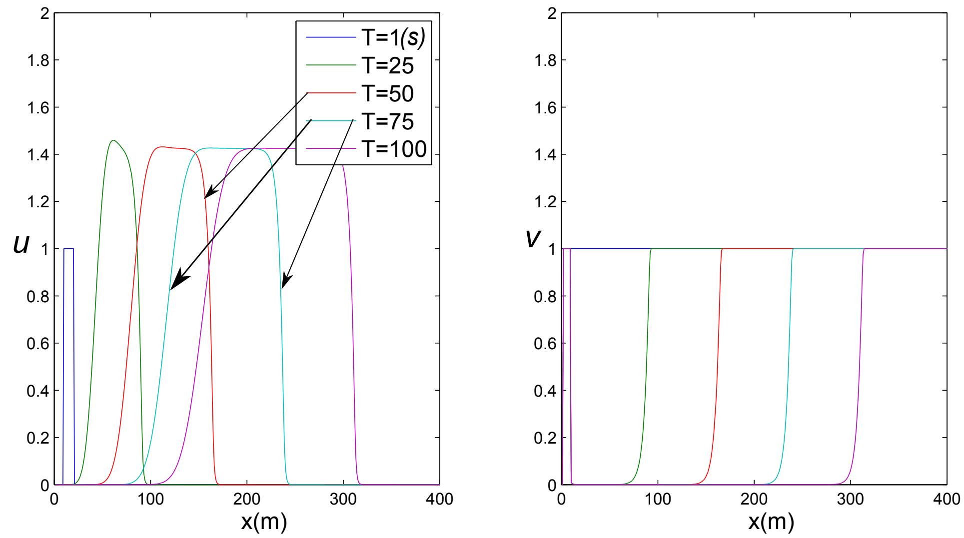

Figure 7.17: Illustration of traveling pulses for the solution to the system (7.19), with dynamics determined by the Arrhenius model (7.22), with uniform spotting kernel given in (7.23). In the left-most graph we plot $u(t)$ versus x for several values of the time t. In the right-most graph we show similar snapshots in time of the total fuel loading fraction $v(t)$ versus x.

from $v = 0$ to $v = 1$ occurring over a larger spatial region.

7.6.7 T3 kinetics, uniform kernel

In these final three subsections, we repeat the steps as in the preceding three subsections, examining solutions to the system (7.19), but now we use the Arrhenius kinetics model T3 as in (7.22). We will again assume throughout that $\alpha = 0.7$, and $d = 0.5$ in (7.19), and $k = 3$ in (7.22).

In this subsection we choose the same spotting kernel as in (7.23), again for the value $L = 5$. We examine such an evolution in Figure 7.17.

In the left-most graph of Figure 7.17 we plot snapshots of $u(t)$ versus x. As in the corresponding T4 and T1 kinetics cases, again the initially compactly supported initial condition for u evolves into a traveling u-pulse, eventually assuming constant shape and speed. The magnitude of the u-pulses are significantly higher in this case relative to the T4 case, but comparable to the peaks displayed for the T1 kinetics, as illustrated in Figures 7.11 and 7.14.

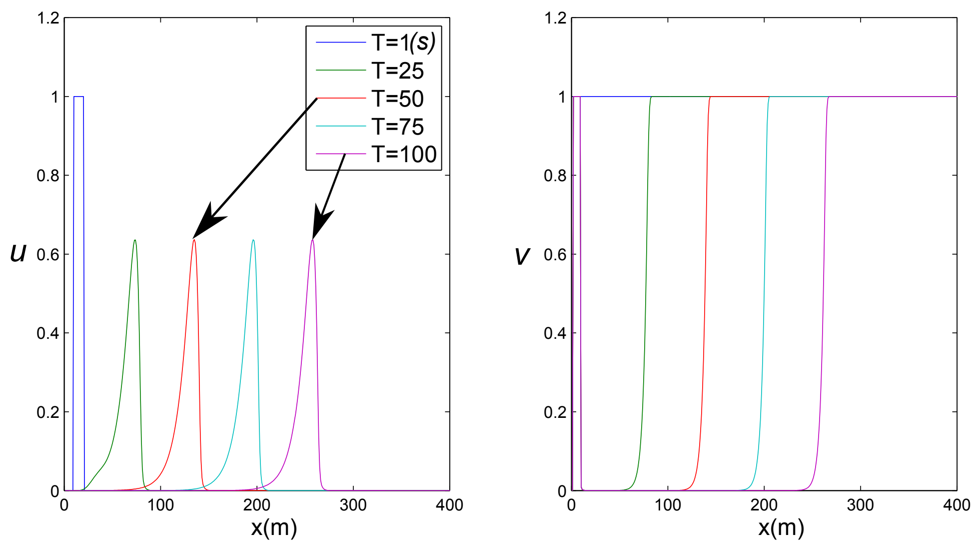

Figure 7.18: Illustration of traveling pulses for the solution to the system (7.19), with dynamics determined by the Arrhenius model (7.22), with exponential spotting kernel given in (7.24). In the left-most graph we plot $u(t)$ versus x for several values of the time t. In the right-most graph we show similar snapshots in time of the total fuel loading fraction $v(t)$ versus x.

The flat-shape for the u-pulses observed in the T1 and T4 cases with the same spotting kernel, are observed in Figure 7.17 after an initial transient.

In right-most graph in Figure 7.17, where we plot snapshots of $v(t)$ versus x, we observe that we have complete combustion as such a wave passes by. The constant speed of the the u-pulse can again be observed by comparing a level set of v between subsequent time steps.

7.6.8 T3 kinetics, exponential kernel

Next, we examine solutions to (7.19), with Arrhenius kinetics T3, and spotting kernel given by the exponential kernel (7.24), again choosing $\lambda = 0.5$. The results are plotted in Figure 7.18.

The evolution for $u(t)$ illustrated in Figure 7.18 is slightly different with these kinetics, compared to the corresponding T4 and T1 kinetics cases, the latter illustrated in Figures 7.11 and 7.15 respectively. We see that the traveling pulses for u are sharper peaked, have greater amplitude, and travel faster

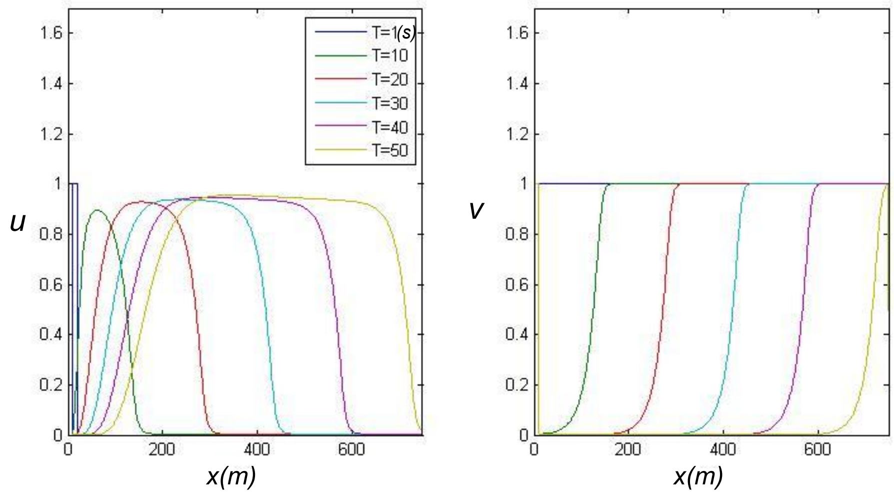

Figure 7.19: Illustration of traveling pulses for the solution to the system (7.19), with dynamics determined by the Arrhenius model (7.22), with exponentially unbounded spotting kernel given in (7.25). In the left-most graph we plot $u(t)$ versus x for several values of the time t. In the right-most graph we show similar snapshots in time of the total fuel loading fraction $v(t)$ versus x.

than in the preceding cases.

The evolution for $v(t)$, illustrated in the right-most graph in Figure 7.18, indicates complete combustion as the u-pulses pass by. This is in contrast to the corresponding fuel fraction evolutions for the corresponding T4 and T1 kinetics cases.

7.6.9 T3 kinetics, fat-tailed kernel: acceleration

Finally, we exhibit solutions to (7.19), with Arrhenius kinetics T3, and spotting kernel given by the exponentially unbounded kernel (7.25), again choosing $\lambda = 0.5$. The results are plotted in Figure 7.19.

The left-most graph for $u(t)$ in Figure 7.19 illustrates a solution $u(t)$, which rapidly evolves to a constant maximum-amplitude traveling pulse. The spatial extent of the wavepeak is widening with time. Further, the spatial extent reached is much greater relative to the corresponding T4 and T1 kinetic models with the same spotting kernels, and the evolution of the waveshape occurs much more rapidly.

The right most graph in Figure 7.19 shows that again we have complete combustion as the fire front passes by. It is more difficult in this case to observe the acceleration from an examination of the snapshots for $v(t)$, relative to the T4 and T1 kinetic cases, though one can observe that the shape of these snapshots is evolving with time.

7.7 Chapter summary

We tested many more scenarios than presented here. The choice of kinetic model T1 (mass action), T2 (non-linear mass action), T3 (Arrhenius) and T4 (logistic) plays an important role, as it changes the form and amplitude of the invasion pulse, and the total fuel loading fraction left behind, both the diffusion-only and spotting dominated cases.

We noticed that for the leading edge, diffusion does not play a role if spotting is significant. So for the purpose of illustration we considered primarily the spotting-dominated case in Chapter 7.6, where we first considered the first model.

In the spotting-dominated case, we found a compactly supported uniform spotting kernel which produced faster advancing waves than an exponentially-decreasing kernel, whereas an exponentially unbounded kernel leads to accelerating pulse-like solutions, in all cases studied. This is important, since most spotting kernels will have compact support, due to the finite lifetimes of the firebrands combustion. The results even with v concerning spreading speeds appear to be qualitatively consistent with the results from Chapter 6.

Chapter 8

Discussion

In the introduction, we formulated several scientific questions which we wished to address in this thesis. These were:

- What is the *spotting distribution*, or the probability of spot fire ignition, downwind of an existing fire front?
- What is the probability that a fire will breach an obstacle to local spread?
- What role does spotting play on the *rate of spread* of a fire front?
- Can spotting *accelerate* a fire's advance?

In Chapter 2, starting from a discrete-time, discrete-space model for local spread and spotting, we derived a new model continuous in space and time, for the expected instantaneous fire probability and the total fuel loading fraction. The full model is an i-PDE system with time delay. We then discussed various simplifications of the model, such as removing the time delay, and ignoring the fuel fraction, the latter resulting in a one-component model for the fire probability. Appearing in the integral term of these models is the spotting distribution, so before proceeding with further analysis, this needed to be determined.

In Chapter 3, we focused on the spotting process of individual firebrands, and introduced a new transport-type model for firebrand transport and combustion. We showed how such a model can be used to determine how a particular vertical launch distribution of firebrands evolves in time, and in particular, determined the firebrand asymptotic landing distribution. In Chapter 4, we reviewed most of the submodels from the literature for firebrand generation, launching, transport, combustion, and ignition.

In Chapter 5, we combined the results from Chapters 3 and 4 to determine a general formula for the spotting distribution. The general formula resulted in an enormous number of possible spotting distributions, depending on the permutations of the various submodels chosen from Chapter 4. We then derived some analytic examples of the spotting distribution, for the purpose of illustration.

Hence in Chapter 5 we finally addressed the first main question of this thesis. The spotting distributions determined in Chapter 5 were determined from an impulse release of firebrands. Physically, we explained how this might result from a fire which reaches a barrier to local spread, but is able to spot along the barrier. Hence the spotting distribution, for each point downwind of the release, in the context of Chapter 5, provides an estimate of the probability that a fire will breach the barrier. We would like to expand upon this problem in future research, since in reality once a local barrier is reached, the fire will launch firebrands for a finite time period prior to its extinction.

Perhaps a more realistic model to address breaching would be to use the full i-PDE model from Chapter 7, with initial conditions for the fire probability non-zero to the left of the barrier; in reality, we do not observe an impulse release as a fire reaches a barrier, but rather the fire launches firebrands for a finite amount of time. The probability of breaching could then be measured by considering the cumulative probability distribution for the instantaneous fire probability, by integrating at each spatial point the instantaneous fire probability against time. Alternatively, the remaining total fuel loading fraction could provide another indicator of the breaching probability.

The final two main questions concerning rates of spread, and acceleration, were addressed in Chapters 6 and 7. In Chapter 6, we performed qualitative analysis for the no-time-delay, one-component i-PDE model for spotting from Chapter 2 (ignoring the evolution of the total fuel loading fraction). We showed that for exponentially bounded kernels, compactly supported initial data for the solution will evolve into a travelling wave with finite speed and fixed shape, and exhibited formulae for these wavespeeds. In addition, in the case of unbounded kernels, we showed no travelling wave solutions exist, but rather we see wave-like accelerating solutions.

In Chapter 7, we addressed the rate of spread and acceleration problem numerically in the context of view of the full model i-PDE system, including now the total fuel loading fraction as a state variable. We presented a number of kinetic models for how combustion can be related to an increase in the fire probability, and then adding diffusion we found a number of travelling pulse solutions.

For the spotting-dominated case, which we found to have essentially the same spreading results as the full model with diffusion, we focused again on a number of kinetic models, and some simple spotting kernels, both exponentially bounded and unbounded. In Section 7.6 in particular, by keeping model parameters the same, we found that the shape, rate of spread, and possibility of acceleration of the travelling pulse-like solutions for u depended on both the kinetics and the spotting kernel. In addition, the remaining fuel fraction after the fire front passes by was qualitatively different depending on the kinetics and spotting kernel, as evidenced by the corresponding snapshots for v.

Several simplifying assumptions were made throughout. For instance, we have neglected the time-delay appearing in the the first i-PDE (2.34) appearing in Chapter 2, in all further discussion. Recall that this time-delay corresponds to the finite travel time it takes, to travel from the launching point above a fire, to landing point somewhere downwind. In the sort of quasi-steady spread states illustrated in the travelling pulses in Chapter 7, perhaps it is more reasonable to neglect the time-delay.

However, there are many other scenarios not considered here where the time-delay could be very important. In addition, we have not considered the time to crowning (and hence spotting) after ignition [40], which could add significantly to the time delay. Ignoring the time delay in such a scenario could lead to erroneous results. In future work we would like to incorporate the time-delay, either in the i-PDE or discrete models presented in Chapter 2, and examine its role in the front's evolution.

Another major assumption is that of homogeneity. While most fire models employ some form of homogenization process (the Fire Behaviour Prediction system does not account for within-stand variability [40]), in reality the fire environment is highly variable in space and time. We have ignored variability in fuel type and loading, topography, and weather, which are amongst the most important factors governing wildfire spread at the macroscopic scale, and are also amongst the most highly variable either in space or time. Fire tends to spread faster upslope, since the radiation emitted by the rising flame is closer to the upslope fuel. In addition, fire tends to spread faster in the direction of prevailing winds. Finally, the rate of spread depends on the type of fuel, which varies spatially. Future work should incorporate heterogeneity in these spread factors.

We have considered only the far-field plume, mostly ignoring the actual flame structure, and the fire-atmosphere interaction. This is more appropriate for highly intense fires, where the convection column rises almost vertically up to the upper bound of the atmospheric boundary layer, since such fires can launch firebrands much higher, and consequently further downwind. The further one moves away from the flame, the more the ambient windflow approximates its fire-free counterpart. Our model may not be appropriate for modelling the spread of smaller scale fires, where the maximum launching height and flame height may be of the same order.

Further, ignoring turbulence and the fire-atmosphere interaction are very strong assumptions. While many efforts have been made to incorporate these factors in other models (see plume models from Chapter 3), we have chosen to ignore them, primarily so that we can obtain analytically tractable models. Existing operational computer models (e.g., [40], [34]) do not include the fire-atmosphere interaction, but rather use a computational fluid dynamics simulator to approximate windflow over fixed topography, accounting only for diurnal variations. Further research efforts should include an approach at modelling the windfield surrounding the fire more accurately, perhaps incorporating Large Eddy Simulations as a necessary component ([16], [83], [84]).

We have also created qualitative models, as opposed to typical transport-type models which are based on conservation of mass, momentum, or energy. We would like these to provide accurate models for the spread of a wildfire's front. To do this, we need to connect our models to data. Fortunately, there is a fair amount of data about a wildfire's local spread, ignoring long-distance spotting events.

There needs to be a direct connection made between the diffusion coefficients appearing in our equations, and the fire's local rate of spread. This could be done by first computing the mean-squared displacement of a point on the front, $< x^2 >$, which was at the origin at time $t = 0$, with the diffusion coefficient D, namely $< x^2 >= 4Dt$, where $t > 0$ is the time. Alternatively, the known rate of spread R (units $\frac{\text{space}}{\text{time}}$) provided by FBP [40], can similarly give the displacement at time t, namely displacement $= R\,t$. We can clearly connect D with R in this way.

Further, the burned crown fraction is an output of the FBP system. This could be connected directly to the remaining total fuel loading fraction after the passage of a fire, and could aid in parameterizing our model kinetics. Also of use would be knowledge of the fire's residence time in a fuel type given a particular spread scenario; we could choose our parameters so that these correspond to one another.

For these results to be used in the field, we need further experimental investigation into the spotting distributions. Our systematic approach outlined in Chapters 4 and 5 allows for the design of controlled experiments, for specific fuel, weather, wind etc., to be able to fit realistic spotting distributions. The spotting distribution could be measured in future prescribed burns, by setting up traps in the region surrounding the fire.

As mentioned earlier, we have only considered firebrands of a single type, while evidence suggests that other firebrand types, like pine cones or Eucalyptus bark, can be very effective firebrands. We have not incorporated the notion of *firebrand type* into the firebrand launching distribution, though this can certainly be done. The absence of experimental data on the generation of these other firebrands makes determining a mass distribution impossible right now, but in the near future it might be possible to incorporate other firebrand types into the model framework.

Finally, perhaps one of the most important applications of the models in this thesis could be to fire spread in the urban environment. There are some natural ways to extend the type of models we've derived to two-dimensions, which would be necessary to accurately model the spread from house to house in an urban environment. Some of the greatest conflagrations in history have been driven by spotting, for example in post-Earthquake fires (see e.g. the excellent review [46] for more details). With the appropriate parameterizations, we could use our models to better describe spread in situations where spotting is important.

Appendix A

Smooth solutions for first-order BVP's and the method of characteristics

A.1 The characteristic equations

Equation (3.11) is an example of a non-linear first-order partial differential equation (PDE). We will denote the solution $p : \mathbb{R}^n \to [0, \infty)$, and its first (classical) derivative by $DP \in \mathbb{R}^n$. In this subsection we will investigate smooth solutions to boundary value problems (BVP) for general first-order PDE's, in the form [33]:

$$F(Dp(x), p(x), x) = 0, \qquad x \in M \subset \mathbb{R}^n, \tag{1.1}$$

subject to the boundary condition:

$$p(x) = g(x), \qquad x \in \partial M. \tag{1.2}$$

We will assume that the function $F : \mathbb{R}^n \times \mathbb{R} \times \mathbb{R}^n \to \mathbb{R}$, the function g and the boundary of M are smooth. The *classical solution* p to the boundary value problem, which we will refer hereafter to as the solution, is a map $p : \overline{M} \to \mathbb{R}$, which:

- Satisfies the boundary condition (1.2).

- Possesses a continuous derivative:

$$Dp := (\frac{\partial p}{\partial x^1}, \frac{\partial p}{\partial x^2}, ..., \frac{\partial p}{\partial x^n}). \tag{1.3}$$

- The map p solves the PDE (1.1) pointwise in M.

The usual strategy for constructing classical solutions is the *method of characteristics*. Let us define a curve parametrically by

$$x(s) := \left(x^1(s), x^2(s), ..., x^n(s)\right), \qquad s \in [0, T]. \tag{1.4}$$

Assuming that p is a twice-continuously differentiable solution of (1.1), we further define:

$$a(s) := p(x(s)), \qquad x \in [0, T], \tag{1.5}$$

as well as:

$$v(s) := Dp(x(s)) = \left(\frac{\partial p}{\partial x^1}(x(s)), \frac{\partial p}{\partial x^2}(x(s)), ..., \frac{\partial p}{\partial x^n}(x(s))\right). \tag{1.6}$$

The *characteristic equations* determine $x(s)$, $a(s)$, and $v(s)$, provided they can be solved [33]. In vector notation (here primes indicate derivatives with respect to the curve parameter s):

$$x'(s) = D_v F(v(s), a(s), x(s)). \tag{1.7}$$

$$a'(s) = D_v F(v(s), a(s), x(s)) \cdot v(s). \tag{1.8}$$

$$v'(s) = -D_x F(v(s), a(s), x(s)) - D_a F(v(s), a(s), x(s)). \tag{1.9}$$

Notice that whenever p is a classical solution to the BVP, and $x(\cdot)$ solves Equation (1.7), then $a(\cdot)$ and $v(\cdot)$ solve Equations (1.8) and (1.9) respectively [33]. Further, if one knows the solutions $x(\cdot)$ and $v(\cdot)$, one sees that (1.8) decouples and may be solved separately from the other equations. The solutions $x(\cdot)$ and $v(\cdot)$ are called the base characteristic curves [33].

The characteristic equations, which form a system of $2n+1$ ordinary differential equations, will possess unique differentiable solutions, given appropriate initial conditions $x(0) := x_0$, $v(0) := v_0$, and $a(0) := a_0$, assuming the vector field on the right hand side in the characteristic equations is at least locally

Lipschitz continuous [33].

Assuming unique solutions to the characteristic equations exist, we will express them in terms of the initial conditions:

$$x(s) := x(s; x_0), \qquad a(s) := a(s; a_0), \qquad v(s) := v(s; v_0). \tag{1.10}$$

It will be useful to introduce the notion of a *solution operator* ψ for each of the characteristic equations. For example, the combustion process for a mass $m(t)$ is discussed at length in Chapter 4, and in particular we introduce the *combustion operator* C which is defined by $C(m_0, t) := m(t; m_0)$, where $m(t; m_0)$ is the portion of the initial mass m_0 remaining at time t.

In the context of this chapter, we introduce the *solution operator* σ for the *spatial* part of the base characteristics, defined by:

$$\sigma(x_0, t) := x(t; x_0). \tag{1.11}$$

When it exists, we define the *inverse solution operator* $\sigma^{-1}(t, x)$ corresponding to the operator defined in (1.11), such that

$$\sigma^{-1}(t, x(t; x_0)) := x_0. \tag{1.12}$$

A.2 Constructing smooth solutions using characteristics

Since by assumption $p = g$ on the boundary ∂M, it is natural to choose initial conditions:

$$a_0 = g(x_0), \qquad x_0 \in \partial M. \tag{1.13}$$

In addition to the previous equations, we require a *compatibility condition* to hold for v_0 [25], namely that the components v_0^i satistfy:

$$v_0^i = \frac{\partial a(x_0)}{\partial x^i}. \tag{1.14}$$

$$F(v_0, a_0, x_0) = 0. \tag{1.15}$$

We note that x_0 and z_0 are determined by the boundary condition (1.2), there is some freedom in our choice of the derivative v_0. A triple of initial conditions (v_0, a_0, x_0) satisfying Equations (1.13) and (1.14) is called *admissible* [33].

We say an admissible triple (v_0, a_0, x_0) is *non-characteristic* if the following holds [33]:

$$\frac{\partial F(v_0, a_0, x_0)}{\partial v} \cdot n(x_0) \neq 0, \tag{1.16}$$

where $n(x_0)$ denotes the unit outward normal to ∂M at x_0.

Remark: Geometrically, Equation (1.16) says that the initial surface is orthogonal to the characteristic curves through (v_0, a_0, x_0).

Remark: The key idea of the method of characteristics is to choose initial conditions for the base characteristics (x_0, v_0) in just this way, so that we may ultimately determine a using Equation (1.8), along the base characteristics, in some neighbourhood of the initial surface ∂M.

Proposition A.1: **([25], Ch. 3.2., Lemma 2)** *Suppose that (v_0, a_0, x_0) is an admissible, non-characteristic triple of initial conditions for the characteristic equations {(1.7), (1.8),(1.9)}.*

Then for every $x_0 \in \partial M$, there exists a neighbourhood $W \subset \mathbb{R}^n$ containing x_0, and an open neighbourhood $V \subset \mathbb{R}^{n-1}$ also containing x_0, with $V \subset \partial M$, such that for every $\tilde{x} \in W$ there exists a unique $s \in [0, T]$ and $y \in V$, for which:

$$\tilde{x} = x(s; x_0 = y), \tag{1.17}$$

and the maps $(s, y) \to x$ are twice-continuously differentiable and invertible.

In other words, we can uniquely determine the solutions to the base characteristic equations locally, for points $y \in V \subset \mathbb{R}^{n-1}$ in some neighbourhood of x_0. The spatial characteristics in this case form a congruence [49] for some neighbourhood of ∂M, such that each point in W lies on exactly one characteristic curve connected to the boundary. This situation is illustrated in Figure 1.1.

One can then define the solution $p(x) = z\,(s(x); y(x))$ for x in some neighbourhood of the boundary ∂M [33]. In this way, the characteristic ODE's,

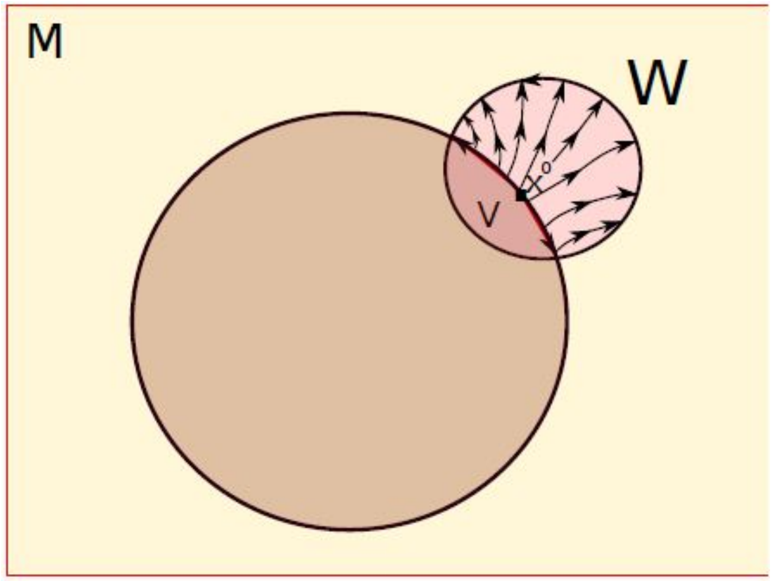

Figure 1.1: Illustration of Proposition A.1, in the planar case. Here M is the plane $\mathbb{R}^2$, excluding the larger disc which is shaded darker in brown, and the boundary ∂M which is the circle bounding the larger disc. The neighbourhood W of x_0 is shown as the smaller circle, shaded in pink. The set V has the same dimension as the boundary, and is denoted by the arrows extending from x_0 parallel to the large circle. The curves with arrows extending from V do not intersect in W, in the case of admissible and non-characteristic boundary data.

equipped with admissible and non-characteristic initial data, allow us to construct a classical solution p for the BVP in some neighbourhood of the boundary. We call the graph of p the integral surface of the PDE (1.1), and with out stated assumptions the integral surface is smoothly embedded in $\mathbb{R}^n$ [49].

This method works up to the first point where the base characteristic curves intersect. At this point, the map $x \to (s, y)$ described in Proposition A.1 is no longer invertible, and our solution $p(x)$ becomes multi-valued [33]. To extend the solution further, we must introduce the notion of a *weak solution* to the BVP, which in general are Lipschitz-continuous mappings, and which may possibly be discontinuous or possess discontinuous derivatives. Weak solutions are discussed in detail in [33].

Remark: To illustrate the method of characteristics in the simplest case, consider an initial value problem for a density $p : \mathbb{R}^2 \to \mathbb{R}$, and constant

$c > 0$:

$$\frac{\partial p}{\partial t}(x,t) + c\frac{\partial p}{\partial x}, \qquad x \in \mathbb{R}. \tag{1.18}$$

The x-characteristic equation gives $\dot{x} = c$, which has solution $x(t) = x_0 + ct$. The momentum characteristic equation provides no information. The characteristic equation for $Z(t) := p(t, x(t)$ gives $Z' = 0$, so that the solution is constant along characteristics. In this case the curve $t = 0$ carries information contained in the initial condition $f(x)$, with speed c, into the region $t > 0$.

The solution to the IVP, with $u(x, 0) = f(x)$, is given by

$$u(x,t) = f(x - ct), \qquad x \in \mathbb{R}, t \geq 0. \tag{1.19}$$

i.e. the graph of the initial condition $u(x, 0)$ is translated to the right with time, with speed c.

Appendix B

Essentials of semigroup theory

This section serves to introduce notation and a variety of preliminary mathematical results, which will be used in Chapter 6 to discuss solutions to the iPDE models from Chapter 2.

B.1 The Lebesgue spaces L^p

For the first four subsections we take definitions and notation from [71]. First of all, we introduce the space $C^0(\Omega)$ of continuous real-valued functions $f : \Omega \longrightarrow \mathbb{R}$, where $\Omega \subset \mathbb{R}^n$ is a bounded open set with smooth boundary. This space is a Banach space when equipped with the supremum norm $||\cdot||_\infty$

$$||f||_\infty := \max_{x\in\bar{\Omega}} |f(x)|. \tag{2.1}$$

We say a function $f \in C^0(\Omega)$ has compact support in Ω if there is some compact set $K \subset \Omega$ such that $f(x) = 0$ for x in the complement of K. In particular, $f(x) = 0$ for $x \in \partial\Omega$. We define the space of continuous, compactly supported functions on Ω:

$$C_c^0(\Omega) =:= \{f \in C^0(\Omega) | \exists K \subset\subset \Omega, f(x) = 0 \;\text{ if }\; x \notin K\}, \tag{2.2}$$

where the notation $K \subset\subset \Omega$ means K is a compact subset of Ω.

One can then define a new space $L^p(\Omega)$, for $1 \leq p < \infty$, as the completion of $C_c^0(\Omega)$ in the metric topology induced by the functional (7.1.2). This means any element $f \in L^p(\Omega)$ can be approximated arbitrarily closely by a sequence

$\phi_n \in C_c^0(\Omega)$, such that $||\phi_n - f||_p \longrightarrow 0$ as $n \longrightarrow \infty$. The L^p spaces are Banach spaces when equipped with the $||\cdot||_p$ norm.

A special case is $L^\infty(\Omega)$, which is a Banach space when equipped with the sup norm $||\cdot||_{L^\infty}$:

$$||f||_{L^\infty} = \operatorname*{ess\,sup}_{x \in \Omega} |f(x)| \tag{2.3}$$

Of particular interest in our study is the space $L^2(\Omega)$, which is a complete inner product space, or Hilbert space, when equipped with the following inner product $< \cdot, \cdot >$: $L^2(\Omega) \times L^2(\Omega) \longrightarrow \mathbb{R}$:

$$< f, g >= \int_\Omega f(x)g(x)dx. \tag{2.4}$$

B.2 The Sobolev spaces $W^{k,p}$

We will also be interested in the Sobolev spaces $W^{k,p}$. In order to introduce these spaces, one must first develop the notion of the weak derivative.

It is helpful to introduce the multi-index vector α consisting of natural numbers $\alpha = (\alpha_1, \alpha_2, ...\alpha_m)$, and we write $|\alpha| = \alpha_1 + \alpha_2 + ... + \alpha_m$. We can represent the partial derivatives of all orders for a smooth function f by

$$D^\alpha f = \frac{\partial^{|\alpha|} f}{\partial x_1^{\alpha_1} \cdots \partial x_m^{\alpha_m}}. \tag{2.5}$$

With this definition, we introduce the space $C^r(\Omega)$,

$$C^r(\Omega) = \{f : \Omega \longrightarrow \mathbb{R} | D^\alpha f \in C^0(\Omega), |\alpha| \leq r\}. \tag{2.6}$$

From the latter spaces we can define the smooth functions $C^\infty(\Omega)$, by

$$C^\infty(\Omega) = \bigcap_{r=0}^{\infty} C^r(\Omega). \tag{2.7}$$

More importantly, we are interested in a subset of (7.1.3) of functions with compact support in Ω, $C_c^\infty(\Omega)$, which we will refer to as test functions:

$$C_c^\infty(\Omega) = \{f \in C^\infty(\Omega) | \exists K \subset\subset \Omega, f(x) = 0 \quad \text{if} \quad x \notin K\}. \tag{2.8}$$

To introduce the weak derivative, we first introduce a subset of $L^p(\Omega)$ which are locally integrable, that is integrable on every compact subset $K \subset\subset \Omega$:

$$L^p_{loc}(\Omega) := \{f|f \in L^p(K), \forall K \subset\subset \Omega\}. \tag{2.9}$$

For a given function $u \in L^1_{loc}(\Omega)$, we say that v is the weak derivative of u with respect to the coordinate x_j , written $v = D_j u$, if $v \in L^1_{loc}(\Omega)$ and

$$\int_\Omega v\phi dx = -\int_\Omega u \frac{d\phi}{dx_j} dx, \tag{2.10}$$

holds $\forall \phi \in C_c^\infty(\Omega)$.

The latter formula results from the integration by parts in the x_j variable, and the fact that $\phi = 0$ on $\partial\Omega$. We can similarly define higher-order weak derivatives: if $u, v \in L^1_{loc}(\Omega)$, then v is the α^{th} weak derivative of $u, v = D^\alpha u$, if:

$$\int_\Omega v\phi dx = \int_\Omega (-1)^{|\alpha|} u D^\alpha \phi dx, \tag{2.11}$$

holds $\forall \phi \in C_c^\infty(\Omega)$.

We are now in the position to define the Sobolev spaces $W^{k,p}$, where the expression $D^\alpha u$ refers to the weak derivative of u as in (2.11):

$$W^{k,p} := \{u|D^\alpha u \in L^p(\Omega), 0 \leq |\alpha| \leq k\}, \tag{2.12}$$

with norms,

$$||u||_{W^{k,p}} := \sum_{0 \leq |\alpha| \leq k} \{||D^\alpha u||^p_{L^p}\}^{1/p}. \tag{2.13}$$

These spaces are Banach spaces, and of particular interest is the case $p = 2$. We will introduce the notation

$$H^k(\Omega) := W^{k,2}(\Omega) = \{u|D^\alpha u \in L^2(\Omega), \forall 0 \leq |\alpha| \leq k\}. \tag{2.14}$$

The spaces H^k are Hilbert spaces when equipped with the inner product

$$((u, v))_{H_k} := \sum_{0 \leq |\alpha| \leq k} < D^\alpha u, D^\alpha v >, \tag{2.15}$$

where $< \cdot, \cdot >$ denotes the L^2-inner product.

It turns out that $C_c^\infty(\Omega)$ is not dense in $H^k(\Omega)$, so we define the completion of the test functions with respect to the H^k-norm, denoted $H_0^k(\Omega)$. In particular we are interested in $H_0^1(\Omega)$

$$H_0^1(\Omega) := \{u \in H^1(\Omega) | Tu = 0\}, \tag{2.16}$$

where T is the "trace operator", which for functions $u \in H^1 \bigcap C^0(\Omega)$, we have $Tu = u_{\partial\Omega}$. In essence, what this technical definition tells us is that $H_0^1(\Omega)$ is the subset of H^1 which vanishes on the boundary of.

B.3 The dual space of important function spaces

We recall here some important facts concerning the dual space X^* of a Banach space X. The dual space is the space of continuous real-valued mappings on X. The dual space X^* is a Banach space itself, when equipped with the operator norm:

$$||L||_{X^*} = \sup_{x \neq 0} \frac{||Lx||_X}{||x||_X}. \tag{2.17}$$

The dual space of $L^p(\Omega)$ is $L^q(\Omega)$, where p and q are said to be conjugate, i.e. $1/p + 1/q = 1$. In particular, the Hilbert space $L^2(\Omega)$ is its own dual space. The cases L^1 and L^∞ must be handled separately.

We will be interested in the dual space to the Sobolev space H_0^k defined in (7.1.3). We define:

$$(H_0^k)^* := H^{-k}. \tag{2.18}$$

B.4 Banach-space valued functions

In the context of time-evolution problems like the one we are considering, we must discuss Banach-space valued functions. Suppose I is some interval in the real line, and X is a Banach space. Then we define the space of continuous functions from I into X,

$$C^0(I,X) := \{u(t) : I \longrightarrow X \mid u(t) \longrightarrow u(t_0) \ \text{ in } \ X \ \text{ as } \ t \longrightarrow t_0\}, \tag{2.19}$$

where convergence in X is understood with respect to the norm.

On this space we can define the functional

$$||u||_{L^p(I,X)} := \left(\int_I ||u(t)||_X^p dt\right)^{\frac{1}{p}}. \tag{2.20}$$

We can then define the space $L^p(I,X)$ as the completion of $C^0(I,X)$ with respect to the norm defined in (7.1.5), and it is a Banach space when equipped with this norm.

We will also be interested in the dual spaces to these function spaces. For example, if $I = (0,T)$, we have

$$(L^p(0,T;L^r(\Omega))^* = L^q(0,T;L^s(\Omega))), \tag{2.21}$$

where both (p,q) and (r,s) are conjugate indices.

Of extreme importance are the Sobolev spaces for Banach-space valued functions. For example, we can define

$$H^1(0,T;L^2(\Omega)) := \{u \in L^2(0,T;L^2(\Omega)) | Du \in L^2(0,T;L^2(\Omega))\} : \tag{2.22}$$

B.5 Semigroups of bounded linear operators

The existence, uniqueness, and continuous dependence on initial conditions for solutions to initial value problems, as considered in Chapters 2 and 4, for an appropriate function space V, allows us to define the notion of a solution operator $\Psi(t)$ to an IVP:

$$\Psi(t)u_0 := u(t;u_0), \tag{2.23}$$

where $u(t;u_0)$ is the unique solution to the IVP with initial condition $u_0 \in V$, at time $t > 0$.

We will be particularly interested in families of solution operators $\{\psi(t)\}_{t\geq 0}$ which form a so-called *strongly continuous semigroup of bounded linear operators.*

Definition: ([65], Definition 2.1) Let X be a Banach space. A one parameter family $\{T(t)\}$, $0 \leq t < \infty$ of bounded linear operators from X into itself is a *strongly continuous*, or a C_0 semigroup of bounded linear operators on X, if:

- $T(0) = I$, where I is the identity operator on X.
- $T(t+s) = T(t)\,T(s)$, for all $t, s \geq 0$.
- $\lim_{t\to 0^+} T(t) = x$, for all $x \in X$.

Also important is the idea of the *infinitesimal generator* A of a C_0 semigroup, formally defined by [32]:

$$Ax := \lim_{h\to 0^+} (T(h)x - x), \qquad x \in D(A), \tag{2.24}$$

with domain $D(A)$ given by:

$$D(A) := \{x \in X \mid t \to T(t)x \text{ is differentiable}\}. \tag{2.25}$$

The connection to our differential equation problem is that the existence, uniqueness, and continuous dependence on initial conditions in $L^2(\Omega)$ for reaction-diffusion equations, defines a strongly continuous semigroup on $L^2(\Omega)$: $(\psi(t))_{t\geq 0}$, which provides us with the unique solution $\psi(t)u_0 = u(t; u_0)$ to the abstract Cauchy problem $u_t = Au + f(u)$ with $u(0) := u_0 \in L^2(\Omega)$, where A is the abstract operator associated with the Laplacian operator in $\mathbb{R}^n$, defined later in this appendix.

To use this abstract framework for our iPDE spotting model, in the next subsection we investigate properties of integral operators.

B.6 Boundedness of integral operators

This subsection is based on Chapter 16 from the manuscript by Lax [48]. Let X and Y be Banach spaces. We define the integral operator $\mathcal{K} : X \to Y$

$$\mathcal{K}(f)(x) := \int_X K(x,y)f(y)dy, \qquad f \in X, \tag{2.26}$$

where the integral is taken with respect to Lebesgue measure. The mapping $K : Y \times X \to \mathbb{R}$ appearing in Equation (2.26) is called the *kernel* of $\mathcal{K}$.

We will determine conditions on f and K so that the integral (2.26) defines a measurable function on Y.

Theorem B.1: *([48], Theorem 16.1.1) The map $\mathcal{K}$ defined in (2.26) is bounded:*

- *As a mapping $L^1(X) \to L^\infty(Y)$, provided:*

$$||\mathcal{K}|| \leq ess\sup_{x,\, y} |K(x,y)| < \infty. \tag{2.27}$$

- *As a mapping $L^\infty(X) \to L^1(Y)$, provided:*

$$||\mathcal{K}|| \leq \int_Y \int_X |K(x,y)| dx\, dy < \infty. \tag{2.28}$$

- *As a mapping $L^1(X) \to L^1(Y)$, provided:*

$$||\mathcal{K}|| \leq ess\sup_{y} \int_X |K(x,y)| dx < \infty. \tag{2.29}$$

- *As a mapping $L^\infty(X) \to L^1(Y)$, provided:*

$$||\mathcal{K}|| \leq ess\sup_{x} \int_Y |K(x,y)| dy < \infty. \tag{2.30}$$

Further, when the kernel K is nonnegative, the sign of equality holds in the first inequalities of (2.29) and (2.30), respectively.

Of particular interest is the L^2-case.

Theorem B.2: *([48], Theorem 16.1.2), The map $\mathcal{K}$ is bounded $L^2(X) \to L^2(Y)$ provided:*

$$||\mathcal{K}||^2_{L^2(X\times Y)} \leq \int_Y \int_X |K(x,y)|^2 dx\, dy < \infty. \tag{2.31}$$

The inequality (2.31) is due to Hilbert and Schmidt, and operators $\mathcal{K}$ satisfying this inequality are called *Hilbert-Schmidt* operators.

A second inequality due to Holmgren ensures $\mathcal{K}$ is bounded in the L^2-case:

Theorem B.3: *([48], Theorem 16.1.3), The map $\mathcal{K}$ is bounded $L^2(X) \to \mathbb{L}^2(Y)$, provided:*

$$\left(\sup_x \int |K(x,y)|dy\right)^{1/2} \left(\sup_y \int |K(x,y)|dy\right)^{1/2} < \infty. \tag{2.32}$$

We should point out that there are several important integral operators, namely the Fourier and Laplace transforms, which despite not satisfying either of these inequalities are nevertheless bounded from L^2 to L^2.

B.7 The Bounded Perturbation Theorem

In this subsection we investigate bounded perturbations of strongly continuous semigroups of bounded linear operators. As a preliminary result towards the main theorem of this subsection, we require a Lemma:

Lemma B.1: *([32], Prop. 1.5.5) For every C_0 semigroup $(T(t))_{t\geq 0}$, there exists constants $w \in \mathbb{R}$ and $M \geq 1$ such that:*

$$||T(t)|| \leq Me^{wt}, \quad t \geq 0. \tag{2.33}$$

So, without loss of generality, we may always assume strongly continuous semigroups possess constants w and $M \geq 1$, which appear in the following Theorem:

Theorem B.4: *([65], Thm. 3.1.1) Let X be a Banach space and let A be the generator of a C_0 semigroup $(T(t))_{t\geq 0}$ on X, satisfying $||T(t)|| \leq Me^{wt}$. If B is a bounded linear operator on X, then $A + B$ is the generator of a C_0 semigroup $S(t)$ on X, satisfying $||S(t)|| \leq Me^{(w+M||B||)t}$.*

B.8 The initial value problem for reaction-diffusion equations in an open bounded domain

Our goal is to investigate the existence and uniqueness problem for non-linear reaction-diffusion equations. We will then perturb these equations with an integral term, and use techniques from semigroup theory to argue well-posedness for the model (2.34) below. In this subsection and the next we follow closely the arguments and assumptions presented in [71].

The scalar reaction-diffusion equation for a density $u : \Omega \subset \mathbb{R}^{\ltimes} \times [0,T] \longrightarrow \mathbb{R}$ is an equation of the form

$$\frac{\partial u(x,t)}{\partial t} = \Delta u(x,t) + f(u(x,t)), \quad x \in \Omega, \quad t \in [0,T]. \tag{2.34}$$

Here, $\Delta u(x,t) = \nabla \cdot \nabla u(x,t)$ is the Laplacian, i.e. the divergence of the gradient of u, and $f(u)$ is a birth/death term.

The domain $\Omega \subset \mathbb{R}^n$ is an open, bounded domain with smooth boundary, and we prescribe homogeneous Dirichlet boundary conditions for the solutions $u(x,t)$, for values of x in the boundary of the domain $\partial\Omega$

$$u(x,t) = 0, \quad x \in \partial\Omega, \quad t \in [0,T]. \tag{2.35}$$

We also require an initial condition,

$$u(x,0) := u_0(x). \tag{2.36}$$

Following the argument in Robinson [71], we will view $u(x,t)$ as a trajectory in a Banach space, regarding $u(\cdot,t)$ as a sequence of functions $u(t)$, each defined on Ω, such that

$$u(t)(x) = u(x,t), \quad u(t) : \Omega \longrightarrow \mathbb{R}. \tag{2.37}$$

It will be important to characterize the various Banach spaces in which both the initial condition $u_0(x)$, as well as the various solutions $u(t)$ reside.

B.9 Weak solutions to reaction-diffusion equations

We now return to the equation (2.34), together with boundary conditions (2.35), and initial conditions (2.36). Multiply the PDE by a test function $\phi \in C_c^\infty(\Omega)$, and integrate:

$$\int_\Omega \phi(x)\frac{\partial u(x,t)}{\partial t}dx - \int_\Omega \phi(x)\Delta u(x,t)dx = \int_\Omega \phi(x)f(u(x,t))dx \tag{2.38}$$

We now use integration by parts on the second term, to obtain

$$\int_\Omega \phi(x)\frac{\partial u(x,t)}{\partial t}dx - \int_\Omega \nabla\phi(x)\cdot\nabla u(x,t)dx = \int_\Omega \phi(x)f(u(x,t))dx. \tag{2.39}$$

From the second term we can define a bilinear form $a(u,\phi)$,

$$a(u,\phi) = \int_\Omega \nabla\phi(x)\cdot\nabla u(x,t)dx. \tag{2.40}$$

For each $u \in L^2(\Omega)$, the map

$$v \longrightarrow a(u,v) \tag{2.41}$$

is a linear functional on $L^2(\Omega)$, since if one assumes $v \in L^2(\Omega)$, we have

$$|a(u,v)| = |< u,v >| \leq ||u||_{L^2}||v||_{L^2}, \tag{2.42}$$

the final inequality following from the Cauchy-Schwarz inequality.

It follows that one can define a linear operator $A : L^2(\Omega) \longrightarrow (L^2(\Omega))^*$, by

$$< Au, v >= a(u,v), \tag{2.43}$$

for all $v \in L^2(\Omega)$. It can also be shown that A defines a bounded operator from H_0^1 into its dual H^{-1}.

Further, the nonlinear term in (2.34) defines a linear functional on $\phi \in C_c^\infty(\Omega)$, for fixed f, defined by $[f(u(t))](x) := f(u(x,t))$ (see the discussion leading up to (2.37), namely

$$\int_\Omega \phi(x) f(u(x,t))dx =< f(u(t)), \phi >:=< f(u), \phi > . \tag{2.44}$$

The density of $C_c^\infty(\Omega) \subset H_0^1$ allows us to define $< f, \phi >$ for $f \in H^{-1}$ and $\phi \in H^1$. In this case the notation $< f, \phi >$ denotes the action of the functional f on the function ϕ in the abstract, and not L^2-sense.

To deal with the first term in (2.34), we weaken the condition that $\frac{du}{dt}$ exists as a continuous function, and define the weak derivative $\frac{du}{dt}$.

$$\int_0^T \frac{du}{dt}\phi(t)dt = -\int_0^T u(t)\frac{d\phi(t)}{dt}, \tag{2.45}$$

for test functions $\phi \in C_c^\infty([0,T], \mathbb{R})$.

Putting all of this together, we can rewrite (2.34) as:

$$< \frac{du}{dt}, \phi > + < Au, \phi >=< f(u), \phi >, \tag{2.46}$$

for all $\phi \in C_c^\infty(\Omega)$. The density of $C_c^\infty(\Omega) \subset H_0^1$ allows us to rephrase the latter (2.46) as equality for all $\phi \in H_0^1$.

We can re-express the PDE (2.34) as an abstract operator equation,

$$\frac{du}{dt} + Au = f(t). \tag{2.47}$$

where equality holds in $L^2(0,T;H^{-1})$. The operator $A = -\Delta$ is the Laplacian equipped with Dirichlet boundary conditions. We are now prepared to state our main result:

Theorem B.5: *([71] Robinson Theorem 8.4)*

Suppose f is a C^1 function satisfying

$$-k - \alpha_1|s|^p \leq f(s)s \leq k - \alpha_2|s|^p, f'(s) \geq\sim l, p > 2, \tag{2.48}$$

Then the IBVP for (2.34) with Dirichlet boundary conditions has a unique weak solution: for any $T > 0$, given an initial condition $u(x,0) = u_0(x) \in L^2(\Omega)$ there exists a solution u with

- $u \in L^2(0,T;H_0^1(\Omega)) \bigcap L^p(0,T;L^p(\Omega))$.

- *$u \in C^0(0, T; L^2(\Omega))$.*
- *The map $u_0 \longrightarrow u(t)$ is continuous on $L^2(\Omega)$.*
- *Equation (7.1.6) holds as equality in $L^q(0, T; H^{-s})$, where q is conjugate to p in (7.1).*

B.10 The Fourier transform and the heat equation on $\mathbb{R}^n$

In this subsection we investigate the Cauchy problem for the heat equation on $\mathbb{R}^n$, defined by

$$\frac{\partial u(x,t)}{\partial t} = \Delta u(x,t), \quad x \in \mathbb{R}^n, \quad t \in [0,T]. \tag{2.49}$$

with initial conditions $u(x, 0) := u_0(x)$.

This problem requires different methods than the bounded domain case considered in the previous section. Unless otherwise specified, the discussion and results in this subsection were obtained from Chapter 3 of [85].

For unbounded domains, the *Schwartz space* plays an analogous role to the space of test functions $C_c^\infty(\Omega)$ in the bounded case. The *Schwartz space* $Y(\mathbb{R}^n)$ of rapidly decreasing functions is defined by:

$$Y(\mathbb{R}^n) := \{u \in C^\infty(\mathbb{R}) \mid x^\beta D^\alpha u \in L^\infty(\mathbb{R}^n), \forall \alpha, \beta \geq 0\}, \tag{2.50}$$

where $x^\beta := x_1^{\beta_1} ... x_n^{\beta_n}$, $D^\alpha = D_1^{\alpha_1} ... D_n^{\alpha_n}$, with $D_j := \frac{\partial}{\partial x_j}$.

The Schwartz spaces are intimately connected to the Fourier transform $\mathcal{F}$, defined by

$$\mathcal{F}f(s) = \hat{f}(s) = (2\pi)^{-n/2} \int_{\mathbb{R}} f(x) \exp{(-ix \cdot s)} dx. \tag{2.51}$$

We define the inverse Fourier transform $\mathcal{F}^*$ by

$$\mathcal{F}^* f(x) = (2\pi)^{-n/2} \int f(x) \exp{(ix \cdot s)} dx. \tag{2.52}$$

On the Schwartz space, we have the Fourier inversion formula $\mathcal{F}^*\mathcal{F} = \mathcal{F}\mathcal{F}^* = I$. One can show that both $\mathcal{F}$ and $\mathcal{F}^*$ extend uniquely to isometries on $L^2(\mathbb{R}^n)$, and are there inverses of each other. Fourier analysis is an essential tool in investigating PDE's on unbounded domains.

We can equip $Y(\mathbb{R}^n)$ with a topology. We start with the seminorms

$$p_k(u) := \sum_{|\alpha|\leq k} \sup_{x\in\mathbb{R}^n} |D^\alpha u(x)|. \tag{2.53}$$

The distance function

$$d(u,v) := \sum_{k=0}^{\infty} \frac{p_k(u-v)}{1+p_k(u-v)} \tag{2.54}$$

then makes $Y(\mathbb{R}^n)$ into a complete metric space.

We can then talk about continuity of maps $L : Y(\mathbb{R}^n) \to \mathbb{R}$. It is necessary and sufficient that there exists k, C, such that

$$|< u, l >| \leq C p_k(u), \quad \forall u \in Y(\mathbb{R}^n). \tag{2.55}$$

The space of *temperered distributions*, denoted $Y'(\mathbb{R}^n)$, is the set of all continuous linear functionals on the Schwartz space. In the space of tempered distributions we have the weak* topology, in which we say a sequence $L_n \in Y'(\mathbb{R}^n)$ converges weak* to w if $< u, L_n > \to < u, w >$ for all $u \in Y(\mathbb{R}^b)$.

Now consider the IVP for Equation (2.49), with $f \in Y'(\mathbb{R}^n)$. We seek smooth solutions $u \in C^\infty([0,T]; Y'(\mathbb{R}^n))$.

Of primary importance is the *fundamental solution* $G(x,t)$, defined for $t > 0$ by

$$G(x,t) = (4\pi t)^{-n/2} e^{-\frac{|x|^2}{4t}}. \tag{2.56}$$

We can use the fundamental solution (2.56) to construct the solution to the IVP, using convolution:

$$u(x,t) = (G(\cdot,t) * u_0)(x). \tag{2.57}$$

Further, if $f \in L^p(\mathbb{R}^n)$, then the solution $u \in C^0([0,T]; L^p(\mathbb{R}^n))$ for all $T > 0$.

B.11 The heat semigroup on $\mathbb{R}^n$

In this section we consider the family of operators $T(t)$ defined on $L^p(\mathbb{R}^n)$, which are the solution operators for the hear equation, written in terms of the fundamental solution G:

$$\begin{aligned} T(t)f(x) &:= (G(x,t) * f(x))(x) \\ &= (4\pi t)^{-n/2} \int_{\mathbb{R}^n} e^{-\frac{|x-r|^2}{4t}} f(r) dr, \end{aligned} \tag{2.58}$$

for $t > 0$, $x \in \mathbb{R}^n$, and $f \in L^p(\mathbb{R}^n)$.

Theorem B.6: *([32], E.g. 2.13) If we define $T(0) := I$, then the family $(T(t))$ defined in (2.58) forms a strongly continuous semigroup of operators on $L^p(\mathbb{R}^n)$. The generator A coincides with the closure of the Laplace operator on the Schwartz space.*

Bibliography

[1] S. Ai and W. Huang. Travelling wavefronts in combustion and chemical reaction models. *Proc. Royal Soc. Edinburgh*, 137A:671–700, 2007.

[2] F. A. Albini. Spot fire distance from burning trees - a predictive model. Technical report, Intermountain Forest and Range Experiment Station, Ogden, Utah, USDA For. Serv. Gen. Tech. Rep. INT-56, 1979.

[3] F. A. Albini. Transport of firebrands by line thermals. *Combust. Sci. Technol.*, 32:277–288, 1983.

[4] M. E. Alexander, C. Tymstra, and K.W. Frederick. Incorporating breaching and spotting considerations into PROMETHEUS, the Canadian wildland fire growth model. Technical report, Foothills Model Forest, Hinton, Alberta, Canada, 2004.

[5] M.E. Alexander and M. G. Cruz. Evaluating a model for predicting active crown fire rate of spread using wildfire observations. *Can. J. For. Res.*, 36:3015–3028, 2006.

[6] M.B. Allen and E.L. Isaacson. *Numerical Analysis for Applied Science.* John Wiley and Sons, 1st edition, 1998.

[7] W. Alt, S. Dunbar, and H. Othmer. Models of dispersal in biological systems. *J. Math. Biol.*, 26:263–298, 1988.

[8] D.H. Anderson, E.A. Catchpole, N.J de Mestre, and T. Parkes. Modelling the spread of grass fires. *J. Aust. Math. Soc. (Ser. B)*, 23:451–466, 1982.

[9] D. Aronson. The asymptotic speed of propagation of a simple epidemic. In W. Fitzgibbon and H. Walker, editors, *Nonlinear Diffusion, Res. Notes Math. 14*, pages 1–23. Pitman, London, 1977.

[10] D.G. Aronson and H.F. Weinberger. Nonlinear diffusion in population genetics, combustion, and nerve pulse propagation. In J.A. Goldstein, editor, *Partial Differential Equations and Related Topics*, pages 5–49. Lecture Notes in Mathematics, No. 466, Springer-Verlag, Heidelberg/Berlin, 1975.

[11] P. Babak, A. Bourlioux, and T. Hillen. The effect of wind on the speed of propagation of an idealized forest fire. *SIAM J. Appl. Math*, 70(4):1364–1388, 2009.

[12] P. Babak and T. Hillen. A probabilistic model for wildfre spread. Private correspondence.

[13] V. Babrauskas. Heat release rates. Technical report, National Fire Protection Association: Quincy, MA, 2002.

[14] J. Barber, C. Bose, A. Bourlioux, J. Braun, E. Brunelle, T. Garcia, T. Hillen, and B. Ong. Burning issues with prometheus, the Canada's wildfire growth simulator. *Canad. Appl. Math. Quart.*, 16(4):337–378, 2008.

[15] H.R. Baum and B.J. McCaffrey. Fire induced flow field - theory and experiment, fire safety science. Technical report, Hemisphere Washington, D.C., 1983.

[16] S. Bhutia, M.A. Jenkins, and R. Sun. Comparison of firebrand propagation by a plume model and a coupled-fire/atmosphere large-eddy simulator. *J. Adv. Model. Earth Syst.*, 2, 2009.

[17] W. H. Blackmarr. Moisture content influences ignitability of slash pine litter. Technical report, USDA Forest Service South-Eastern Forest Experimental Station, 1972.

[18] D. Boychuk, W.J. Braun, R.J. Kulperger, Z.L. Krougly, and D.A. Stanford. A stochastic model for forest fire growth. *INFOR*, 45:9–16, 2008.

[19] N.F Britton. *Reaction-Diffusion Equations and Applications to Biology.* Academic Press Inc., 1986.

[20] G. Byram. *Combustion of Forest Fuels.* New York: McGraw Hill, 1959.

[21] D. Cioranescu and P. Donato. *An Introduction to Homogenization.* Oxford University Press, New York, 1999.

[22] T. Clark, J. Coen, and D. Latham. Description of a coupled atmosphere-fire model. *Int. J. Wildland Fire*, 13:49–63, 2004.

[23] T. Clark, M.A. Jenkins, J. Coen, and D. Packham. A coupled atmospheric-fire model: convective feedback on fire line dynamics. *J Applied Meteorology*, 35:875–901, 1996.

[24] T. Clark, M.A. Jenkins, J. Coen, and D. Packham. A coupled atmospheric-fire model: convective Froude number and dynamic fingering. *Int J Wildland Fire*, 6:177–190, 1996.

[25] W.H. Cottrell. *The book of fire.* Mountain Press Pub., 2004.

[26] M.G. Cruz and M.E. Alexander. Assessing crown fire potential in coniferous forests of western north america: a critique of current approaches and recent simulation studies. *Int. J Wildland Fire*, 19:377–398, 2010.

[27] P. Cunningham, S.L. Goodrick, M.Y. Hussaini, and R.R. Linn. Coherent vertical structures in numerical simulations of buoyant plumes from wildland fires. *Int. J Wildland Fire*, 14:61–75, 2005.

[28] P. Cunningham and R.R. Linn. Numerical simulations of grass fires using a coupled atmosphere-fire model: Dynamics of fire spread. *J Geophys. Research*, 112:D05108, 2007.

[29] W.M. Deen. *Analysis of Transport Phenomena.* Oxford University Press, New York, 1998.

[30] O. Diekmann. Run for your life. a note on the asymptotic speed of propagation of an epidemic. *J. Diff. Eqns.*, 33:58–73, 1979.

[31] P. Ellis. *The aerodynamic and combustion characteristics of eucalypt bark - a firebrand study.* PhD thesis, Australian National University, 2000.

[32] K.J. Engel and R. Nagel. *One-Parameter Semigroups for Linear Evolution Equations.* Springer-Verlag, New York, 2000.

[33] L.C. Evans. *Partial Differential Equations.* AMS Press, 1998.

[34] M.A. Finney. Farsite: Fire area simulator - model development and evaluation. Technical report, USDA Forest Service, 2004.

[35] R.A. Fisher. The wave of advance of advantageous genes. *Ann. Eugenics*, 7:335–369, 1937.

[36] J. Garnier. Accelerating solutions in integro-differential equations. *SIAM J. Math. Anal.*, 43(4):1955–1974, 2011.

[37] A. Gentaume. Laboratory characterization of firebrands involved in spot fires. *Annals of Forest Science*, 68:531–541, 2011.

[38] A. Gentaume, C. Lampin-Maillet, M. Guijarro, C. Hernando, M. Jappiot, T. Fonturbel, P. Perez-Gorostiaga, and J. Vega. Spot fires: fuel ammability and capability of firebrands to ignite fuel beds. *Int. J. Wildland Fire*, 18:951–969, 2009.

[39] B. Greese. Development, analysis and application of a nonlinear integro-differential equation in the context of cancer growth. Master's thesis, University of Alberta, 2005.

[40] Forestry Canada Danger Group. Development and structure of the canadian forest fire behaviour prediction system. Technical report, Forestry Canada, 1992.

[41] Y. Jin and M. A. Lewis. Seasonal influences on population spread and persistence in streams: spreading speeds. *J. Math. Biol.*, 65(3):403–439, 2011.

[42] A.M. Kanuri. *Introduction to Combustion Phenomena.* Gordon and Breach Science, New York, 1995.

[43] D.G. Kendall. Mathematical models of the spread of infection. In *Mathematics and Computer Science in Biology and Medicine*, pages 213–225. H.M.S.O., London, 1965.

[44] W.D. Kermack and A.G. McKendrick. Mathematical models of the spread of infection. *Proc. Royal Soc. A.*, 115:700–721, 1927.

[45] A.N. Kolmogorov, I.G. Petrovsky, and N.S. Piskunov. Etude de l'equation de la diffusion avec croissance de la quantite de matiere etson application a un probleme biologique. *Bull. Univ. Moskov. Ser. Internat. A*, 1:1–25, 1937.

[46] E. Koo, P.J. Pagni, D.R. Weise, and J.P. Woycheese. Firebrands and spotting ignition in large-scale fires. *Int. J Wildland Fire*, 19:818–843, 2010.

[47] M. Kot, M. Lewis, and P. van den Driessche. Dispersal data and the spread of invading organisms. *Ecology*, 77:2027–2042, 1996.

[48] P.D. Lax. *Functional Analysis*. John Wiley and Sons, 2002.

[49] J.M. Lee. *Introduction to Smooth Manifolds*. Springer-Verlag, New York, 2006.

[50] R. Linn, J. Winterkamp, C. Edminster, J.J. Colman, and W.S. Smith. Coupled influences of topography and wind on wildland fire behaviour. *Int. J Wildland Fire*, 16:183–195, 2007.

[51] F. Lutscher. A short note on short dispersal events. *Bull. Math. Biol.*, 69:1615–1630, 2007.

[52] A.H. Lynch and J.J. Cassano. *Applied Atmospheric Dynamics*. John Wiley and Sons, 2006.

[53] S.L. Manzello, T. G. Cleary, J.R. Shields, and J. C. Yang. On the ignition of fuel beds by firebrands. *Fire Mater.*, 30:77–87, 2006.

[54] S.L. Manzello, A. Maranghides, and W.E. Mell. Firebrand generation from burning vegetation. *Int. J. Wildland Fire*, 16:458–462, 2007.

[55] S.L. Manzello, A. Maranghides, J.R. Shields, W.E. Mell, and Y. Hayashi. Mass and size distribution of firebrands generated from burning Korean pine trees. *Fire Mater.*, 33:21–31, 2009.

[56] A.G. McArthur. Fire behaviour in eucalypt forests. Technical report, Commonw. Aust. For. Timber Bureau, 1967.

[57] B. McCaffrey. Momentum implications for buoyant dffusion flames. *Combustion and Flames*, 52:149–167, 1983.

[58] R. McIlveen. *Fundamentals of Weather and Climate.* Oxford University Press, 2nd edition, 2010.

[59] G.N. Mercer and R.O. Weber. Plumes above line fires in a cross wind. *Int. J Wildland Fire*, 4(4):201–207, 1994.

[60] D. Mollison. Possible velocities for a simple epidemic. *Adv. Appl. Prob.*, 4:233–257, 1972.

[61] D. Mollison. The rate of spatial propagation of simple epidemics. In W. Fitzgibbon and H. Walker, editors, *Proc. 6th Berkeley Symp. on Math. Statist. and Prob., Vol 3,*, pages 579–614. University of California Press, 1972.

[62] A. Muraszew and J.B. Fedele. Firebrand investigation. Technical report, The Aerospace Corporation, El Segundo, CA, 1975.

[63] A. Muraszew, J.B. Fedele, and W.C. Kuby. Trajectory of firebrands in and out of fire whirls. *Combust. Flame*, 30:321–324, 1977.

[64] F. Nmira, J.J. Consalvi, P. Boulet, and B. Porterie. Numerical study of wind effects on the characteristics of flames from non-propagating vegetation fires. *Fire Safety Journal*, 45:129–141, 2010.

[65] A. Pazy. *Semigroups of Linear Operators and Applications to Partial Differential Equations.* Springer-Verlag, New York, 1983.

[66] P. Porterie, J.C. Louraud, D. Morvan, and M. Larini. A numerical study of buoyant plumes in cross-flow conditions. *Int. J Wildland Fire*, 9(2):101–108, 1999.

[67] S.J. Pyne, P.L. Andrews, and R.D. Laven. *Introduction to Wildland Fire*. John Wiley and Sons, New York, 2nd edition, 1996.

[68] J.G. Quintiere. *Fundamentals of Fire Phenomena*. John Wiley and Sons Ltd., 2006.

[69] G.D. Richards. An elliptical growth model of forest fire fronts and its numerical solution. *Int. J. Numerical Methods in Engineering*, 30:1163–1179, 1990.

[70] T. Robbins. *Seed dispersal and biological invasion: A mathematical analysis*. PhD thesis, University of Utah, 2003.

[71] J.C. Robinson. *Infinite-Dimensional Dynamical Systems: An Introduction to Dissipative Parabolic PDE's and the Theory of Global Attractors*. Cambridge Texts in Applied Mathematics, 2001.

[72] H. Rouse, C.S. Yih, and H.W. Humphries. Gravitational convection from a boundary source. *Tellus*, 4:202–210, 1952.

[73] S.D. Ryu. The seven types of spotting. Private correspondence.

[74] A. Okubo S.A. Levin. *Diffusion and Ecological Problems: Modern Perspectives*. Springer-Verlag, New York, 2nd edition, 2002.

[75] C. Tarifa Sanchez, P. Perez del Notario, and F. Garcia Moreno. On the flight paths and lifetimes of burning particles of wood. *Proceedings of the Combustion Institute*, 10:1021–1037, 1967.

[76] N. Sardoy, J-L. Consalvi, B. Porterie, and A.C. Fernandez-Pello. Modeling transport and combustion of firebrands from burning trees. *Combustion and Flame*, 150:151–169, 2007.

[77] K. Schumacher. Travelling front solutions for integro-differential equations. i. *J. Reine Angew. Math.*, 316:54–70, 1980.

[78] K. Schumacher. Travelling-front solutions for integro-differential equations. ii. In *Biological growth and spread (Proc. Conf. Heidelberg, 1979)*, pages 296–309. Lecture Notes in Biomath. 38, Springer, Berlin, 1980.

[79] O. Sero-Guillaume, S. Ramezani, J. Margerit, and D. Calogine. On large scale forest fires propagation models. *Int. J. Thermal Sciences*, 47:680–694, 2008.

[80] J.A. Sethian. *Level Set Methods and Fast Marching Methods*. Cambridge University Press, New York, 2nd edition, 1999.

[81] E. Suli and D. Mayers. *An Introduction to Numerical Analysis*. Cambridge University Press, 1st edition, 2003.

[82] A.L. Sullivan. A review of wildland fire spread modelling, 1990-present, parts i-iii. retrieved from arXiv:0706.3074v1 [physics.geo-ph], 2007.

[83] R. Sun, M.A. Jenkins, S.K. Krueger, W. Mell, and J.J. Charney. An evaluation of fireplume properties simulated with the fire dynamics simulator (fds) and the clark coupled wildfire model. *Can. J. For. Res.*, 36:2894–2908, 2006.

[84] R. Sun, S.K. Krueger, M.A. Jenkins, M.A. Zulauf, and J.J. Charney. The importance of fire-atmosphere coupling and boundary-layer turbulence to wildfire spread. *Int. J Wildland Fire*, 18:50–60, 2009.

[85] M.E. Taylor. *Partial Differential Equations I: Basic Theory*. Springer-Verlag, New York, 1996.

[86] H.R. Thieme. Asymptotic estimates of the solutions of nonlinear integral equations and asymptotic speeds for the spread of populations. *J. Reine Agnew. Math.*, 306:94–121, 1979.

[87] H.R. Thieme and X.Q. Zhao. Asymptotic speeds of spread and traveling waves for integral equations and delayed reaction-diffusion models. *J. Diff. Eqn.*, 195(2):430–470, 2003.

[88] S.D. Tse and A.C. Fernandez-Pello. On the flight paths of metal particles and embers generated by power lines in high winds - a potential source of wildland fires. *Fire Safety Journal*, 30:333–356, 1998.

[89] C. Tymstra. Prometheus - the Canadian wildland fire growth model: Development and assessment. Technical report, Canadian Forest Service, Northern Forestry Centre, 2007.

[90] H.H. Wang. Analysis on downwind distribution of firebrands sourced from a wildland fire. *Fire Technology*, 47:321–340, 2011.

[91] R. Weber. Towards a comprehensive wildfire spread model. *Int. J. Wildland Fire*, 1(4):245–248, 1991.

[92] H.F. Weinberger. Long-time behaviour of a class of biological models. *SIAM J. Math. Anal.*, 13, no.3:353–396, 1982.

[93] J.P. Woycheese, P.J. Pagni, and D. Liepmann. Brand propagation from large-scale fires. *J. Fire Protect. Eng.*, 10:32–44, 1999.

[94] H. Yagista. Existence and nonexistence of traveling waves for a nonlocal monostable equation. *Publ. RIMS, Kyoto Univ.*, 45:925–953, 2009.

[95] W. Zdunkowski and A. Bott. *Dynamics of the Atmosphere: A Course in Theoretical Meteorology.* Cambridge University Press, 2003.